2011

Design and Analysis of an Innovative Semi-Flexible Hybrid Personal-Body-Armor System

Daniel Jeffrey Miller
University of South Florida, daniel.miller@hatch.ca

Design and Analysis of an Innovative Semi-Flexible Hybrid Personal-Body-Armor System

by

Daniel Jeffrey Miller

A thesis submitted in partial fulfillment
of the requirements for the degree of
Master of Science in Mechanical Engineering
Department of Mechanical Engineering
College of Engineering
University of South Florida

Major Professor: Autar Kaw, Ph.D.
Glen Besterfield, Ph.D.
Craig Lusk, Ph.D.

Date of Approval:
March 22, 2011

Keywords: Woven Composites, Textiles, Impact, ANSYS, AUTODYN, Mechanical Energy Transfer

DEDICATION

This thesis dedicated to my wonderful and beautiful wife, Summer. Without her love, support, and encouragement this project wouldn't even have started.

ACKNOWLEDGEMENTS

I would like to acknowledge the generous support of my wife, parents, family, friends, co-workers and professors. All of them in no small part contributed to every step in this project from start to finish, both directly and indirectly.

I would like to recognize and thank my advisor Dr. Autar Kaw who motivated, guided and mentored me through all phases of this work. Without any hesitation, he accepted the project, and devoted time and resources to insure that I was granted what I needed. He is truly a wonderful professor, engineer, and mentor.

Without the love, support and words of encouragement from my wife, Summer, this project would have never been started. She has stood by me during every step of the process, helping me think outside the box, pushing me along, and making me laugh and smile. I am truly indebted to her.

My parents, Bonny and Jeff, have been nothing short of wonderful in the support and words of wisdom that they have given me throughout the project. They raised me to pursue my passions, work hard, be friendly, and enjoy life. These virtues were always in on my mind during the good and bad times.

I would also like to thank my friend and co-worker, Sri Harsha Garapati for his help and support in this project. The time and effort of Dr. Glen Besterfield and Dr. Craig Lusk as committee members is greatly appreciated.

TABLE OF CONTENTS

LIST OF TABLES

LIST OF FIGURES

LIST OF EQUATIONS

ABSTRACT

Current military-grade rifle body armor technology uses hard ballistic plates positioned on top of flexible materials, such as woven Kevlar® to stop projectiles and absorb the energy of the impact. However, absorbing the impact energy and stopping a rifle projectile comes at a cost to the wearer – mobility. In this thesis, a new concept for personal body armor is proposed – a semi-flexible hybrid body armor. This hybrid armor is comprised of two components that work as a system to effectively balance the flexibility offered by a soft fabric based armor with the protection level of hard plated armor. This work demonstrates techniques used to analyze and design the hybrid armor to be compliant with National Institute of Justice guidelines. In doing so, finite element analysis is used to simulate the effect of a projectile impacting the armor at various locations, angles, and velocities, while design of experiments is used to study the effect of these various impact combinations on the ability of the armor component(s) (including the wearer) to absorb energy.

The flexibility and protection offered by the two component armor system is achieved by the use of proven technique and innovative geometry. For the analytical design, the material properties, contact area(s), dwell duration, and energy absorption are all carefully considered. This yields a lightweight but yet effective armor, which is estimated to weigh 36% less than the current military grade hard body armor.

Using ANSYS, several simulations were conducted using finite element analysis, including a direct center impact, along with various other impacts to investigate possible weak points in the armor. In doing so, it is determined that only one of these impact locations is indeed a potential weak point. The finite element analysis continues to show that a rifle projectile impacting at an oblique angle reduces the energy transferred to the wearer by about 25% (compared to a direct impact).

A design of experiments approach was used to determine the influence of various input parameters, such as projectile impact velocity and impact location. It is shown that the projectile impact velocity contributes 36% to the ability of the wearer to absorb energy, whereas impact velocity contributes only 13% to the energy absorbed by the top armor component. Furthermore, the analysis shows that the impact location is a highly influential factor (with a 69% contribution) in the energy absorption by the top armor component.

CHAPTER 1 PERSONAL BODY ARMOR TECHNOLOGY OVERVIEW

1.1 Purpose of Body Armor

The need to protect one's body in armed combat is as old as combat itself. In a side-by-side technology race, the evolution of weaponry brings the development of armor systems to protect oneself from the intended purpose of these weapons. The objective of body armor is to provide an individual with a resistance from a specified threat while maximizing the wearer's dexterity and minimizing the armor bulk. All body armor systems share at least one inherent trait, a balance of user mobility and ballistic protection (David, Gao and Zheng 2009). Traditionally, as the armor system increases in weight and bulk, the wearer loses stamina and the ability to move rapidly to counter the movements of their advisary. This trend is evident in modern warfare where on the battlefields of Iraq and Afghanistan, United States and Coalition fighters regularly wear hard armor weighing at least 25 lbs. In contrast, their opposition does not typically wear body armor and may only be carrying extra ammunition (Lopez 2009). Although well-protected, the United States and Coalition fighters are not able to move rapidly to pursue or counter the enemy fighters (Lardner 2009).

Beyond simply stopping a specified threat, a properly designed body armor system must also account for the body location that the armor will be worn for protection. Statistical research completed by independent organizations shows that particular body locations are more likely than others to be impacted by penetrating missiles in ground

combat (Grau and Jorgensen 1998). By investigating previous engagements, this research shows that the torso received 47.6% of all fatal missile impacts, followed by the limbs which received 22.8% of all fatal missile impacts (Brady 2003). Although the need to protect these vulnerable areas is high, the torso and limbs have both proven to be very difficult to protect in past conflicts. This is mainly because of the previously mentioned balance of mobility and ballistic protection (Lopez 2009). To protect the torso and limbs, body armor designers and inventers must balance and focus on flexibility, low weight, and ballistic protection against shrapnel and moderate caliber rifle missiles. This fine balance of ballistic protection and mobility has continually challenged body armor designers to devise clever technology to defeat battlefield threats while maintaining low weight and high mission effectiveness by the wearer (Lardner 2009).

1.2 Body Armor Technologies

The development of practical body armor to protect against penetrating missiles has reached several key stages since the mid-1800s. Materials such as silk, cotton, metallic, plastic, synthetic fiber and ceramic have all been used to some extent in ballistic body armor to successfully protect against a specified missile threat ((Discovery Media 2011), (Ministry of Foreign Affairs n.d.), (Nicky 2004), (Bashford 1920), (Olive-Drab LLC 2008)).

In the mid to late-1800s and early 1900s, the first wearable flexible soft ballistic vests to protect against “slow” moving black powder and/or small caliber lead missiles were designed. Two designs are recorded; the first design was invented in Korea that uses multiple layers (upwards of thirty layers) of woven cotton, and the second design, from Poland uses several layers of woven silk to protect against the pistol missiles of the time

((Discovery Media 2011), (Ministry of Foreign Affairs n.d.)). Although both of these designs are considered by historians to offer the wearer flexibility, they are theoretically only capably of stopping soft and slow black powder missiles, offering limited protection against high speed rifle projectiles.

Approximately during the same time period in Australia, bushranger gang members led by Ned Kelly used an arrangement of iron plates forged from plow (plough) blades to protect against multiple types of law enforcement firearm projectiles. This armor system, known as "Kelly Armour" is estimated to weigh nearly 96 lbs, and although effective at stopping projectiles, the system was impractical due to the great lack of mobility of the wearer (Nicky 2004).

The United States of America and other European counties did not actively pursue body armor technology (for firearm projectiles) until 1917, in response to casualties caused by automatic (machine) guns being actively utilized on the European battlefields of World War I. The United States of America developed the "Brewster Body Shield" which weights approximately 40 lbs, was modeled from high strength steel and covered much of the upper body (Bashford 1920). Although the wearer was fairly well protected against rifle and machine gun threats, only limited quantities of this armor were fielded due to the heavy weight and the inability of the user to aim a rifle while wearing the system (Bashford 1920).

During the Second World War, both the United States of America and the Soviet Union designed and fielded several body armor systems. The United States system was designated the M-12 vest (also known as the "flak" vest) and was worn mainly by aircrew members of bomber aircraft to protect the vital organs against explosive

fragments (Olive-Drab LLC 2008). The Soviet design (SN-42) was worn by ground infantry units in urban combat to protect against the German 9 mm Luger (presently renamed the 9×19 mm NATO) projectile at a range of 100 meters and beyond (wikipedia 2010). The flak vest was made from multiple layers of woven ballistic nylon fibers and contained aluminum plates and weighed 12 lbs, while the SN-42 system employed two layers pressed steel sheets and weighed about 7.7 lbs.

The Soviet SN-42 armor is not known to be further developed following World War II, however American scientists and engineers continued to develop the flak vest for the Korean and Vietnam conflicts. The new vests, designated the M-1951 (Korean) (Encyclopaedia Britannica 2010) (Olive-Drab LLC 2008), and M69 (Vietnam) (Encyclopaedia Britannica 2010), (vietnamgear.com n.d.), implemented reinforcements by first using laminated fiber glass (M-1951) (Encyclopaedia Britannica 2010) and then boron-carbide ceramic plates (M69) (Hannon and Abbott 1968) with additional layers of the originally designed woven ballistic nylon. Because of the use of laminates, then with the use ceramics the weight of the vest decreased from 12 lbs (as worn in World War Two) to approximately 8.5 lbs (as worn in Vietnam) (Encyclopaedia Britannica 2010). Both the M-1951 and M69 improved flak vests did not offer much, if any ballistic protection against the common rifle projectiles of the generation. But both did protect the wearer from explosive fragmentation and small caliber pistol projectiles, at a cost of mobility and heat generation to the wearer. Statistics show that the percentage of fatal penetrating explosive fragments to the chest and stomach (including the pelvis) decreased with the use of flak jackets over time by 5.3% and 3.2%, respectively (Grau and Jorgensen 1998).

Toward the end of the Vietnam conflict, and with the intent of designing lightweight automobile tires, the chemical company DuPont™ developed the aramid (name brand Kevlar®) fiber (DuPont 2010) . This high molecular weight fiber was found to possess high strength, high ballistic resilience and a relatively low weight – a natural fit for body armor. Kevlar® can be woven in a similar fashion to many other textiles to form sheets, which in turn are layered to form a ballistic armor system, such as a vest. One of the first Kevlar®-based armor vests was designed in 1972 by Second Chance Body Armor (Second Chance Body Armor 2010), which was a semi-flexible soft armor vest. This armor system offered protection against some pistol projectiles and explosive fragments, providing an alternative to the ageing flak vest, but was not fully accepted by the United States Armed Forces. Second chance Body Armor is still producing Kevlar® vests, mainly for law enforcement officials and is credited with saving nearly a thousand lives (Second Chance Body Armor 2010).

In response to the threats of the cold war, and fueled by the invention of Kevlar® (and possibly the success of the Second Chance Body Armor vest), the United States redesigned the body armor system to be worn by the U.S. Armed Forces. In the early 1980s, the U.S. Army fielded the next generation of body armor, named the Personnel Armor System for Ground Troops, or PASGT (Olive-Drab LLC 2008). The ballistic protection of this armor is offered by using sixteen layers of semi-flexible woven Kevlar®, weighs approximately 9 lbs, and offered protection against some pistol and fragmentation projectiles, to a higher degree then the flak vest. The entire PASGT system (Kevlar® vest and helmet) was worn by the U.S. armed forces in Operation Desert Storm in 1990-1991, where statistics show that the percentage of penetrating missiles to the

chest was merely 5.8%, a much lower statistic then anyone would have predicted (Grau and Jorgensen 1998). These same statistics also show that the percentage of penetrating missiles to the unprotected abdomen was 9.3%, which is similar to previous conflicts, thus validating the use of Kevlar® based body armor. The PASGT was worn unchanged by troops until 1996, at which point the Interim Small Arms Protective Overvest (ISAPO) was added to offer the wearer protection against high speed pistol and rifle projectiles (Olive-Drab LLC 2008). The ISAPO system was worn over the PASGT vest and held two ballistic ceramic plates, one plate mainly located over the wearer's heart and lungs, while the other located over the wearer's back. Together, the ISAPO and PASGT system weighted approximately 25 lbs and was criticized as being bulky, heavy and restricting (Olive-Drab LLC 2008).

During the war on terrorism in 2003, the United States military redesigned the personal body armor system, this time from the ground up (Hodge 2006). The new armor system, named the Interceptor Body Armor (IBA) utilizes a Kevlar® vest similar to the PASGT vest, only adjusted to be more ergonomic, and contains several integrated ballistic plate holding pockets (front and rear), thus eliminating the overvest (ISAPO) worn previously. The Interceptor Body Armor is a modular system comprised of a basic Kevlar® vest and additional ballistic plates that can be worn to protect the torso, crest, stomach, arms, neck and groan from rifle projectiles. The basic vest weighs approximately 8.3 lbs and the entire system (wearing all ballistic plates) weighs about 34 lbs (Lopez 2009) (Lardner 2009), but offers better rifle protective coverage area and a higher multiple hit capacity compared to the PASGT. Although considered to be bulky, heavy, and unnatural by many who have worn the system, the U.S. Military is currently

using the IBA for all combat and frontline troops (Lopez 2009) (Lardner 2009), (Olive-Drab LLC 2008).

Figure 1 depicts a scaled (by year) timeline of the date of use or invention of the various body armor systems discussed. Notice that major conflicts are bracketed by year to provide a reference for the reader. By no means does the timeline presented in Figure 1 represent all the body armor technologies developed during the shown years, it merely highlights the commonly used technologies by the U.S. military, law enforcement departments and foreign militaries.

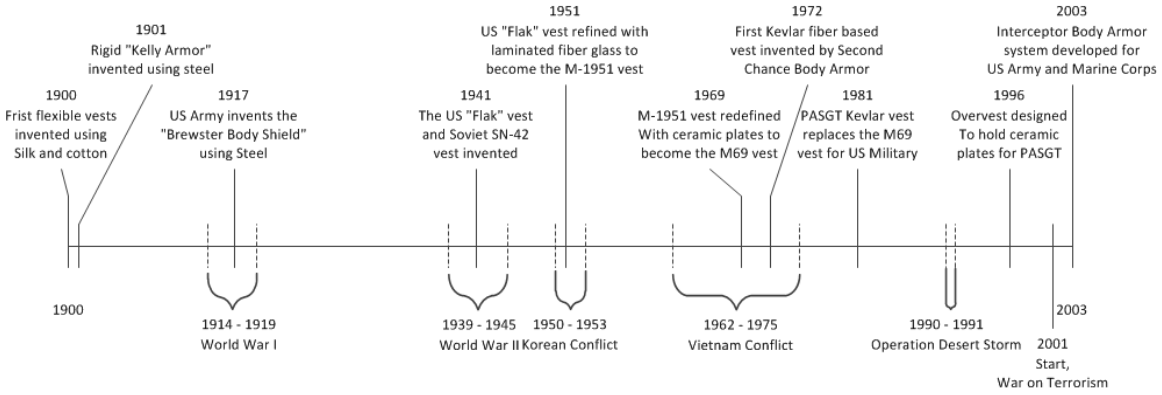

Figure 1 Timeline showing several body armor technologies.

As shown in the timeline most body armor advances and changes take place during major conflicts. This trait follows the cliché "necessity is the mother of invention".

CHAPTER 2 THREAT LEVELS AND TESTING STANDARDS

2.1 Threat Levels

To properly design a body armor system, a designer must first consider the following things:

1) the threat level to protect the wearer against, and
2) the environment that the armor will be worn.

To quantify the threat level to protect against, the kinetic energy (Greenwood 1988), E_k (J), of a projectile can be calculated by relating both the translational velocity (m/s) and mass (kg) as in Equation 1.

$$E_k = \frac{1}{2} m V^2$$

Equation 1 Kinetic energy of a projectile given mass and velocity.

where V is the projectile velocity, and m projectile mass.

Equation 1 is only valid if the projectile remains a single mass and only translational velocity is considered. Table 1 shows several common modern projectiles with the corresponding projectile muzzle velocity, mass and calculated kinetic energy (U.S. Department of Justice 2008) (Fickler, Ballistic Injury 1986) (Fickler, Wounding Patterns of Military Rifle Bullets 1989).

Table 1 Common modern projectiles with muzzle ballistics data.

Projectile	Type	Velocity (m/s)	Mass (gm)	Energy (J)
0.22 LR (long rifle)	Pistol/Rifle	342	2.70	160.0
9×19 mm NATO	Pistol	373	8.00	556.5
0.357 Magnum	Pistol	408	10.2	849.0
0.44 Magnum	Pistol	436	15.6	1482
5.56×45 mm NATO	Rifle	943	3.60	1601
5.65×45 mm (AP) NATO	Armor Piercing	925	4.00	1711
7.62×39 mm Soviet	Rifle	713	7.89	2006
7.62×51 mm NATO	Rifle	862	9.70	3604
0.30 caliber M2 AP	Armor Piercing	887	10.8	4249

A body armor system for a police officer to be worn while on patrol is normally designed to defeat threats from a 0.357 magnum and below (Second Chance Body Armor 2010) (Pinnacle Armor 2010) whereas a frontline infantry soldier would wear armor to protect against the 7.62×39 mm Soviet projectile (Olive-Drab LLC 2008).

2.2 Design and Testing Standards

Once the designer determines the type of threat that the body armor will be designed to defeat, the type of armor can be systematically classified. In the United States, the National Institute of Justice (NIJ) has created a commonly used system of ratings varying in levels from I to IV (with some intermediate level designated with an "a") to categorize body armor vests (U.S. Department of Justice 2008). These body armor types are shown in Table 2.

Table 2 NIJ body armor levels shown with defeated threat.

Level	Protection Against	Remarks
I	0.22 LR and similar missiles	Obsolete armor level
IIA	9x19mm NATO and similar missiles	Concealable soft armor
II	0.357 Magnum and similar missiles	Worn by many police officers
IIIA	0.44 Magnum and similar missiles	Bulky semi-hard armor
III	Military Rifles	This armor uses ceramic plates
IV	Armor Piercing Rifle	Very bulky and hard armor

Typically, the armor vests categorized as NIJ level I, IIA, and II are referred to as "soft" body armor, whereas, levels IIIA, III and IV are commonly referred to as "hard" body armor (U.S. Department of Justice 2008). This is because soft body armor characteristically uses layers of woven textile materials, such as ballistic nylon or Kevlar® 29 fibers, to protect against projectiles and thus when worn remains flexible or semi-flexible (David, Gao and Zheng 2009). Alternatively, hard body armor normally uses a combination of woven fibers with ceramic and/or metallic ballistic plates, such as boron-carbide to protect against many pistol and more critically, rifle projectiles (David, Gao and Zheng 2009). An example of a currently used hard body armor system is the interceptor body armor (IBA) worn by soldiers and marines of the U.S. military.

The balance of protection and mobility is demonstrated and considered in both soft and hard body armor. The mobility inherent of soft body armor comes at the cost of ballistic protection, whereas to achieve a higher degree of protection, the wearer of hard body armor must sacrifice mobility.

In addition to classifying body armor, the National Institute of Justice has also established and outlined a detailed and methodical armor testing rubric (U.S. Department of Justice 2008). Factors contributing to the scoring of a body armor system during the

testing are (but not limited too), the bullet line of flight, angle of incidence, backface signature (BFS), backing material fixture, bullet type, bullet velocity, shot-to-edge distance, and environmental conditions (moisture, humidity, temperature, etc). Figure 2 depicts a typical body armor system testing setup.

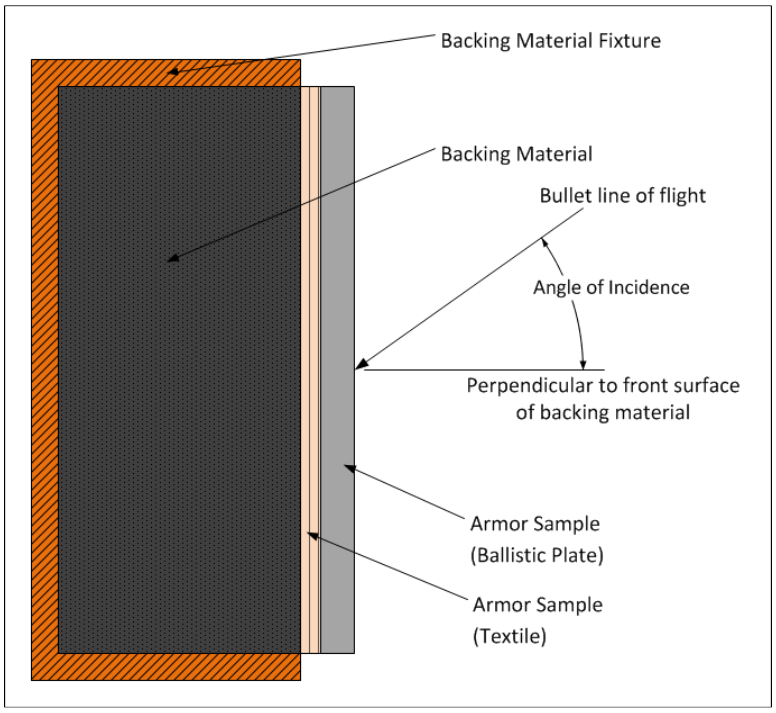

Figure 2 Side view of testing setup as per NIJ standards (not drawn to scale).

Figure 2 shows a hard body armor sample, identified by the use of both the ballistic plate and textile placed on the specified backing material as per NIJ standards. Following the NIJ guidelines, the backing material is specified to be a homogenous block of nonhardening oil-based modeling clay which must be placed in contact with the back face of the armor panel during all testing (U.S. Department of Justice 2008). The backing material fixture is specified to be a box-like rigid frame made from plywood (or metal) with a removable back which restrains the backing (clay) material (U.S. Department of Justice 2008).

The complete scoring of a body armor system in accordance with NIJ standards is complex and requires many different controlled laboratory tests. However, two main factors are indicant that a body armor system has failed with certainty, and these are:

1) an excessive BFS and/or

2) a perforation of the body armor system.

This is one of the first tests conducted by NIJ officials on a potential body armor system and the test is named the Perforation-Backface Signature (P-BFS) test (U.S. Department of Justice 2008). As per NIJ standards (U.S. Department of Justice 2008) "A perforation is any impact which creates a hole passing through the armor," and the backface signature (BFS) is defined as the greatest extent of indentation in the backing material caused by a nonperforating impact on the armor . An armor system is considered to have stopped a projectile if the outcome of the P-BFS test is that the projectile is either captured or deflected by the armor, with no portion of the projectile or fragments of the armor perforating the armor, and resulting in a BFS less than 44 mm (U.S. Department of Justice 2008).

To complete the P-BFS test, NIJ officials conduct several tests on identical armor samples using common projectiles (listed in Table 1). Each armor sample is impacted at a specified velocity at zero, and then 30° and/or 45° angle of incidence. This procedure is repeated for all armor levels (starting at type IIA) with a new armor sample until the armor sample has failed the P-BFS test.

Table 3 shows the NIJ testing requirements for the P-BFS test (U.S. Department of Justice 2008).

Table 3 NIJ testing hit requirements for the P-BFS test.

Armor Type	Bullet type	Test velocity (m/s)	Bullet mass (gm)	Kinetic energy (J)	Hits at 0° angle	Hits at 30° or 45° angle	Maximum BFS (mm)
I	0.22 LR	342	2.70	160.0	4	2	44
IIA	9×19 mm	373	8.00	556.5	4	2	44
II	0.357 Magnum	408	10.2	849.0	4	2	44
IIIA	0.44 Magnum	436	15.6	1482	4	2	44
III	7.62 NATO	862	9.70	3604	6	0	44
IV	0.30 Caliber	887	10.8	4249	1-6	0	44

As one can see from examining the hit requirement table, an armor sample must be able to protect against a specific threat hit at any random location or angle of incidence. Additionally, one can gather that a multiple-hit capacity is a very important consideration for an armor design.

CHAPTER 3 FLESH WOUNDING AND BODY ARMOR PENETRATION

3.1 Bullet Impact Survivability - Protected and Unprotected

The survivability of an unprotected human struck by a bullet or high speed explosive fragment depends on four main wound mechanisms (Fickler, Ballistic Injury 1986) (Fickler, Wounding Patterns of Military Rifle Bullets 1989). These mechanisms are:

1) projectile penetration – defined as the action of the bullet tearing through and/or destroying tissue,
2) permanent flesh deformation – the permanent cavity created by the passage of the bullet where flesh once was,
3) temporary flesh deformation – which is characterized by the tissue that is stretched and/or torn by the shock wave propagation of the impact and the travelling projectile, and
4) fragmentation – which is associated with the pieces of the bullet and/or shattered bone that travel outward of the impact cavity that disrupt tissue, muscle and/or vessels.

The first two mechanisms, projectile penetration and permanent flesh deformation, are the most influential factors contributing the survivability of a bullet or fragmentation strike (Urey 1989). The temporary flesh deformation is primarily associated with bruising and blunt trauma (Fickler, Ballistic Injury 1986), and no

evidence suggests that this mechanism or fragmentation causes severe damage to elastic flesh (Urey 1989). A properly designed body armor system will insure safety to the wearer by defeating at least the first two wound mechanisms for all projectile threats, and thus will prohibit projectile flesh penetration, reduce energy transfer to the user, and minimize the inward flesh deflection.

3.2 Mechanisms of an Impact Into a Hard Body Armor System

The mechanisms and dynamics of a projectile impact into a body armor system are complex and not fully researched or understood (David, Gao and Zheng 2009), (Tabiei and Nilakantan 2008). Intrinsic material properties, damping characteristics, geometry, component constants, and layer inactions are only several of the variables that effect the ability of an armor system to distribute dynamic stresses, absorb energy, and stop a projectile once impacted. Over the past few decades, hard body armor has been studied to determine the basic mechanisms and sequence of events that occur during the moments of impact (David, Gao and Zheng 2009). Figure 3 shows a typical hard body armor system comprised of flexible woven layers of Kevlar® topped with a hard ballistic plate (facing toward the point of impact).

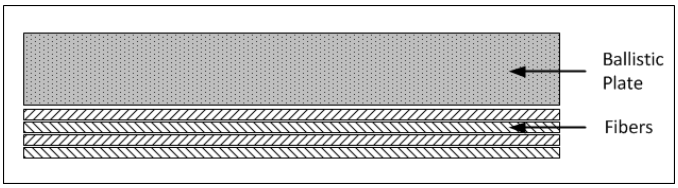

Figure 3 An example layout of a common hard armor system (side view shown).

The purpose of the ballistic plate is to degrade the projectile tip and spread the dynamic loads over a larger area to the underlying layers. Chocron-Galvez (Chocron and Galvez 1998) showed that during the first few moments (around 4 μs) of the projectile-

plate impact, the velocity of the plate is zero; because of the high compressive strength of the plate. During these moments, the tip begins to degrade and plastically deform by being compressed against ballistic plate, all-the-while a compressive shock wave travels at the speed of sound radially outward from the impact zone (Shokrich and Javadpour 2008). Chocron-Galvez (1998) continued to show that the rear of the projectile does not stop moving, and in addition, once the propagating shock wave reaches the outer edges of the ballistic plate, it reflects (mainly because of the larger mechanical impedance) and becomes a tensile shock wave which can fracture the ballistic plate ((Shokrich and Javadpour 2008),(David, Gao and Zheng 2009)). The fractured zone of the ballistic plate is known as the damage cone (or conoid) and is shown in Figure 4 (David, Gao and Zheng 2009), (Fellows and Barton 1999). The moments of impact when plate is not moving or deflecting in any way, and the projectile tip is being eroded is known as the dwell duration and is a very important design parameter for a ballistic plate (David, Gao and Zheng 2009).

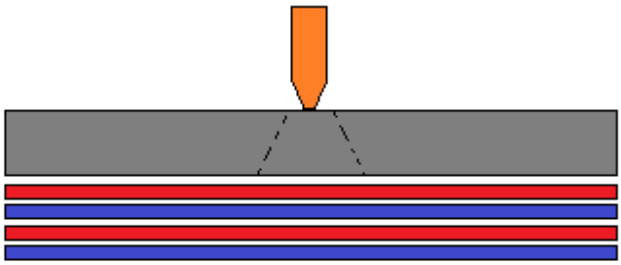

Figure 4 Impacted ballistic plate, shown at the moment of damage cone formation.

Upon the forming of the damage cone, the deformed projectile begins to perforate the ballistic plate. As perforation continues, the damage cone and plate fragments continue to reduce the projectile velocity and further degrade the projectile tip, while the

lower portion of the damage cone distributes the dynamic forces unto the underlying material(s) (David, Gao and Zheng 2009), as shown in Figure 5 (Tabiei and Nilakantan 2008). The underlying material(s) theoretically absorb much of the remaining kinetic energy and further distribute the dynamic forces on an enlarged area to the wearer, unless of course the armor is completely perforated.

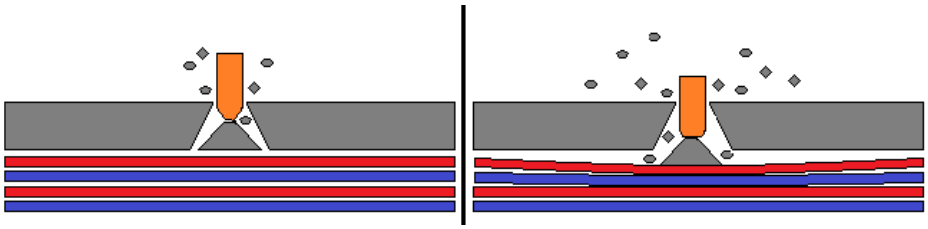

Figure 5 Shown is the damage cone post dwell duration. The figure to the right shows a later impact time of impact from the figure to the left.

In a case of the underlying material being comprised of a metal, energy is mainly absorbed via elastic and then plastic deformation or by fracturing, whereas when the underlying material(s) is/are a woven textile (or unidirectional composite), energy is mainly absorbed by frictional fiber interactions and fiber deformation (David, Gao and Zheng 2009), (Tabiei and Nilakantan 2008), (Gellert, Pattie and Woodard 1998). As in case of the ballistic plate, similar compressive shock waves propagate at the speed of sound radially outward and reflect off the underlying material edges, thus creating a tensile shock wave. However, the phenomenon of the dwell duration typically does not seem to exist for metals or textiles. Energy and stress is transferred transversely from one corresponding layer to the next and is governed by corresponding layer frictional and material constraints and geometric properties (Tabiei and Nilakantan 2008). These interactions continue to occur until projectile is either stopped and the system has reached equilibrium, or has completely perforated the armor system.

3.3 Bullet Design and the Effect on Penetration

Whether for good or bad, a bullet projectile is designed to penetrate and destroy a target. Four main parameters control the ability for a projectile to effectively penetrate a target (Fickler, Ballistic Injury 1986), and these are the

1) projectile mass,
2) projectile shape,
3) projectile construction, and
4) striking velocity.

When comparing a handgun to a rifle projectile, the handgun projectile is more massive with a nearly round nose, whereas a rifle projectile has a pointed nose and strikes at a much higher velocity (Figure 6).

Figure 6 Comparison of a 9×19 mm NATO (left) to a 5.56×45 mm NATO (right) cartridge.

Because of the higher striking velocity and pointed nose shape, a rifle projectile is generally better suited over a pistol projectile for target penetration (Fickler, Ballistic Injury 1986). The reverse is true for a pistol projectile where the nose is round, nominal bullet diameter is large, core is comprised of highly a ductile lead-alloy, and striking velocity is low. A pistol projectile is simply a poor choice for penetration (Brady 2003). Of the common rifle projectiles, the 5.56×45 mm (AP) NATO projectile is specifically designed with a dense steel-lead alloy "penetrator" core to penetrate armor (Fickler,

Wounding Patterns of Military Rifle Bullets 1989). This is considered to be the best armor piecing bullet among its category, hence the AP designation standing for Armor Piercing.

CHAPTER 4 IDEAL ARMOR AND ARMOR CONCEPT

4.1 Current Armor Problems and Shortfalls

Although hard body armor offers a high level of protection against common assault rifle projectiles and high velocity fragments, user mobility and dexterity is noticeably and significantly decreased (as compared to soft or no armor) (Lardner 2009). In addition to the decrease in mobility, the wearer's vital organs, such as the liver and stomach are not fully protected. Particular areas of venerability include the lower torso and upper chest, via the underarms. These areas are intentionally left unprotected to rifle fire to allow for a greater range of motion around and about the waist, as placing a hard ballistic plate would restrict motion. This is an example of balance of mobility and protection mentioned in Section 1.1 Purpose of Body Armor. Table 4 provides a summary of the current body armor problems.

Table 4 Problems with current hard and soft body armor systems.

Hard Body Armor (NIJ level IIIA/III) Problems	
1	Armor is heavy and bulky.
2	User mobility and dexterity is decreased as compared to wearing no armor.
3	NIJ level III protective coverage area is small, lower torso and under arms are exposed.
Soft Body Armor (NIJ level II/IIA) Problems	
1	No protection against a rifle and/or high powered pistol projectiles.

A mix of the great protective qualities of hard body armor with the high levels of protective area and mobility of soft armor would solve many of the problems listed in Table 4.

4.2 Ideal Armor

Given the current state of technology, a body armor system should be able to provide the wearer with protection against high speed rifle projectiles while minimally decreasing mobility. As shown in Table 2, a system capable of accomplishing this feat would be at least an NIJ level IIIA or III armor. The historically hard NIJ level IIIA/III armor systems would require a redesign of the ballistic plates to increase mobility and decrease armor weight, as this is the limiting factor to the wearer's mobility. Redesigning the classic ballistic plates to take advantage of modern technology will require that the plate geometry and material(s) be reconsidered, and this can be a challenging and time-consuming task.

This work aims to address the problems listed in Table 4, particularly by focusing on redesigning the common NIJ IIIA/III armor to take full advantage of current technology. To aid this effort, a set of objectives to directly address the current body armor problems (Table 4) was created, and is listed in

Table 5. An armor system that can fulfill these objectives using current technology is considered the ideal armor of today.

Table 5 Design objectives of the ideal armor system.

1	Increase the wearer's mobility and dexterity while maintaining at least NIJ level IIIA/III protection (as compared to traditional hard body armor).
2	Increase the NIJ level IIIA/III protection coverage area to include the lower torso and underarms.
3	Decrease the areal armor density (as compared other hard armor).

4.3 Preliminary Armor Design

To ease the daunting task of addressing the objectives listed in Table 5, the project was broken into four steps. A flowchart was used to create the ultimate design objectives, provide a map to solving the problem(s), and provide insight to the analysis procedure; this is shown in Figure 7. As one can see, the first step is to define the problem and list the design objectives. Other steps of the problem solving process include the background investigation, design and analysis strategy, and analysis tests outcomes to determine a design failure or success.

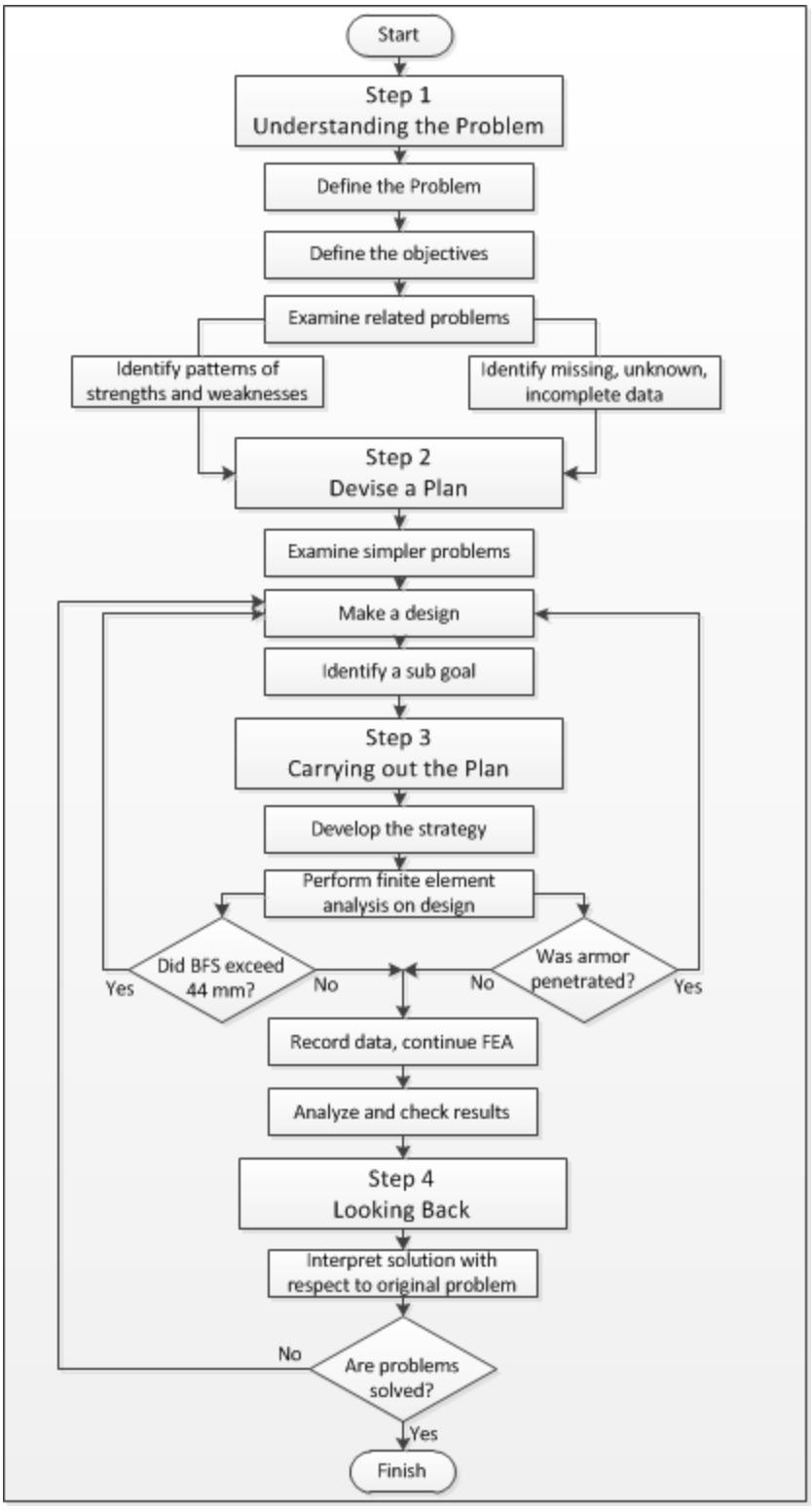

Figure 7 Flowchart used to step through the design and analysis process.

As shown in Figure 7, once the design objectives are set, Step 1 continues by investigating the strengths and weaknesses of current, obsolete, and ancient personal armor systems. These strengths and weaknesses traits are categorized (for example, flexibility, protection level, and weight) and compared and contrasted in Table 6 to identify any patterns and to determine what works or has worked previously relative to the design objectives. The examined armor systems include, the soft and hard armor body armor currently used (described in detail in Section 1.2 Body Armor Technologies), a proposed carbon nanotube armor (Li, et al. 2008), (David, Gao and Zheng 2009), the "coat of plates" armor worn in Russia in the 13th century (Yurasovskiy n.d.), and finally a stab-resistant personal armor researched and developed in Queen's University, Ontario, Canada (Croitoro and Boros 2007).

Table 6 Armor system trait comparison table.

Trait (0-10)	Soft Armor (Kevlar® vest)	Hard Armor (complete IBA)	Theoretical Nanotube armor	Russian "coat of plates"	Stab resistant armor
Protection	3	8	9	--	1
Coverage area	9	6	--	8	--
Weight	7	3	9	--	7
Flexibility	7	3	--	7	8
Manufacturability	8	4	0	--	8
Bulk	8	2	--	--	9

The protection trait listed in Table 6 refers to ability for the armor system to protect against a currently produced single assault rifle projectile. With the exception of soft and hard armor, the protection trait is an assumed number ((David, Gao and Zheng 2009), (Yurasovskiy n.d.), (Croitoro and Boros 2007)). The manufacturability and bulk traits listed correspond to the ability to mass produce the armor system and the overall armor thickness, respectively, and are assumed for all systems (based upon available

literature). The ideal personal armor system would receive a score of 10 for all categories. Note that some information is missing, not available, or unknown, such as the bulk of a nanotube based armor, the weight of the Russian "coat of plates" and the coverage area of the stab resistant armor.

4.4 Design Plan and Concept Proposal

Upon careful and complete examination of Table 6, the focus of the project is shifted to Step 2 of the problem solving process, that is to devise a plan. As shown, no armor system is capable of NIJ level III protection while preserving flexibility and low weight. However, a hybrid of existing and proven technologies may be able to favorably balance both protection and flexibility. The "coat of plates", and in particular the stab resistant armor array both utilize relatively small armor plates placed upon a flexible substrate, such as leather (shown in Figure 8), and both have previously been tested and proven to be wearable and less-restrictive for motion ((Croitoro and Boros 2007), (Yurasovskiy n.d.)). Similarly, soft Kevlar® armor vests have been worn for decades, providing NIJ level II protection, low bulk and weight, and medium to high flexibility (Second Chance Body Armor 2010). In contrast, the IBA has a fantastic ability to protect against rifle projectiles, however, is heavy, uncomfortable and bulky (Lopez 2009).

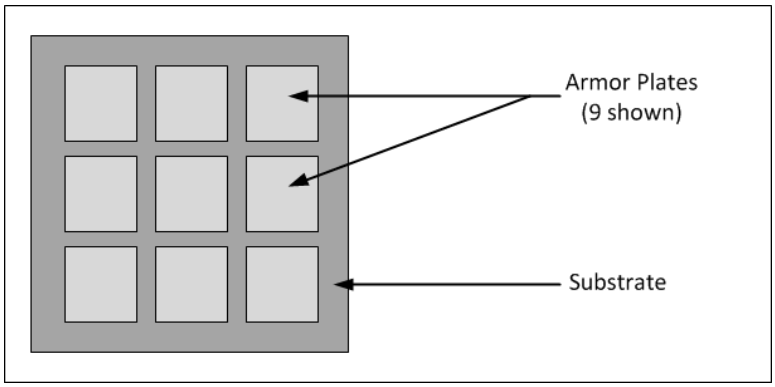

Figure 8 Example layout of flexible plated armor showing armor plates adhered to a flexible substrate (top view shown).

Focusing on the positive traits of the various armor systems, a new armor is proposed. The new armor, a hybrid semi-flexible armor answers the objectives listed in Table 5 by using a matrix of specially designed small ballistic plates placed on top of a substrate of flexible woven Kelvar® layers. Furthermore, each plate will be reinforced with at least one Kevlar® sheet. This sheet is to contain any ceramic fragments and to increase the multiple hit capacity. The small ballistic plates will be secured in place via elastic bands in an over-under cross fashion. The layout of the ballistic plates, shown in Figure 9 is geometrically similar to stab resistant armor mentioned in Table 6, proving that the system will be flexible (providing that the substrate is flexible). However, to avoid the inevitable gaps caused by using rectangular plates, the proposed armor plates will be skewed in two directions to provide a vital gap overlap (Figure 10).

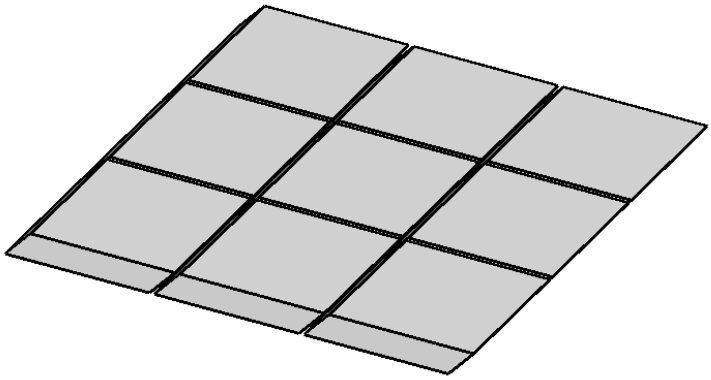

Figure 9 Rigid ballistic plate layout of hybrid semi-flexible armor.

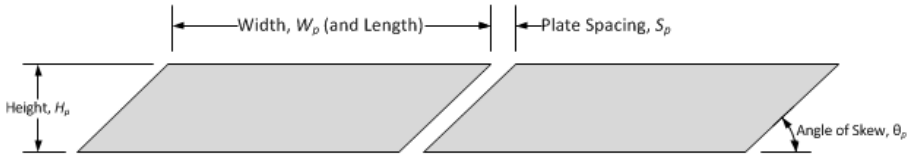

Figure 10 Cross-sectional sketch of two skewed biplates used for proposed armor.

The armor carrier as shown in Figure 11 and Figure 12 is made of cotton (or a similar textile) and contains two compartments.

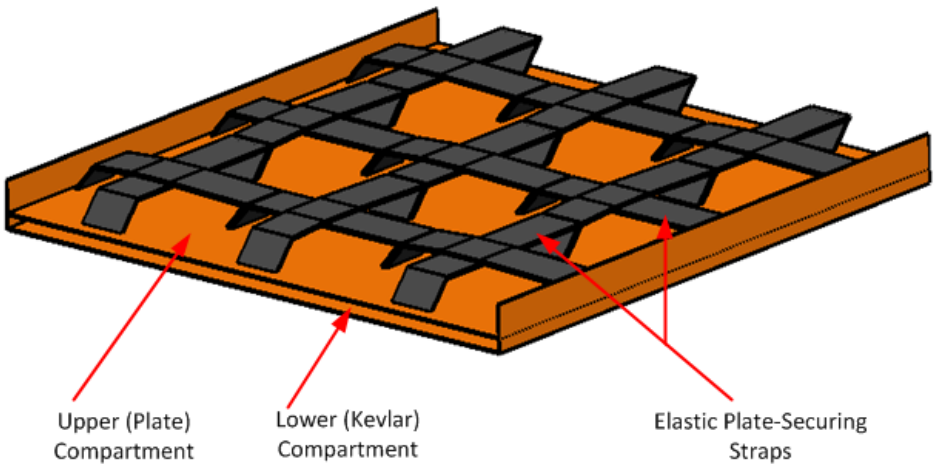

Figure 11 Orthogonal view of the hybrid armor carrier, shown without armor components.

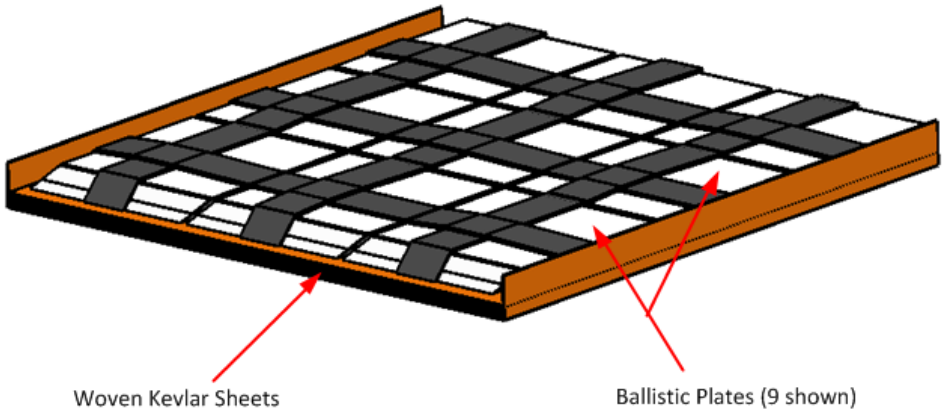

Figure 12 Orthogonal view of the hybrid armor carrier, shown with armor components.

The armor carrier will be worn on the person in a similar fashion to current armor vests, differing in that it will extend higher in the under arms and lower in the torso and groin area. This is made possible by the added flexibility, and therefore the rifle protective area will be increased (as compared to similar NIJ level III armor). Because of the elastic bands holding the ballistic plates in place, the plates can be added or removed to adjust the armor weight, tailor the protective level and comfort desired. The substrate layers may also be easily and freely removed from the lower compartment of the carrier to allow for potential upgrades and maintenance to the woven layers. Additionally, these underlying woven layers will be contained as a single unit inside of a plastic case. This case is to keep the fibers protected and isolated from any chemical, water, and/or ultra-violet light exposure.

The hybrid armor is intended to be worn by frontline combat personnel, specialized police forces and other law enforcement agencies requiring rifle projectile protection. Table 7 provides a summary of current body armor problems and the solution offered by the purposed semi-flexible hybrid body armor.

Table 7 Current armor problems listed with semi-flexible hybrid armor solution.

Problem	Proposed Solution
NIJ IIIA/III level armor is heavy	Optimization for current armor technologies equates to a lower overall areal density
Wearer lacks mobility/dexterity	Small double-skewed rigid ballistic plates will be placed overtop a flexible Kevlar® substrate
Limited rifle protection coverage	skewed ballistic plates provide mobility, additional plates are removable to allow for customization

CHAPTER 5 DESIGN PLAN

5.1 Design Subgoals

The actual design of the hybrid armor system is the next step in the flowchart shown in Figure 7, beginning with setting design subgoals for the finished system. Among the objectives listed in Table 5, the hybrid armor system will also have positive buoyancy and be less than 20 mm in overall thickness (0.787 inch, at the thickest point). Table 8 summarizes the preliminarily set goals and subgoals for hybrid armor system.

Table 8 Design goals and subgoals of the hybrid armor system.

Primary Goal	
1	Increase the wearer's mobility and dexterity while maintaining NIJ level III assault rifle protection (as compared to traditional hard body armor).
2	Increase the NIJ level III protection coverage area to include the lower torso and underarms.
3	Decrease the areal armor density (as compared other hard armor).
Subgoal	
1	Possesses positive buoyancy.
2	Maximum thickness to be no greater than 20 mm.

The areal density, A_p (kg/m^2) for an armor system consisting of n layers is determined by considering the mass density and thickness of each layer and is related in Equation 2 (David, Gao and Zheng 2009).

$$A_p = \sum_{i=1}^{n} t_i \rho_i$$

Equation 2 Areal density of an armor system.

where t_i the individual layer thickness (m) and ρ_i the individual mass density (kg/m^3).

Table 9 shows a few areal density values common armor technologies (David, Gao and Zheng 2009).

Table 9 Areal density of common armor systems.

Armor type	Areal density (kg/m^2)	Classification
Laminated Composite Armor	67	Rigid - hard
Woven Kevlar® 29	12	Flexible - soft
Ceramic-Metallic Plate armor	67	Rigid - hard
Sand and E-Glass Armor	16.5	Flexible - soft
Carbon Nanotubes	Unknown	Unknown

As shown in Table 9, a typical trend is that a textile based flexible armor has a significantly lower areal density as compared to a rigid plated armor system, such as the laminated composite armor.

5.2 Projectile Parameters

One of the factors beyond the control of the designer is the projectile that impacts the armor. In an ideal case, the armor system will be able to protect the wearer against all projectiles of many different shapes, masses, and impact velocities, regardless of the source (explosive fragment, pistol, rifle, etc). Since the impacting projectile type is unknown, good design practice dictates that the armor should be designed to protect against an impact from the best armor piercing projectile in the desired NIJ category.

As mentioned in Section 3.3 Bullet Design and the Effect on Penetration, a projectile with a high striking velocity and pointed tip is best suited for penetration. The

projectile mass and construction do not contribute as highly to penetration as the velocity and tip design do. To be classified as an NIJ level III armor, the system must protect the wearer against rifle projectiles such as the 5.56×45 mm NATO and 7.62 mm Soviet (7.62 Soviet), both common battlefield cartridges chambered for the M-16 and AK-47, respectively (Fickler, Wounding Patterns of Military Rifle Bullets 1989).

The geometry of hybrid armor system will be designed to protect against the high velocity of the 5.56×45 mm NATO (5.56 NATO) and the striking tip of both the 5.56 NATO and 7.62 Soviet. Additional design consideration will be given to the construction of the 5.56 NATO, as this projectile is specifically designed with a dense core to penetrate armor.

In an effort to keep the analysis as free of variables as possible, the hybrid armor system analysis will only consider the 5.56 NATO projectile, the best armor piercing projectile in the NIJ level III category. The impact velocity of this projectile will be adjusted to match the kinetic energy of the lesser NIJ level projectiles, such as the 9×19 mm NATO and 0.44 Magnum. This method will be covered in more depth in Chapter 7. Figure 13 shows the dimensions of the 5.56 NATO used for the design and analysis.

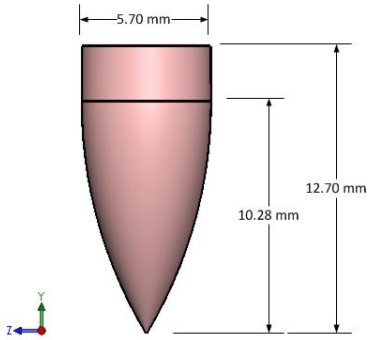

Figure 13 Projectile and dimensions used in design.

Note that in Figure 13, the diameter of the 5.56×45 mm NATO projectile is 5.70 mm and the length is 12.70 mm. This may seem counter-intuitive given the projectile name. The projectile contains a highly-dense lead alloy core surrounded by a copper alloy jacket, about 0.50 mm thick.

5.3 Armor Component Design

With the threat level and projectile type established, the design of the armor system itself may commence. The proposed hybrid armor system contains two main armor components, the

1) ballistic plate, and
2) underlying flexible Kevlar® (substrate).

The ballistic plate(s) serves to degrade the projectile structure, absorb much of the impact energy, and distribute the impact loads over a larger area to the substrate. The underlying flexible Kevlar® serves not only as the plate substrate, but also acts as a means of catching any fragments and to further distribute the impact loads.

To obtain both a low areal density and high compressive strength, ceramics are considered for the ballistic plate (Hannon and Abbott 1968). This decision brings on a new problem; in spite of a high compressive strength, ceramics typically have low modulus of resilience and thus cannot absorb much energy before failure (Norton 2006). To provide a means of absorbing energy, a two-layer ballistic plate is proposed, where the upper layer (orthogonal to and facing the point of impact) is a high hardness-low ductility material and the lower layer is a medium-strength-higher ductility material. This type of ballistic plate (shown in Figure 14) is commonly used in armor systems and is well researched (Teng, Wierzbicki and Huang 2008), (Davila and Chen 2000).

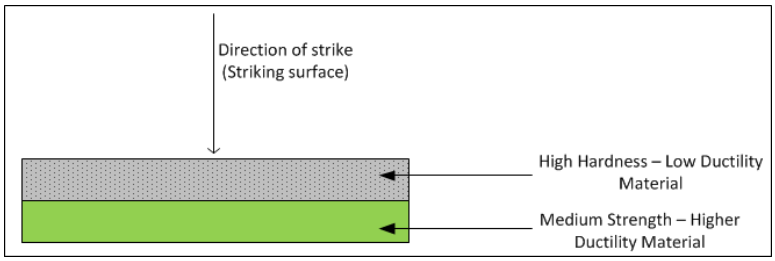

Figure 14 Example layout of a two layer ballistic plate.

While designing the first armor component, the two layer ballistic plate (for this work termed as the "biplate"), one must consider the dwell duration (described in Section 3.2 Mechanisms of an Impact Into a Hard Body Armor System), energy absorption capability, areal density, impact velocity, and projectile type (rifle, pistol, etc). These factors all contribute to the overall thickness dimensions of each layer. Alternatively, the second armor component, the underlying Kevlar® layers, requires one to consider the textile weave, fiber, binding matrix, constraint type, and layer quantities. These traits are all considered in an effort to maximize flexibility and fiber interactions and to evenly distribute loading on the textile fibers. There are many textile weave patterns to consider, and for this work a plain textile weave will be used, as shown in the schematic in Figure 15.

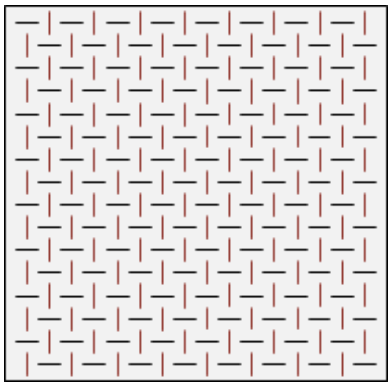

Figure 15 Schematic of a plain-woven textile - the textile weave chosen for the underlying fibers.

As one can see, the weave chosen has a nearly equal distribution of over-under fibers, called the warp and fill (Hahn, et al. 2002). This is further illustrated in Figure 16 which shows a cross-sectional view of a plain-woven textile layer.

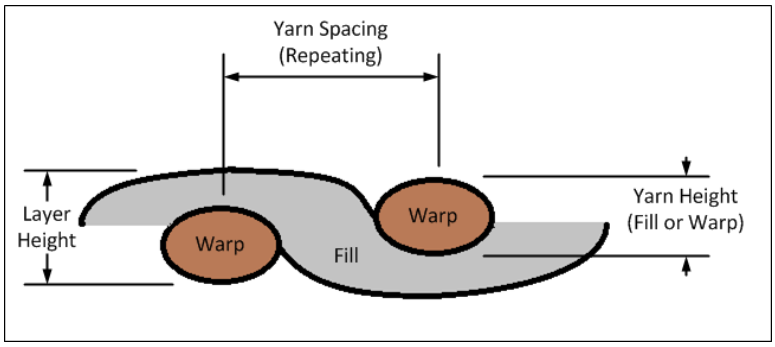

Figure 16 Plain woven textile showing the cross-section of the warp and fill.

With the basic design concept of the ballistic plate and textile determined, each of these components can now be examined and expanded upon in further detail.

5.4 Biplate Material Selection and Properties

For this work, the materials used for the biplate are aluminum-oxide (alumina, Al_2O_3) (MatWeb 2010) and aluminum (MatWeb 2010) for the upper and lower layers, respectively. Other materials considered for the biplate top layer were boron-carbide (B_4C) (MatWeb 2010) and silicon-carbide (SiC) (MatWeb 2010), and for the lower layer, both shock resistant tool steel (MatWeb 2010) and titanium alloy (MatWeb 2010) were considered. Table 10 and Table 11 show the selection criteria used to determine the two biplate materials.

Table 10 Material properties of the considered ceramics of the biplate.

Trait	B_4C	Al_2O_3	SiC
Speed of sound (m/s)	8630.7	7457.6	7906.6
Tensile strength (MPa)	172	300	340
Compressive strength (MPa)	1721	3000	3500
Modulus of resilience (kJ/m^3)	39.074	121.6	152.1
Young's modulus (GPa)	379	370	380
Poisson's ratio	0.18	0.22	0.17
Fracture toughness (MPa-m$^{1/2}$)	3.50	4.00	4.00
Mass Density (kg/m^3)	2650	3960	3070

Table 11 Material properties of the considered metallics of the biplate.

Trait	Aluminum	Steel	Titanium
Speed of sound (m/s)	5001.6	4502.5	4873.8
Ultimate strength (MPa)	572	2080	1030
Yield strength (MPa)	503	1800	930
Strain at failure (m/m)	0.110	0.100	0.140
Modulus of toughness (kJ/m^3)	59125	194000	137200
Young's modulus (GPa)	71.7	200	110
Poisson's ratio	0.33	0.290	0.33
Mass Density (kg/m^3)	2810	7830	4540

The speed of sound, a (m/s), of the material is calculated using Equation 3 (White 2006).

$$a = \sqrt{\frac{K}{\rho}}$$

Equation 3 Speed of sound in a material.

where ρ is the material density (kg/m^3), and K is the bulk modulus (Pa) and is found using Equation 4 (Ugural and Fenster 2003).

$$K = \frac{E}{3(1-2v)}$$

Equation 4 Bulk modulus of a material.

Equation 4 relates the Young's and Poisson's moduli of the material, E (Pa) and v, respectively, to find the bulk modulus. In Table 10, the modulus of resilience, U_R (J/m^3) is approximated by using Equation 5 (Norton 2006).

$$U_R \approx \frac{1}{2}\frac{S_y^2}{E}$$

Equation 5 Method for approximating the modulus of resilience.

where S_y is the yield strength (Pa) of the material.

In Table 11 the modulus of toughness, U_T (J/m^3) is approximated by using Equation 6 (Norton 2006).

$$U_T \approx \left(\frac{S_y + S_{ut}}{2}\right)\varepsilon_f$$

Equation 6 Method for approximating the modulus of toughness.

where S_{ut} is the ultimate tensile strength (Pa) of the material, and ε_f is the strain at failure of the material.

To rank and evaluate each material for use as part of body armor component, a decision matrix was developed. For each material, each trait was normalized with respect to the largest value in the category and then assigned a multiplication factor. This multiplication factor, MF (1, 2, 3, 4, or 5) is given for each trait and is based on the importance of that trait. For example, speed of sound is given a multiplication factor (MF) of 5 because it is a very important design perimeter. This multiplication factor is then multiplied to the normalized value (NV) for each material to obtain a score value (SV) for the trait in question. To find the total score, the desired large (designated as "B") and low (designed as "A") traits are totaled, where the low value sum is then subtracted

from the high value sum. Table 12 and Table 13 show the score values for materials of the top and lower layers of the biplate, respectively.

Table 12 Scoring and ranking each ceramic material for the top layer.

			B_4C		Al_2O_3		SiC	
Trait		MF	NV	SV	NV	SV	NV	SV
A	Speed of sound	5	1.00	5.00	0.86	4.32	0.92	4.58
	Density	3	0.67	2.01	1.00	3.00	0.78	2.33
Total: A		8	--	7.01	--	7.32	--	6.91
B	Tensile strength	3	0.51	1.52	0.88	2.64	1.00	3.00
	Compressive strength	4	0.49	1.97	0.86	3.42	1.00	4.00
	Modulus of resilience	4	0.26	1.03	0.80	3.20	1.00	4.00
	Young's modulus	2	0.99	1.99	0.97	1.95	1.00	2.00
	Poisson's ratio	2	0.82	1.64	1.00	2.00	0.77	1.55
	Fracture toughness	4	0.88	3.50	1.00	4.00	1.00	4.00
Total: B		19	--	11.65	--	17.21	--	18.55
Total: B - A		11	--	4.64	--	9.89	--	11.64

Table 13 Scoring and ranking each metallic material for the lower layer.

			Aluminum		Steel		Titanium	
Trait		MF	NV	SV	NV	SV	NV	SV
A	Speed of sound	2	1.00	2.00	0.90	1.80	0.97	1.94
	Density	5	0.36	1.80	1.00	5.00	0.58	2.90
Total: A		8	--	3.80	--	6.80	--	4.84
B	Modulus of toughness	4	0.30	1.20	1.00	4.00	0.71	2.84
	Young's modulus	2	0.36	0.72	1.00	2.00	0.55	1.10
	Poisson's ratio	2	1.00	2.00	0.88	1.76	1.00	2.00
	Strain to failure	4	0.79	3.16	0.71	2.84	1.00	4.00
Total: B		19	--	7.08	--	10.6	--	9.94
Total: B - A		11	--	3.28	--	3.80	--	5.10

Each material trait from Table 12 and Table 13 is normalized by using Equation 7.

$$T_i^* = \frac{T_i}{\max(T)}$$

Equation 7 Normalization equation.

where T is the respective trait and the subscript i corresponds to the material in question.

As one can see from Table 12, silicon carbide shows a favorable score, followed closely by aluminum oxide, with values of facture toughness, compression and tensile strength being very similar. Ultimately, aluminum oxide was chosen because of the low speed of sound as compared to silicon carbide. Upon a high velocity impact, the damage cone will inevitably form causing the ceramic material to fracture. Prolonged dwell duration is highly desirable and is dependent upon the speed of sound of the material; therefore, the raw score alone cannot be used as the deciding factor for material selection.

For the lower portion of the plate, aluminum is selected. Titanium alloy shows good potential as an armor material (as evaluated in Table 13) and will be examined further in future work. Steel and aluminum both ranked closely. Although tough and strong, steel is very dense, and hence if implemented, it would require a thin armor section to remain lightweight, and thus reducing layer contact areas and in turn eliminating its advantages.

5.5 Woven Textile Fiber Selection and Properties

The fiber selected for the woven underlying textile material is aramid Kevlar® 29 by DuPont. This fiber exhibits high axial strength, high transverse flexibility, low weight, and most importantly, high impact resilience (DuPont 2010). Other fibers considered were the Kevlar® 49 fiber (DuPont 2010) and the common glass fiber (Kaw 2006). Table 14 shows the properties of the three plausible fibers and Table 15 shows the fibers scored and ranked in a similar fashion that is shown Section 5.4.

Table 14 Material properties for the considered fibers.

Trait	Kevlar® 29	Kevlar® 49	Glass
Tensile strength (MPa)	3600	3600	1550
Strain at failure (m/m)	0.036	0.024	0.018
Modulus of resilience (kJ/m^3)	78072	52258	14132
Young's modulus (GPa)	83.0	124	85.0
Poisson's ratio	0.36	0.36	0.20
Mass Density (kg/m^3)	1440	1440	2500

Table 15 Scoring and ranking matrix for each fiber considered.

			Kevlar® 29		Kevlar® 49		Glass	
Trait		MF	NV	SV	NV	SV	NV	SV
A	Mass Density	4	0.57	2.28	0.57	2.28	1.00	4.00
Total A		4	--	2.28	--	2.28	--	4.00
B	Tensile strength	4	1.00	4.00	1.00	4.00	0.43	1.72
	Strain at failure	4	1.00	4.00	0.67	2.68	0.50	2.00
	Modulus of resilience	5	1.00	5.00	0.67	3.35	0.18	0.90
	Young's modulus	3	0.67	2.01	1.00	3.00	0.69	2.07
	Poisson's ratio	1	1.00	1.00	1.00	1.00	0.56	0.56
Total B		17	--	16.01	--	14.03	--	7.25
Total B-A		13	--	13.73	--	11.75	--	3.25

For Table 15, the modulus of resilience is calculated using Equation 5 shown in Section 5.4.

As shown, Kevlar® 29 significantly outranked the other two fibers. Although the Young's modulus is lower than either other fiber, Kevlar® 29 has the highest modulus of resilience, mainly because of the high strain to failure. The glass fiber did not score well because the strain to failure, tensile strength and Young's modulus are all low. This fiber also has the highest mass density of all three fibers, a very important design consideration.

5.6 Predicted Plain-Woven Textile Engineering Properties

To predict the required engineering constants of the textile, the weave type, warp/fill spacing, fiber diameter(s), denier, independent fiber properties, and fiber volume fracture, must all be considered. Table 16 shows the directional individual fiber and matrix properties used to predict the woven layer properties ((DuPont 2010),(Kaw 2006), (Hahn, et al. 2002)).

Table 16 Fiber and matrix properties used for plain weave.

Property	Kevlar® 29	Matrix
Axial modulus, (GPa)	83.0	3.4
Transverse modulus, (GPa)	2.50	3.4
Axial shear modulus, (GPa)	2.01	1.308
Transverse shear modulus, (GPa)	0.924	1.308
Axial Poisson's ratio	0.36	0.30
Transverse Poisson's ratio	0.37	0.30
Axial tensile strength, (MPa)	2760.0	72.0
Shear strength, (MPa)	21.0	34.0
Density, ρ (kg/m^3)	1440	1650

For future uses, the axial fiber direction is denoted with a 1, and the transverse directions are denoted as 2 and 3, where 3 is the out-of-plane tangent direction.

Many models exist for determining the properties of a unidirectional composite with straight fibers; however, plain-woven composites do not have straight fibers (Figure 16) (Kaw 2006). The waviness of the fibers must be accounted for to effectively determine the engineering properties of the textile.

A high denier (1500-denier, 0.11 diameter) Kevlar® 29 fiber is chosen for the textile, with the pitch set at 3.175 mm. This value was selected to create a textile with a high structural integrity (Hahn, et al. 2002). The fabric is modeled as having 12.5 threads per inch (in both fill and warp directions), which gives a fill and warp spacing of 2.032

mm. Since the pitch and warp-fill spacing has been established, the cover factor may be checked. The cover factor is the ratio of warp-fill spacing to pitch and is a method to determine if the textile is too loose or if yarn degradation has taken place in the weaving process (Tabiei and Nilakantan 2008). For a ballistic textile, the cover factor should be between 0.60 and 0.95 (Tabiei and Nilakantan 2008). In this work, the cover factor is 0.64, and therefore acceptable for a ballistic textile.

To find the textile engineering properties requires two steps. First, the effect of the angle of crimp is not considered. During these first steps, the warp, fill and matrix components are each isolated and the effective properties are found for each. The second step is to predict the engineering properties to include effect of undulation, or the angle of crimp.

Starting the process of finding the individual yarn and matrix properties, requires first that the yarn stress partitioning parameter(s), η is/are found using Equation 8 (Hahn, et al. 2002).

$$\eta_1 = 1$$

$$\eta_2 = 1$$

$$\eta_3 = 1$$

$$\eta_4 = 1$$

$$\eta_{5w} = \left(\frac{1}{4(1-\nu_{m23})}\right)\left(3-4\nu_{m23}\frac{G_{m23}}{G_{w23}}\right)$$

$$\eta_{5f} = \left(\frac{1}{4(1-\nu_{m23})}\right)\left(3-4\nu_{m23}\frac{G_{m23}}{G_{f23}}\right)$$

$$\eta_{6w} = \frac{1}{2}\left(1+\frac{G_{m12}}{G_{w12}}\right)$$

$$\eta_{6f} = \frac{1}{2}\left(1 + \frac{G_{m12}}{G_{f12}}\right)$$

Equation 8 Equations for finding the stress partitioning parameters of the textile.

where *w* is the warp, *f* is the fill, and *m* is the matrix. This same notation, used as subscripts will be used throughout the calculation.

The bulk modulus, *K* (Pa) of the yarn(s) and matrix is now found using Equation 9 (Hahn, et al. 2002).

$$K_{wy} = \frac{E_{w2}G_{w23}}{4G_{w23} - E_{w2} - 4G_{w23}\frac{E_{w2}}{E_{w1}}\left(\nu_{w23}\right)^2}$$

$$K_{fy} = \frac{E_{f2}G_{f23}}{4G_{f23} - E_{f2} - 4G_{f23}\frac{E_{f2}}{E_{f1}}\left(\nu_{f23}\right)^2}$$

$$K_m = \frac{G_{m12}}{1 - 2\nu_{m12}}$$

Equation 9 Equations used to determine the bulk modulus of the yarns and matrix.

The remaining yarn stress partitioning parameters may now be found by using Equation 10.

$$\eta_{8w} = \left(\frac{1}{2\left(1-\nu_{m12}\right)}\right)\left(1 + \frac{G_{m12}}{K_w}\right)$$

$$\eta_{8f} = \left(\frac{1}{2\left(1-\nu_{m12}\right)}\right)\left(1 + \frac{G_{m12}}{K_f}\right)$$

Equation 10 Additional yarn stress partitioning parameters.

Assuming that the matrix does not contribute to the total thickness of the textile, and that all gaps in the weave are filled by the fill or the warp, then the area of the warp (and fill) may be found using Equation 11 (Hahn, et al. 2002).

$$W_g = h_f$$

$$a_w = L_w - W_g$$

$$F_g = h_w$$

$$a_f = L_f - F_g$$

Equation 11 Method for finding the area of the warp (and fill).

where W_g is the gap caused by the warp, h_f is the diameter of the fill, F_g is the gap caused by the fill, h_w is the diameter of the warp, L_f is the fill spacing, and L_w is the warp spacing.

The volume occupied, V by the various components may be found by using Equation 12 (Hahn, et al. 2002).

$$V_{yarns} = 0.5$$

$$V_{intervoid} = 0$$

$$V_{intermatrix} = V_{yarns} - V_{intervoid}$$

$$V_{wy} = \frac{2h_w}{\pi T_T} \sin\left(\frac{a_w}{2L_w}\right)$$

$$V_{fy} = \frac{2h_f}{\pi T_T} \sin\left(\frac{a_f}{2L_f}\right)$$

$$V_y = V_{wy} + V_{fy}$$

$$V_f = \frac{V_{yarns}}{V_y}$$

$$V_{intravoid} = 0$$

$$V_{ym} = 1 - V_f - V_{intravoid}$$

$$V_{im} = V_{inermatrix} - V_y V_{ym}$$

Equation 12 Equations used to determine the volume occupied by the various components.

where *wy* is the warp yarn, *fy* is the fill yarn, *im* is the interyarn matrix, T_T is the total thickness of the textile, and V_f is the fiber volume fraction.

Now, with the stress partitioning factors, bulk modulus, and occupied volumes calculated, the individual yarn properties may be predicted. First, the axial Young's modulus, E_1 (Pa) of the warp and fill is determined by using Equation 13 (Hahn, et al. 2002).

$$E_{1w} = \left(\frac{1}{V_f + \eta_1 V_{ym}} \right) \left(V_{xf} E_{w1} + \eta_1 V_{ym} E_{m1} \right)$$

$$E_{1f} = \left(\frac{1}{V_f + \eta_1 V_{ym}} \right) \left(V_{xf} E_{f1} + \eta_1 V_{ym} E_{m1} \right)$$

Equation 13 Equations to determine the Young's modulus of the yarns.

Two of the six Poisson's ratios, *v* for the warp and fill may be determined using Equation 14 (Hahn, et al. 2002).

$$\nu_{12w} = \left(\frac{1}{V_f + \eta_2 V_{ym}}\right)\left(V_{xf}\nu_{w12} + \eta_2 V_{ym}\nu_{m12}\right)$$

$$\nu_{13w} = \nu_{12w}$$

$$\nu_{12f} = \left(\frac{1}{V_f + \eta_2 V_{ym}}\right)\left(V_{xf}\nu_{f12} + \eta_2 V_{ym}\nu_{m12}\right)$$

$$\nu_{13f} = \nu_{12f}$$

Equation 14 Equations to find the Poisson's ratios for the yarns.

Now, all three of the yarn shear moduli, G (Pa) may be determined by using Equation 15 (Hahn, et al. 2002).

$$G_{12w} = \frac{V_f + \eta_{w6} V_{ym}}{\frac{V_f}{G_{w12}} + \frac{\eta_{w6} V_{ym}}{G_{m12}}}$$

$$G_{13w} = G_{12w}$$

$$G_{23w} = \frac{V_f + \eta_{w5} V_{ym}}{\frac{V_f}{G_{w23}} + \frac{\eta_{w5} V_{ym}}{G_{m23}}}$$

$$G_{12f} = \frac{V_f + \eta_{fw6} V_{ym}}{\frac{V_f}{G_{f12}} + \frac{\eta_{f6} V_{ym}}{G_{m12}}}$$

$$G_{13f} = G_{12f}$$

$$G_{23f} = \frac{V_f + \eta_{f5} V_{ym}}{\frac{V_f}{G_{f23}} + \frac{\eta_{f5} V_{ym}}{G_{m23}}}$$

Equation 15 Equations for determine the three shear moduli of the yarns.

The bulk modulus, K (Pa) for the fill and warp fibers may be determined using Equation 16 (Hahn, et al. 2002).

$$K_w = \frac{V_f + \eta_{w8} V_{ym}}{\frac{V_f}{K_{wy}} + \frac{\eta_{w8} V_{ym}}{K_m}}$$

$$K_f = \frac{V_f + \eta_{f8} V_{ym}}{\frac{V_f}{K_{fy}} + \frac{\eta_{f8} V_{ym}}{K_m}}$$

$$M_w = 1 + \frac{4K_w (\nu_{12w})^2}{(E_{1w})^2}$$

$$M_f = 1 + \frac{4K_f (\nu_{12f})^2}{(E_{1f})^2}$$

Equation 16 Remaining yarn bulk moduli equations.

The remaining two fill and warp Young's moduli, E (Pa) may be determined using Equation 17 (Hahn, et al. 2002).

$$E_{2w} = \frac{4K_w G_{23w}}{K_w + M_w G_{23w}}$$

$$E_{3w} = E_{2w}$$

$$E_{2f} = \frac{4K_f G_{23f}}{K_f + M_f G_{23f}}$$

$$E_{3f} = E_{2f}$$

Equation 17 Remaining Young's moduli equations for the yarns.

In Equation 17, the subscripts 2 and 3 correspond to the tangent yarn directions, where the 3 is through the thickness of the yarn.

The remaining four Poisson's ratios, v for each of the yarns, and the three remaining Poisson's ratios for the matrix may now be determined using Equation 18 (Hahn, et al. 2002).

$$v_{23w} = \frac{E_{2w}}{2G_{23w}} - 1$$

$$v_{21w} = \frac{E_{2w} v_{12w}}{E_{1w}}$$

$$v_{31w} = \frac{E_{3w} v_{13w}}{E_{1w}}$$

$$v_{32w} = \frac{E_{3w} v_{23w}}{E_{2w}}$$

$$v_{23f} = \frac{E_{2f}}{2G_{23f}} - 1$$

$$v_{21f} = \frac{E_{2f} v_{12f}}{E_{1f}}$$

$$v_{31f} = \frac{E_{3f} v_{13f}}{E_{1f}}$$

$$v_{32f} = \frac{E_{3f} v_{23f}}{E_{2f}}$$

$$v_{21m} = \frac{E_{m2} v_{m12}}{E_{m1}}$$

$$v_{31m} = \frac{E_{m3} v_{m13}}{E_{m1}}$$

$$v_{32m} = \frac{E_{m3} v_{m23}}{E_{m2}}$$

Equation 18 Remaining equations for the Poisson's ratios of the fill, warp, and matrix.

The individual yarn (warp and fill) and matrix compliance matrices, $[S]$ may be populated by the following Equation 19 (Hahn, et al. 2002) (Kaw 2006).

$$[S_i]=\begin{bmatrix} \frac{1}{E_{1i}} & -\frac{\nu_{12i}}{E_{1i}} & -\frac{\nu_{13i}}{E_{1i}} & 0 & 0 & 0 \\ -\frac{\nu_{12i}}{E_{1i}} & \frac{1}{E_{2i}} & -\frac{\nu_{23i}}{E_{2w}} & 0 & 0 & 0 \\ -\frac{\nu_{13i}}{E_{1i}} & -\frac{\nu_{23i}}{E_{2w}} & \frac{1}{E_{3i}} & 0 & 0 & 0 \\ 0 & 0 & 0 & \frac{1}{G_{23i}} & 0 & 0 \\ 0 & 0 & 0 & 0 & \frac{1}{G_{13i}} & 0 \\ 0 & 0 & 0 & 0 & 0 & \frac{1}{G_{12i}} \end{bmatrix}$$

Equation 19 Equation to develop the individual yarn and matrix compliance matrix.

In general, the inverse of the compliance matrix is the stiffness matrix, and can be calculated for each yarn and matrix by using Equation 20 (Kaw 2006).

$$[C_i]=[S_i]^{-1}$$

$$[S_i]=[C_i]^{-1}$$

Equation 20 Determining the individual yarn and matrix stiffness matrix.

The subscript *i* is a general notation used to represent the warp (*w*), fill (*f*) or matrix (*m*).

The effect of the yarn crimp angle, or the yarn undulations has not yet been considered. This effect changes the overall value of the engineering constants, and must be considered for an accurate prediction. To consider the undulation effects, first the geometric efficiency values, *V* must be calculated for each yarn in each direction (both weave directions). This is done by the following Equation 21 (Hahn, et al. 2002).

$$V_{1w} = \frac{1}{L_f}\int_0^{L_f} \cos\left[2\left(a\tan\left(\frac{\pi}{2}\frac{h_f}{L_f}\sin\left(\frac{\pi x}{L_f}\right)\right)\right)\right]dx$$

$$V_{2w} = \frac{1}{L_f}\int_0^{L_f} \cos\left[4\left(a\tan\left(\frac{\pi}{2}\frac{h_f}{L_f}\sin\left(\frac{\pi x}{L_f}\right)\right)\right)\right]dx$$

$$V_{1f} = \frac{1}{L_w}\int_0^{L_w} \cos\left[2\left(\arctan\left(-\frac{\pi}{2}\frac{h_w}{L_w}\sin\left(\frac{\pi y}{L_w}\right)\right)\right)\right]dy$$

$$V_{2f} = \frac{1}{L_w}\int_0^{L_w} \cos\left[4\left(\arctan\left(-\frac{\pi}{2}\frac{h_w}{L_w}\sin\left(\frac{\pi y}{L_w}\right)\right)\right)\right]dy$$

Equation 21 Method used to determine the geometric efficiency factors.

In Equation 21, the h_w (h_f) and L_w (L_f) terms represent the height of the warp (or fill), and warp (or fill) spacing, respectively. Additionally, the *x* and *y* directions correspond to the two weave directions.

The invariants of the stiffness matrices found in Equation 20 for the fill, warp and matrix may now be determined using Equation 22 (Hahn, et al. 2002).

$$U_{1i} = \frac{1}{8}\left(3C_{(1,1)i} + 3C_{(3,3)i} + 2C_{(1,3)i} + 4C_{(5,5)i}\right)$$

$$U_{2i} = \frac{1}{2}\left(C_{(1,1)i} - C_{(3,3)i}\right)$$

$$U_{3i} = \frac{1}{8}\left(C_{(1,1)i} + C_{(3,3)i} - 2C_{(1,3)i} - 4C_{(5,5)i}\right)$$

$$U_{4i} = \frac{1}{8}\left(C_{(1,1)i} + C_{(3,3)i} + 6C_{(1,3)i} - 4C_{(5,5)i}\right)$$

$$U_{5i} = \frac{1}{8}\left(C_{(1,1)i} + C_{(3,3)i} - 2C_{(1,3)i} - 4C_{(5,5)i}\right)$$

$$U_{6i} = \frac{1}{2}\left(C_{(1,2)i} + C_{(2,3)i}\right)$$

$$U_{7i} = \frac{1}{2}\left(C_{(1,2)i} - C_{(2,3)i}\right)$$

$$U_{8i} = \frac{1}{2}\left(C_{(4,4)i} + C_{(6,6)i}\right)$$

$$U_{9i} = \frac{1}{2}\left(C_{(4,4)i} - C_{(6,6)i}\right)$$

Equation 22 Equations for determining the invariants of the stiffness matrix components.

With the invariants determined, using Equation 22 and the geometric efficiency values calculated in Equation 21, the textile stiffness matrix, $[C_T]$ may be formed by using Equation 23 (Hahn, et al. 2002).

$$C_{(1,1)T} = V_{wy}\left(U_{1w} + V_{1w}U_{2w} + V_{2w}U_{3w}\right) + V_{fy}C_{(2,2)f} + V_{im}C_{(1,1)m}$$

$$C_{(2,2)T} = V_{fy}\left(U_{1f} + V_{1f}U_{2f} + V_{2f}U_{3f}\right) + V_{wy}C_{(2,2)w} + V_{im}C_{(2,2)m}$$

$$C_{(3,3)T} = V_{wy}\left(U_{1w} - V_{1w}U_{2w} + V_{2w}U_{3w}\right) + V_{fy}\left(U_{1f} - V_{1f}U_{2f} + V_{2f}U_{3f}\right) + V_{im}C_{(3,3)m}$$

$$C_{(1,2)T} = V_{wy}\left(U_{6w} + V_{1w}U_{7w}\right) + V_{fy}\left(U_{6f} + V_{1f}U_{7f}\right) + V_{im}C_{(1,2)m}$$

$$C_{(1,3)T} = V_{wy}\left(U_{4w} - V_{1w}U_{3w}\right) + V_{fy}\left(U_{6f} - V_{2f}U_{7f}\right) + V_{im}C_{(1,3)m}$$

$$C_{(2,3)T} = V_{wy}\left(U_{6w} - V_{2w}U_{7w}\right) + V_{fy}\left(U_{4f} - V_{1f}U_{3f}\right) + V_{im}C_{(2,3)m}$$

$$C_{(4,4)T} = V_{wy}\left(U_{8w} + V_{1w}U_{9w}\right) + V_{fy}\left(U_{5f} - V_{2f}U_{3f}\right) + V_{im}C_{(4,4)m}$$

$$C_{(5,5)T} = V_{wy}\left(U_{5w} - V_{2w}U_{3w}\right) + V_{fy}\left(U_{8f} + V_{1f}U_{9f}\right) + V_{im}C_{(5,5)m}$$

$$C_{(6,6)T} = V_{wy}\left(U_{8w} - V_{1w}U_{9w}\right) + V_{fy}\left(U_{8f} - V_{1f}U_{9f}\right) + V_{im}C_{(6,6)m}$$

Equation 23 Equations for developing the textile stiffness matrix.

where *wy* is the warp yarn volume, *fy* is the fill yarn volume, and *im* is the intermatrix yarn volume.

Now that the undulation effects have been accounted for, and the plain-weave textile stiffness matrix $[C_T]$ has been populated, Equation 20 may be used to determine the textile compliance matrix $[S_T]$, and in turn the various textile engineering constants may be predicted (Kaw 2006). The three Young's moduli of the textile may be determined using Equation 24.

$$E_{1T} = \frac{1}{S_{(1,1)T}}$$

$$E_{2T} = \frac{1}{S_{(2,2)T}}$$

$$E_{3T} = \frac{1}{S_{(3,3)T}}$$

Equation 24 Equations for the three Young's moduli of the textile.

The six Poisson's ratios for the textile are calculated by using Equation 25 (Kaw 2006).

$$\nu_{12T} = -\frac{S_{(1,2)T}}{S_{(1,1)T}}$$

$$\nu_{12T} = -\frac{S_{(1,3)T}}{S_{(1,1)T}}$$

$$\nu_{12T} = -\frac{S_{(1,3)T}}{S_{(1,1)T}}$$

$$\nu_{21T} = -\frac{S_{(1,2)T}}{S_{(2,2)T}}$$

$$\nu_{23T} = -\frac{S_{(2,3)T}}{S_{(2,2)T}}$$

$$\nu_{31T} = -\frac{S_{(1,3)T}}{S_{(3,3)T}}$$

$$\nu_{32T} = -\frac{S_{(2,3)T}}{S_{(3,3)T}}$$

Equation 25 Equations used to determine the six Poisson's ratios of the textile.

Lastly, the textile shear moduli are found using Equation 26 (Kaw 2006).

$$G_{23T} = \frac{1}{S_{(4,4)T}}$$

$$G_{31T} = \frac{1}{S_{(5,5)T}}$$

$$G_{12T} = \frac{1}{S_{(6,6)T}}$$

Equation 26 Equations used for the three shear modulus of the textile.

The number subscripts in parenthesis correspond to the respective element location of the textile compliance matrix.

The calculated textile stiffness matrix, $[C_T]$ is shown in Equation 27 and the compliance matrix $[S_T]$ is shown in Equation 28.

$$[C_T] = \begin{bmatrix} 23.7707 & 1.5505 & 1.5315 & 0 & 0 & 0 \\ 1.5505 & 23.7704 & 1.5311 & 0 & 0 & 0 \\ 1.5315 & 1.5311 & 3.7015 & 0 & 0 & 0 \\ 0 & 0 & 0 & 0.8624 & 0 & 0 \\ 0 & 0 & 0 & 0 & 0.8624 & 0 \\ 0 & 0 & 0 & 0 & 0 & 1.6382 \end{bmatrix} \text{GPa}$$

Equation 27 Generated Kevlar 29 textile stiffness matrix.

$$[S_T] = \begin{bmatrix} 0.0433 & -0.0017 & -0.0172 & 0 & 0 & 0 \\ -0.0017 & 0.0433 & -0.0172 & 0 & 0 & 0 \\ -0.0172 & -0.0172 & 0.2844 & 0 & 0 & 0 \\ 0 & 0 & 0 & 1.1596 & 0 & 0 \\ 0 & 0 & 0 & 0 & 1.1596 & 0 \\ 0 & 0 & 0 & 0 & 0 & 0.6104 \end{bmatrix} \frac{1}{\text{GPa}}$$

Equation 28 Generated Kevlar 29 textile compliance matrix.

Table 17 shows the plain-woven predicted textile engineering constants calculated from Equation 24, Equation 25, and Equation 26.

Table 17 Engineering constants of the Kevlar 29 textile.

Young's Modulus, E_1 (GPa)	23.1007
Young's Modulus, E_2 (GPa)	23.1007
Young's Modulus, E_3 (GPa)	3.5163
Poisson's ratio, ν_{12}	0.03963
Poisson's ratio, ν_{23}	0.3972
Poisson's ratio, ν_{31}	0.06048
Shear Modulus, G_{12} (GPa)	1.6382
Shear Modulus, G_{23} (GPa)	0.86236
Shear Modulus, G_{13} (GPa)	0.86236

As shown, the out-of-plane Young's modulus is much lower than the two tangent direction Young's moduli. This is expected given the typical physical response of a textile material. Additionally, the shear moduli are all low, contributing to the flexibility of the textile, and further confirming the predicted results.

5.7 Dynamic Material Properties and Failure Criteria

Once impacted, the loading of the armor system and projectile is expected to be that of a high strain-rate dynamic response. Static or quasi-static loading is not expected given the short impact times and high impact speeds. Because of this expected response, dynamic material properties and failure criteria for the aluminum, aluminum-oxide, lead,

copper, and Kevlar® must be considered. Additionally, because the deformation is also expected to be both elastic and plastic, effects such as strain hardening must be considered for aluminum, lead and copper.

The dynamic properties used to model the aluminum and lead are in the form of a Steinberg-Guinan strength model (SAS IP, Inc. 2009). This model takes into account the high strain plastic deformation and is commonly used for impact analysis. The material properties are shown in Table 18 (aluminum – AL7075-T6) and Table 19 (lead - LEAD) and were obtained via the ANSYS 12.1 Engineering Properties Library (SAS IP, Inc. 2009).

Table 18 Dynamic material properties used to model aluminum.

Density (kg/m^3)	2804
Shear Modulus (GPa)	26.7
Steinberg Guinan Strength	
Initial yield stress (MPa)	420
Maximum yield stress (MPa)	810
Hardening constant	965
Hardening exponent	0.1
dG/dP	1.741
dG/dT (MPa/K)	−16.450
dY/dP	0.02788
Melting Temperature (K)	1220
Shock Equation of State (EOS)	
Gruneisen Coefficient	2.2
Parameter C1 (m/s)	5200
Parameter S1	1.36

Table 19 Dynamic material properties used to model lead.

Density (kg/m^3)	25105
Shear Modulus (GPa)	8.6
Steinberg Guinan Strength	
Initial yield stress (MPa)	8.0
Maximum yield stress (MPa)	100
Hardening constant	110
Hardening exponent	0.52
dG/dP	1
dG/dT (MPa/K)	−9976
dY/dP	0.0009304
Melting Temperature (K)	760
Shock Equation of State (EOS)	
Gruneisen Coefficient	2.74
Parameter C1 (m/s)	2006
Parameter S1	1.429

The dynamic material properties chosen for the plastic deformation of the copper jacket is that of a multilinear isotropic hardening model (SAS IP, Inc. 2009). Again, the properties for this material were obtained via the ANSYS 12.1 Engineering Properties Library (COPPER) (SAS IP, Inc. 2009) and are shown in Table 20.

Table 20 Dynamic material properties used to model copper.

Density (kg/m^3)	8900
Shear Modulus (GPa)	46.4
Multilinear Isotropic Hardening Values	
Plastic Strain 1 (m/m)	0
Plastic Strain 2 (m/m)	0.3
Plastic Strain 3 (m/m)	1.5
Stress 1 (MPa)	120
Stress 2 (MPa)	450
Stress 3 (MPa)	450
Scale	1
Offset	0
Shock Equation of State (EOS)	
Gruneisen Coefficient	2
Parameter C1 (m/s)	3958
Parameter S1	1.497

Aluminum-oxide does not plastically deform like the other three materials. However, the dynamic response will differ from when statically loaded. To simulate the response of aluminum-oxide under dynamic loading, a Johnson-Holmquist strength model is used (SAS IP, Inc. 2009). Like the other three material properties shown thus far, ANSYS 12.1 Engineering Properties Library (AL2O3-99.7) is used to obtain the values shown in Table 21 (SAS IP, Inc. 2009).

Table 21 Dynamic material properties used to model Aluminum Oxide.

Density (kg/m^3)	3800
Shear Modulus (GPa)	46.4
Bulk Modulus (GPa)	200
Johnson-Holmquist Strength Continuous	
Hugoniot Elastic Limit (MPa)	5900
Intact Strength Constant	0.989
Intact Strength Exponent	0.3755
Strain Rate Constant	0
Fracture Strength Constant	0.77
Fracture Strength Exponent	1
Maximum Fracture Strength Ratio	0.5
Damage Constant 1	0.01
Damage Constant 2	1
Bulking Constant	1
Hydrodynamic Tensile Limit (MPa)	−29
Polynomial Equation of State	
Parameter A1 (GPa)	200
Parameter T1 (GPa)	200

The static failure (and quasi-static failure) of the Kevlar® woven and laminated fibers is well researched and documented. However, little is known about the plastic deformation and dynamic failure of a Kevlar® fiber. This is primarily because of the differences in fiber, matrix, weave and impact types. Research has shown that while impacted in the transverse direction, plain-woven Kevlar fibers do indeed have a linear stress-strain curve (in the warp and fill or tangent directions) to failure (Gellert, Pattie and

Woodard 1998). These same tests also show that plain-woven Kevlar fabrics appear to have a ballistic strain value that is much higher than the static strain to failure value (Berg, et al. 2005). In addition to Table 17, the failure parameters of the plain-woven Kevlar® 29 fabric are shown in Table 22.

Table 22 Dynamic failure properties of the woven Kevlar fabric.

Apparent ballistic axial strain to failure	0.15
Assumed ballistic shear strain to failure	1×10^{20}

As shown in Table 22, the apparent ballistic axial and shear strain values are relatively high, especially compared to static test values. The textile is not expected to fail from being twisted or bent, as the textile is highly ductile in the out-of-plane directions. The direction of observed failure is in the direction of weave, or the tangent directions.

The behavior of the fibers is shown to be that of a viscoelastic material (Tabiei and Nilakantan 2008). The strain value at failure is highly dependent upon the applied strain rate and other constants that must be determined experientially. Again, because of vast differences in fiber type, matrix type, weave patterns and impact velocities, these constants required for the typically used viscoelastic spring-dashpot model are not well known (Tabiei and Nilakantan 2008).

What is known about the failure of woven Kevlar® fabric panels is that when impacted transversely and directly at a high velocity, the strain and stress becomes localized to a small area and cannot be transferred to the surrounding fibers, causing the impacted fibers to be sheared (literally cut) in the normal (out-of-plane direction) direction (Tabiei and Nilakantan 2008). On the contrary, when impacted at a low velocity, the fabric has time to deflect in the transverse direction which causes the projectile to become entangled in the fibers of the fabric, thereby increasing the fiber

contacts. The failure mode in these low velocity impacts is prominently that of yarn pullout, excessive creasing and stretching (Tabiei and Nilakantan 2008). These failure traits will be examined in the analysis to confirm the accuracy of the material response.

CHAPTER 6 BIPLATE DESIGN AND ANALYSIS

An important design parameter to the biplate is determining the individual layer thicknesses. One may start with the assumption of equal thickness of the aluminum-oxide and aluminum layers for optimal performance. However, we will later show that this is not the case. Once impacted, the failure of the ceramic is nearly certain. Before and during failure the ceramic portion of the plate serves to prolong the dwell duration, degrade the projectile tip and distribute the impact forces to the lower aluminum. The aluminum then elastically and plastically deforms to absorb the remaining energy.

6.1 Biplate Finite Element Analysis – Setup

To aid in the design of the ballistic plate, finite element analysis using ANSYS Workbench 12.1 Explicit Dynamics (with the AUTODYN solver) is conducted (SAS IP, Inc. 2009). While maintaining a constant overall thickness, six different plate thickness combinations (see Figure 17) were imported into ANSYS and impacted with a rigid sphere travelling at a set initial velocity of 940 m/s.

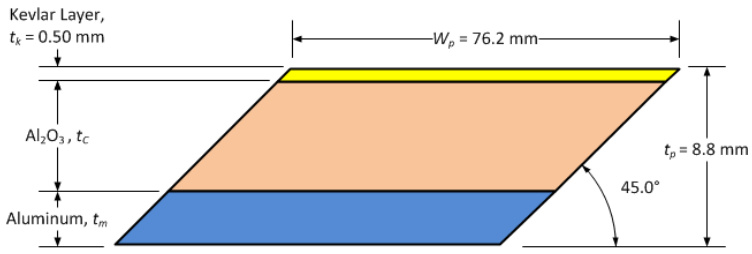

Figure 17 General cross section of the biplate (not drawn to scale).

For this work, the overall biplate thickness (t_p) and width (W_p) are fixed at 8.8 mm and 76.2 mm, respectively (to help accomplish the objectives listed in Table 8). The thicknesses of the aluminum (t_m) and aluminum-oxide (t_c) were adjusted six different times. As shown in Figure 17, a layer of plain-woven (t_k, 0.5 mm thick) Kevlar 29® fabric is bonded to the surface of the top plate. This is to contain any ceramic fragments that may separate from the aluminum-oxide once impacted, and to increase the plate multiple-hit capability. The sphere impact direction is normal to (0° angle of incidence) the exposed face of the top plate (Figure 18).

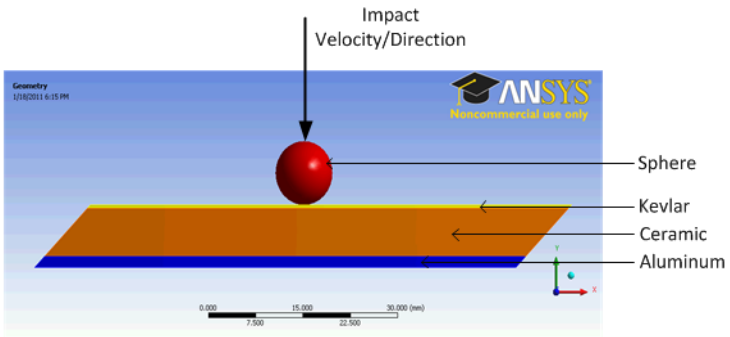

Figure 18 Sphere, Kevlar, ceramic, and aluminum components of the biplate (1.5 mm aluminum thickness shown).

The material properties used for the aluminum and aluminum-oxide are shown in Table 18 and Table 21, respectively. The sphere was modeled with a diameter of 9 mm, using the mass properties of steel, and with a rigid physical behavior (no deflection can occur within the sphere body). This is done so that the only method of system energy transfer from the projectile to the ballistic plate is via strain energy and plastic deformation/material fracture of the plate components. Both the biplate and the sphere were meshed using hexagonal (hex8) and tetrahedral (tet4) elements with a medium relevance center with a value of 50. The connection(s) between the Kelvar® sheet,

aluminum-oxide and aluminum are bonded, whereas the connection(s) between the sphere and all other bodies is/are frictionless. The finite element model of the ballistic plate was rigidly constrained along the plate edges. This is done so that the biplate may not move within the reference plane, and so the projectile may perforate the plate, if physically possible. Figure 19 and Figure 20 each show an image of one of the six meshed models, and Table 23 lists the simulation number with the corresponding thickness values, meshed nodes, elements, and the average element aspect ratio.

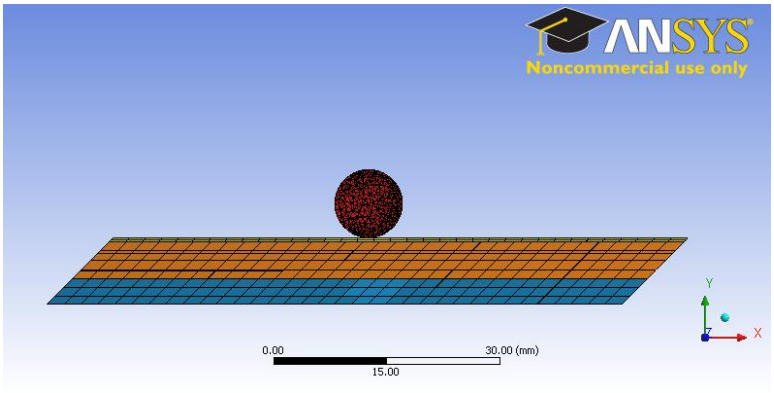

Figure 19 Screen image of a meshed model, side cross-section view shown.

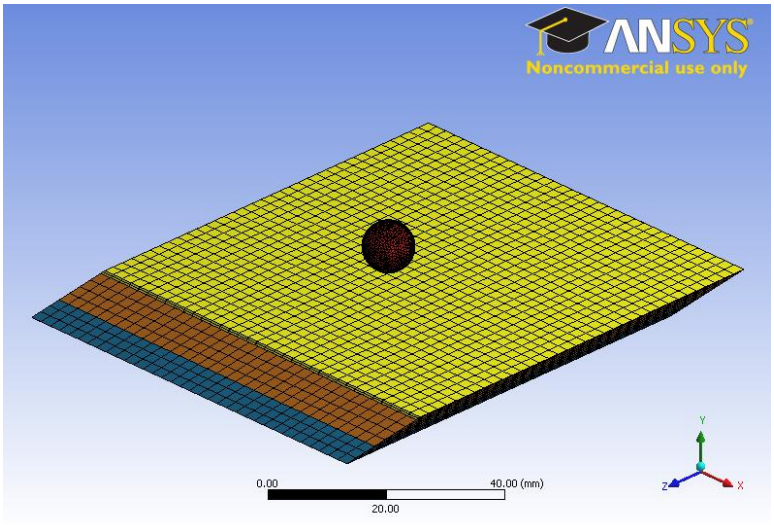

Figure 20 Screen image of a meshed model, orthogonal view shown.

Table 23 Number of simulations with layer thickness, and mesh information.

Test #	Thickness (mm)		Mesh details		
	Aluminum	Al_2O_3	Nodes	Elements	Aspect ratio
1	0.00	8.30	16971	22501	2.398
2	1.50	6.80	20188	24271	2.401
3	3.30	5.00	18741	22919	2.376
4	4.15	4.15	19975	24137	2.396
5	6.80	1.50	20179	24223	2.403
6	8.30	0.00	16960	22440	2.404

As one can see from Table 23, the amount of required nodes and elements changed significantly between each simulation, however the aspect ratio of the element dimensions were kept about the same for each simulation.

6.2 Biplate Finite Element Analysis - Results

For the FEA, the deflection and the equivalent stress was recorded for all bodies. Additionally, the translational average body velocity was recorded for the impacting sphere. Figure 21 shows a screen shot of the cross-section of one of the six finite element models at various analysis times, captured from the solution video.

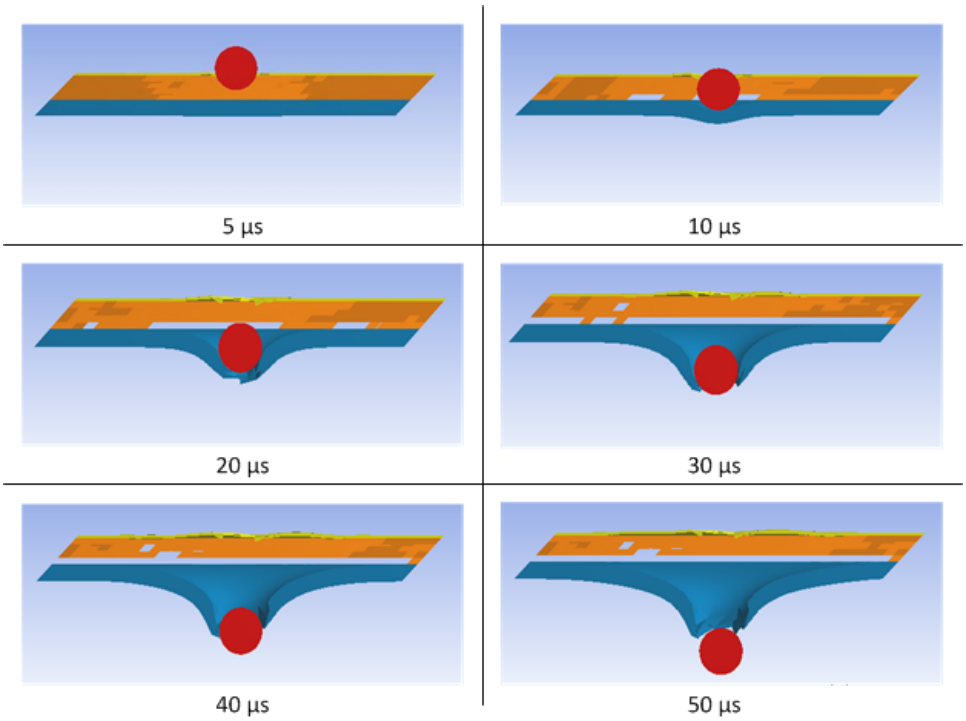

Figure 21 Cross-sectional view of the impact at various times.

A similar response to what is shown in Figure 21 was recorded for the other five finite element simulations. The aluminum-oxide failed due to fracture whereas the aluminum underwent elastic, then plastic deformation, and ultimately was perforated by the sphere. The top Kevlar® appeared to serve the design purpose of catching the fragments, although this was difficult to confirm. Regardless, the Kevlar® did not seem to contribute to the slowing of the sphere.

Once the finite element modeling was complete, the results could be tabulated. As mentioned, the translational velocity of the sphere was recorded during the impact. Generated in MATLAB® (TheMathWorks, Inc. 2008), Figure 22 shows the sphere velocity of each of the six simulations during the entire impact time. Notice that up until approximately 12 µs, the velocity of the projectile is nearly the same for each simulation, and varies from that point until the end of the simulation(s) for each combination.

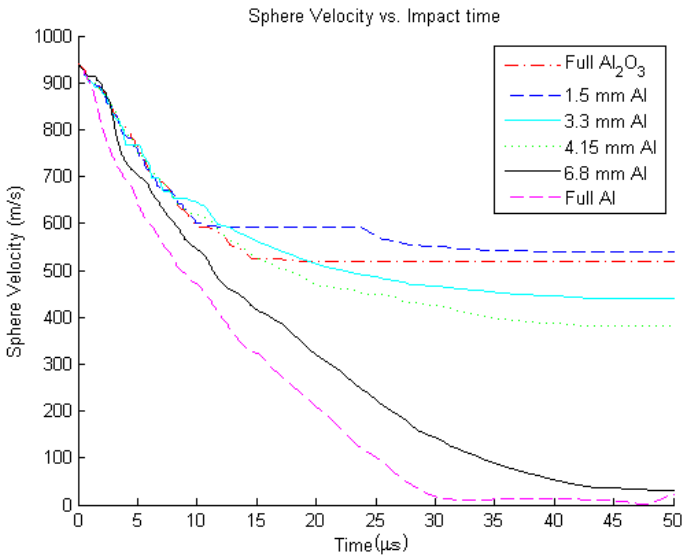

Figure 22 Average mass projectile velocities vs. impact time.

The translational velocity is also used to determine the energy absorbed by the ballistic plate. Assuming that the projectile remains intact (as one mass, and in this case it does), the amount of energy absorption for the biplate, E_P (J), can be related to the projectile mass (kg) and velocity (m/s) by using Equation 29 (David, Gao and Zheng 2009).

$$E_P = \tfrac{1}{2} m\left(V_{in}{}^2 - V_{re}{}^2\right)$$

Equation 29 Kinetic energy absorption of the ballistic plate.

where V_{in} is the initial projectile velocity, and V_{re} is the residual projectile velocity.

Table 24 shows the FEA results with the calculated energy absorption for the various biplate configurations (with an initial sphere kinetic energy of 2647.6 J).

Table 24 Finite element analysis results for the biplate.

Test #	Thickness (mm)		Finite Element Analysis Results		
	Aluminum	Al_2O_3	Cycles to completion	Residual Velocity (m/s)	Energy absorption (J)
1	0.00	8.30	4351	519.04	920.07
2	1.50	6.80	2914	540.75	885.60
3	3.30	5.00	2916	441.60	1031.5
4	4.15	4.15	2914	380.70	1106.5
5	6.80	1.50	2914	29.80	1322.3
6	8.30	0.00	2925	0.00	1323.6

As shown, the residual velocity of the projectile is not a linear response for the various configurations, and thus neither is the energy absorption.

Figure 23 shows the energy absorption capability of the biplate as a function of the overall aluminum thickness value. In this figure, the recorded FEA results are shown with square data points and these values are then interpolated using a cubic-spline model.

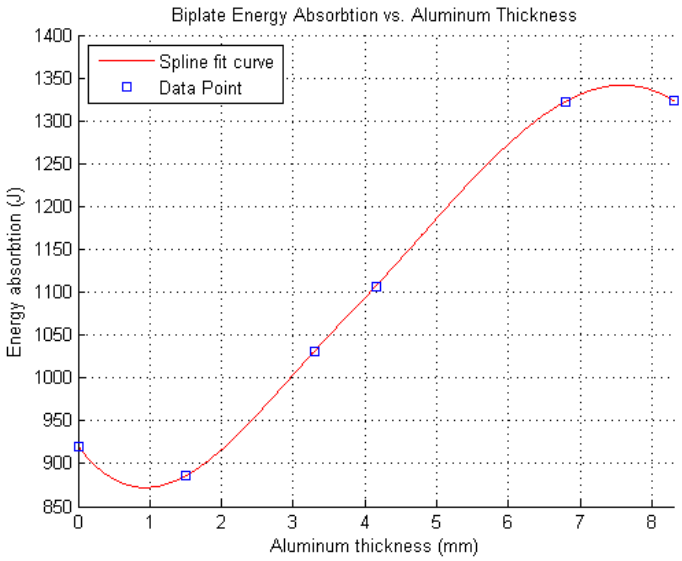

Figure 23 Calculated energy absorption vs. aluminum thickness.

As mentioned, the energy absorption value at the various thicknesses is not linear. According to the cubic-spline model, the minimum and maximum energy absorption

values would occur at approximately 0.75 and 7.5 mm of aluminum thicknesses, respectively. It is thought that this is related to the lack of layer contact area interactions in assisting distribution of the dynamic loads.

6.3 Biplate Analytical Analysis

In addition to energy absorption, the ballistic biplate also serves to degrade the projectile. Because the impacting sphere is modeled as rigid, this behavior is not represented in the FEA shown in Section 6.1. To relate the ability of the biplate to degrade the projectile tip with the thickness of the top layer, the material speed of sound is considered. Recall that the dwell duration is the time that the ceramic remains stationary, while the compressive shock wave propagates at the speed of sound (Section 3.2). The time to form the damage cone is related to both the speed of sound of the material and the conoid angle as shown in Figure 24.

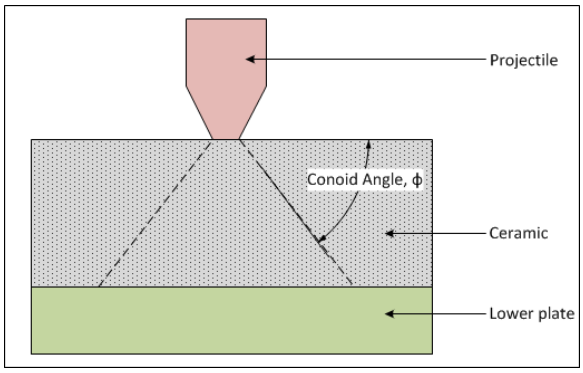

Figure 24 Drawing of the formed damage cone with conoid angle.

The conoid angle, ϕ (radians), is directly dependent upon the impact velocity V_{in} (m/s) and can be approximated using Equation 30 (Fellows and Barton 1999).

$$\phi = \left(\frac{V_{in} - 220}{780}\right)\frac{34\pi}{180} + \frac{34\pi}{180}$$

Equation 30 Conoid angle given impact velocity.

Equation 30 is only valid for impact velocities varying from 220 to 1000 m/s. For impact velocities over 1000 m/s, a constant conoid angle of 68° may be used (Fellows and Barton 1999).

The distance D_S (m) that the shock wave must propagate through to form the damage cone is governed by the conoid angle and the thickness of the top ceramic layer and may be found using the laws of right triangles with Equation 31 (Bittinger, et al. 2001).

$$D_S = \frac{t_C}{\cos(\phi)}$$

Equation 31 Distance that the shock wave travels during dwell.

where t_C is the thickness (m) of the top ceramic layer.

Now, by using Equation 3 and Equation 31, the dwell duration T_D (s) may be calculated using Equation 32.

$$T_D = \frac{D_S}{a}$$

Equation 32 Dwell duration of a ballistic impact.

Table 25 shows the calculated dwell duration along with the energy absorption capability for each of the six biplate combinations.

Table 25 Energy absorption and dwell duration for the various biplate combinations.

	Thickness (mm)		Calculated Values	
Test #	Aluminum	Al_2O_3	Energy Absorption (J)	Dwell Duration (μs)
1	0.00	8.30	920.07	1.2242095
2	1.50	6.80	885.60	1.0029668
3	3.30	5.00	1031.5	0.7374756
4	4.15	4.15	1106.5	0.6121047
5	6.80	1.50	1322.3	0.2212427
6	8.30	0.00	1323.6	0

As shown in Table 25, the relationship of dwell duration and ceramic thickness may be expressed as, the thicker the aluminum-oxide, the longer the dwell duration. This linear relationship is shown in Figure 25.

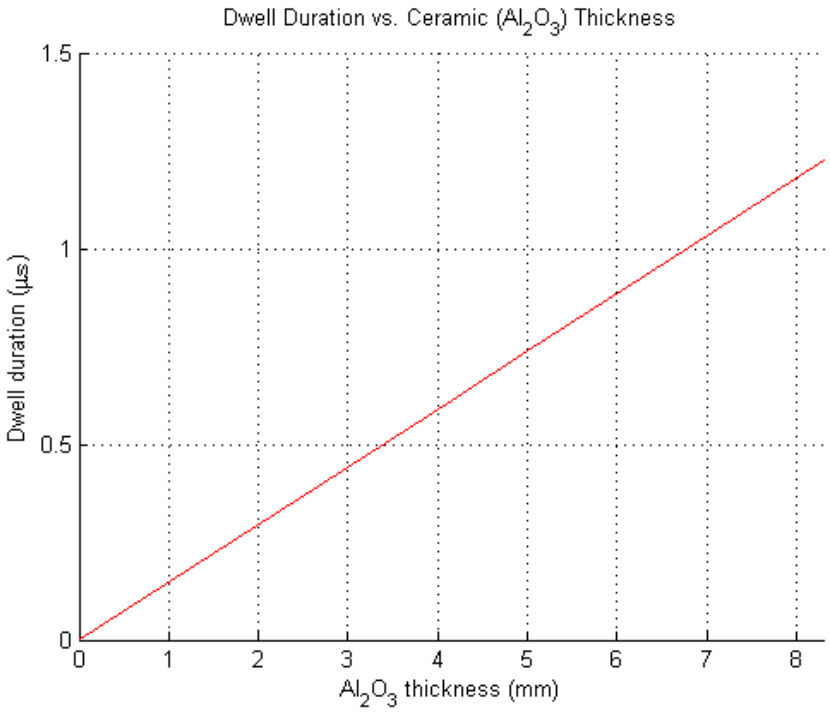

Figure 25 Calculated dwell duration vs. aluminum thickness.

The ideal ballistic plate will degrade the projectile tip as much as possible, thus increasing the contact area(s) and decreasing the various contact pressures (stress). For a relatively ductile projectile, the erosion process is fluid-like and is referred to as

"mushrooming" (Fellows and Barton 1999). Ideally, the mushroomed projectile converts kinetic energy to internal/strain energy in a process of plastic deformation to the shape of a cylinder (or a similar shape). To be effective, this deformation process must also occur prior to the forming of the damage cone, that is, during the dwell duration.

To estimate the amount of deformation of the projectile tip requires several assumptions to be made. For this work, three assumptions are made, and they are:

1) that the projectile tip velocity is zero during the erosion process,
2) the rear of the projectile continues forward at a constant velocity (the impact velocity),
3) and the tip of the projectile maybe simplified and modeled as a triangle.

With these assumptions, and knowing the ballistic plate dwell duration calculated using Equation 32, one may estimate the geometry of the projectile immediately following the end of the dwell duration. It is important to note that because the dwell duration is dependent upon impact velocity and plate thickness, the projectile erosion will also be dependent upon these variables.

Once the damage cone forms, the projectile continues to erode, but the aluminum-oxide aluminum contact area is fixed. This contact area may be increased if the contact area between the projectile tip and the ceramic is increased prior to the end of the dwell duration. Using the law of similar triangles (Bittinger, et al. 2001), and the assumptions mentioned previously, and in the case of the 5.56×45 mm NATO projectile, the eroded tip diameter, d_e (m) is estimated by Equation 33.

$$d_e = \left(T_D V_{in}\right)\left(\frac{d_p}{h_t}\right)$$

Equation 33 Equation for determining the eroded projectile tip diameter.

where h_t is the height of the tip (m) and d_p is the nominal diameter of the projectile (m)

The area of contact, A_C (m^2) between the aluminum-oxide and aluminum layers may now be estimated in terms of the conoid angle, ϕ by Equation 34 as.

$$A_C = \frac{1}{4}\pi\left(d_e + 2\tan(\phi)\, t_c\right)^2$$

Equation 34 Estimation of the aluminum-oxide aluminum contact area given conoid angle.

Combining Equation 30 and Equation 33 with Equation 34, the contact area may be estimated in terms of impact velocity in Equation 35.

$$A_C = \frac{1}{4}\pi\left(\left(T_D V_{in}\right)\left(\frac{d_p}{h_t}\right) + 2\tan\left(\left(\frac{V_{in} - 220}{780}\right)\frac{34\pi}{180} + \frac{34\pi}{180}\right) t_c\right)^2$$

Equation 35 Aluminum-oxide aluminum contact area in terms of impact velocity.

Given a ceramic layer thickness of 5 mm and a 5.56×45 mm NATO projectile travelling at muzzle velocity (Table 1 - 940 m/s), the estimated aluminum-oxide aluminum contact area using Equation 35 is 387.5 mm^2, in contrast to 374.2 mm^2 in the case with no projectile erosion (i.e. $T_D = 0$) using the same thickness of the aluminum-oxide. This is approximately a 4 % difference in contact area, which can be significant.

Table 26 Estimated aluminum-oxide aluminum contact area.

Test #	Thickness (mm)		Contact Area (mm^2)
	Aluminum	Al_2O_3	
1	0	8.30	1067.662
2	1.50	6.80	716.631
3	3.30	5.00	387.452
4	4.15	4.15	266.916
5	6.80	1.50	34.871
6	8.30	0	0

As shown in Table 26, as the thickness of aluminum-oxide decreases, the aluminum-oxide aluminum contact area decreases. A high contact area is desirable, but as the thickness of ceramic increases, the effective protective area of the biplate is decreased. This must be considered toward determining the final geometry.

Another consideration in designing the biplate is to identify any potential plate weak spots. One such weak spot would be when impacted in such a location so that the aluminum-oxide aluminum contact area is not at the maximum. Since the plate is square, an effective or critical width may be determined to help identify this potential weak spot. This dimension relates the thickness of the ceramic layer with the conoid angle, angle of skew, and eroded tip diameter to determine the maximum distance measured from the plate edge that a projectile may impact and the biplate may still have maximum aluminum-oxide aluminum contact. The critical width concept is shown in Figure 26. Note that two damage cones are shown, and these are the extreme cases which still yield a maximum aluminum-oxide aluminum contact area.

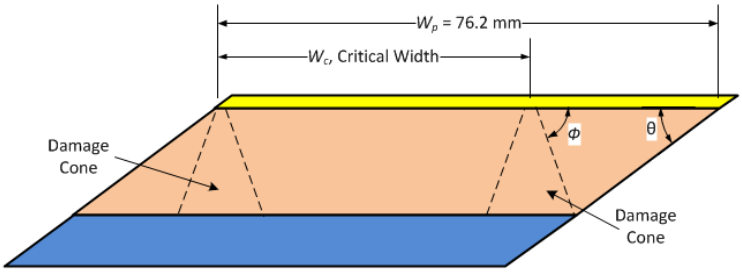

Figure 26 Critical width concept showing two extreme damage cones (Not drawn to scale).

Using the laws of right triangles (Bittinger, et al. 2001), Equation 31, and Equation 33, the critical width, W_c (mm) may be approximated with Equation 36.

$$W_c = W_p - \left[\frac{t_c}{\tan(\phi)} + \frac{t_c}{\tan(\theta)} + \frac{1}{2}(T_D V_{in}) \left(\frac{d_p}{h_t} \right) \right]$$

Equation 36 Critical width equation.

Equation 36 may be combined with Equation 30 to estimate the critical width in terms of impact velocity, V_{in} (m/s) and results in Equation 37.

$$W_c = W_p - \left[t_c \cot\left(\left(\frac{V_{in} - 220}{780} \right) \frac{34\pi}{180} + \frac{34\pi}{180} \right) + t_c \cot(\theta) + \frac{1}{2}(T_D V_{in}) \left(\frac{d_p}{h_t} \right) \right]$$

Equation 37 Critical width equation in terms of impact velocity.

In Table 27, the calculated critical width is tabulated. Because the plate is square and skewed in two directions, the critical width corresponds to two dimensions, therefore the critical protection area may be found. The percent area reduction compares the critical area to that of a 76.2 × 76.2 mm plate, or 5806.44 mm^2.

Table 27 Calculated critical width shown with area reduction.

Test #	Thickness (mm)		Critical Width (mm)	Critical Area Reduction (%)
	Aluminum	Al_2O_3		
1	0	8.30	63.78	29.95
2	1.50	6.80	66.02	24.93
3	3.30	5.00	68.72	18.68
4	4.15	4.15	69.99	15.64
5	6.80	1.50	73.96	5.81
6	8.30	0	76.20	0

Notice from Table 27 that the critical width increases with decreasing thickness in aluminum-oxide. It is important to point out that although the protective area is increasing with decreasing aluminum-oxide, the actual aluminum-oxide aluminum contact area is decreasing. The decreasing aluminum-oxide aluminum contact area increases the chances of an armor perforation.

The biplate design is a classic example of balance and trade-offs between energy absorption, tip erosion, contract, protection areas, minimal weak spots and overall thickness/weight.

6.4 Geometry Selection of the Biplate

As shown in Section 6.3, to select the geometry of the biplate requires the proper balancing of the ability to absorb energy, erode the projectile tip, and to increase layer contact area(s) while maintaining a relatively small thickness and low weight. It has already been determined in Section 4.4 - Design Plan and Concept Proposal that the best arrangement of ballistic plates for mobility and dexterity is that of a two-dimensional matrix. It was also determined that to minimize the gaps between the small ballistic plates, a double-skewed plate geometry will be implemented, as shown in Figure 17. The angle of skew, overall plate thickness and width are fixed at 45°, 8.8 and 76.2 mm, respectively (Section 6.3). Additionally, to keep the plate symmetric, both the length and width are to be the same.

Because the plate is square, the minimum length/width dimension(s) can be determined using the contact area(s) in Table 26, and are tabulated in Table 28.

Table 28 Minimum plate dimension for various plate combinations.

Test #	Thickness (mm)		Contact Area (mm^2)	Minimum Dimension (mm)
	Aluminum	Al_2O_3		
1	0	8.30	1067.662	32.68
2	1.50	6.80	716.631	26.77
3	3.30	5.00	387.452	19.68
4	4.15	4.15	266.916	16.34
5	6.80	1.50	34.871	5.91
6	8.30	0	0	0

Table 28 sets the minimum width dimension by assuming that the projectile impacts directly in the center of the biplate, as the shock wave travels radially and evenly outward from the impact point. These minimum values confirm that in all cases, the set biplate width of 76.2 mm is sufficient to meet the desired aluminum-oxide aluminum contact area.

To decide the individual layer thicknesses requires that the designer balance many variables. These variables include the plate capability to:

1) absorb energy,
2) degrade a projectile tip,
3) increase aluminum-oxide aluminum contact area, and
4) increase critical protection area.

These variables must also be balanced with a low areal density to meet the goals set forth in Table 8 Design goals and subgoals of the hybrid armor system. To aid in the decision process, a scoring matrix is used in a similar method that was shown in Section 5.4, to include a multiplication factor (MF), normalized value (NV), and score value (SV).

Table 29 shows the summarized trait values, while Table 30 shows the tabulated score values for each of the layer combinations.

Table 29 Layer combinations listed with trait values.

	Layer Combination (Al_2O_3/Al)			
Trait	6.8/1.5	5.0/3.3	4.15/4.15	1.5/6.8
Areal density, AD (kg/m^2)	31.143	29.07	28.10	25.05
Energy absorption, EA (kJ)	885.60	1031.5	1106.5	1322.3
Dwell time, DT (μS)	1.003	0.738	0.612	0.221
Layer contact area, LCA (mm^2)	716.63	387.45	266.92	34.87
Critical width, CW (mm)	66.02	68.72	69.99	73.96

Table 30 Scoring table for various biplate layer thicknesses.

			Layer Combination (Al_2O_3/Al)							
			6.8/1.5		5.0/3.3		4.15/4.15		1.5/6.8	
Trait		MF	NV	SV	NV	SV	NV	SV	NV	SV
A	AD	5	1	5	0.933	4.667	0.902	4.511	0.804	4.022
Total: A		5	--	5	--	4.667	--	4.511	--	4.022
B	EA	4	0.670	3.349	0.780	3.900	0.837	4.184	1	5
	DT	2	1	2	0.736	1.472	0.610	1.220	0.220	0.441
	LCA	3	1	3	0.541	1.622	0.372	1.117	0.049	0.146
	CW	5	0.893	4.463	0.929	4.646	0.946	4.732	1	5
Total: B		14	--	12.812	--	11.640	--	11.253	--	10.587
B - A		9	--	7.812	--	6.973	--	6.742	--	6.564

In Table 29, the areal density is calculated using Equation 2 with density values from Table 10 and Table 11. In Table 30, the normalized values were calculated using Equation 7.

Because of the scoring determined from Table 30, the ultimate decision for determining the layer thicknesses was between two arrangements. Both the 6.8/1.5 and 5.0/3.3 aluminum-oxide to aluminum thickness ratio biplates were considered. The final decision was to use the 5.0/3.3 type biplate, although it was the second highest scoring armor plate. This decision was made for two reasons, the first being related to the low weight subgoal set in Section 4.4. The chosen biplate (5.0/3.3) is about 7 % lighter than the 6.8/1.5 plate. The second reason is on the bases that the plate must absorb energy of a NIJ projectile. Therefore, as a design parameter the plate should be able to absorb at least half the energy of a 7.62 mm Soviet projectile, or about 1003 J (Table 1) before being perforated.

The final dimensions of the biplate are shown in Figure 27 and Figure 28.

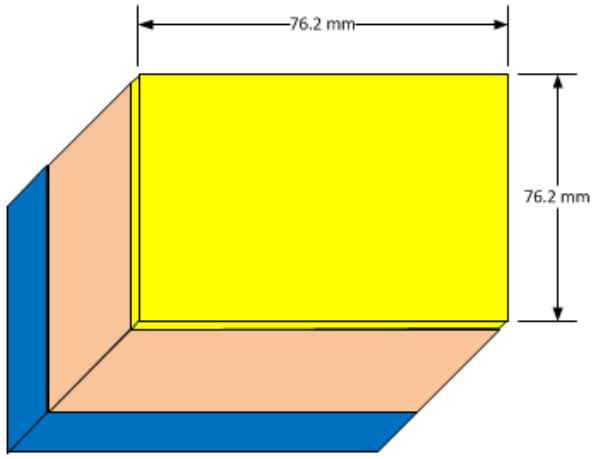

Figure 27 Final biplate dimensions - Top view (not drawn to scale).

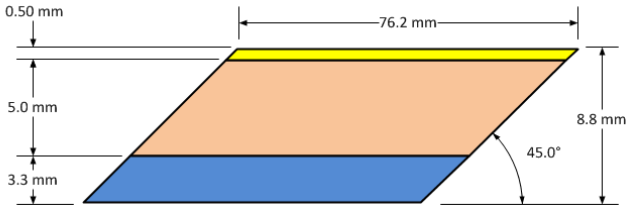

Figure 28 Final biplate dimensions - Side view (not drawn to scale).

Recall that in Table 27 the critical width for the 5.0/3.3 plate combination is 68.72 mm. This dimension is shown in Figure 29 along with the top area of highest risk if impacted, and for this work is termed as the "danger zone". This area is bounded by the extremes of the two critical width dimensions and the plate edges. The danger zone is the area that if impacted would provide the least aluminum-oxide aluminum contact area and is noted for the analysis.

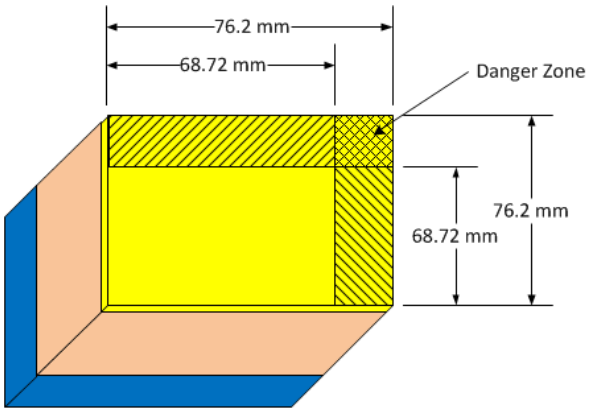

Figure 29 Top view of biplate with the critical dimension and the danger zone (not drawn to scale).

The layout of the biplates as worn on a person, is shown in Figure 30. It shows fourteen biplates positioned around a model of a cross-sectional torso. The biplates are drawn to scale using the plate dimensions in Figure 27 and Figure 28. The torso is modeled as an ellipse where the major and minor axes are the measured dimensions of the author's torso (17" and 9").

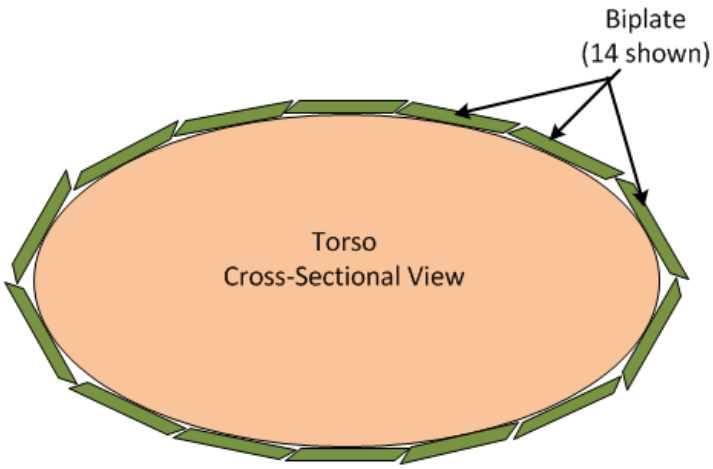

Figure 30 Scaled layout of biplates on simulated torso section.

In Figure 30, each plate is rotated approximately 5° relative to the previous to allow for the curvature about the torso section. The exception to this angle is the two

plates positioned at either outer end of the torso. These two plates are rotated about 15° to allow for curved coverage about this particular section. See Figure 67 in Appendix E to view other plates considered to avoid the tight curved sections.

CHAPTER 7 SYSTEM ANALYSIS

7.1 Analysis Techniques

The ultimate goal of this work is to design a flexible NIJ level III armor and to determine if the proposed design is feasible. To save time, money and other resources, finite element analysis (FEA) is used to simulate and predict the response of an NIJ P-BFS test on the purposed body armor system in lieu of experimental testing. As in Section 6.1, ANSYS Workbench 12.1 Explicit Dynamics (SAS IP, Inc. 2009) with the AUTODYN solver is used for the FEA in this section. Mainly, a 64-bit Windows 7 operating system CPU with Intel® dual core processors at 3.00 GHz and 8 GB of RAM is used for the finite element analysis.

Several combinations of projectile impact velocity, angle, and location were analyzed on a 3×3 biplate layout with underlying armor comprised of sixteen layers of plain-woven Kevlar® 29 fibers, as shown in Figure 31. Following the NIJ standards guidelines (U.S. Department of Justice 2008), modeling clay is used to record the backface signature (BFS). To save computational time and because licensing resources, the 3×3 biplate arrangement is used, and only the armor components of the layout are analyzed (that is, the armor carrier and cover shown in Chapter 4 are omitted from the FEA). The layout of the biplates is such that the spacing is 3 mm between each plate. Additionally, to save nodes, the biplate(s) that were not directly impacted by the

projectile were modeled with a rigid physical behavior, and a smaller than actual clay segment is used, measuring 50×250×250 mm (*H*×*W*×*L*).

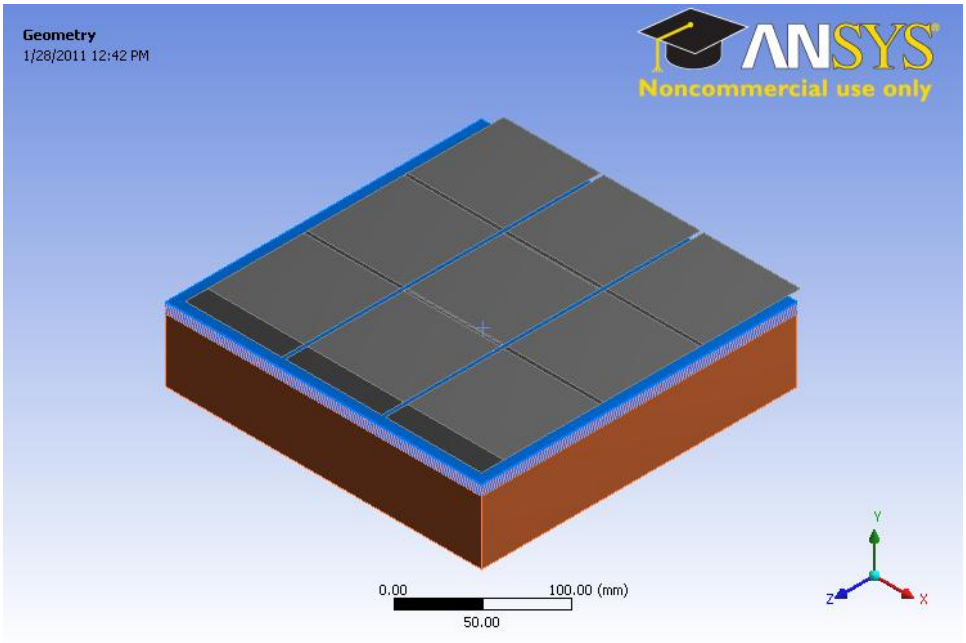

Figure 31 Armor layout used for the finite element model.

7.2 Simulation Setup

For the finite element analysis to realistically predict the outcome of a P-BFS test, numerous simulations must be completed. The location of the impact, angle of incidence, and impact velocity must all be adjusted. Weak points in the armor system must be identified, tested and compared to a hit in an ideal location to determine if the armor has failed the P-BFS test. Figure 32 shows the four impact points considered for the FEA.

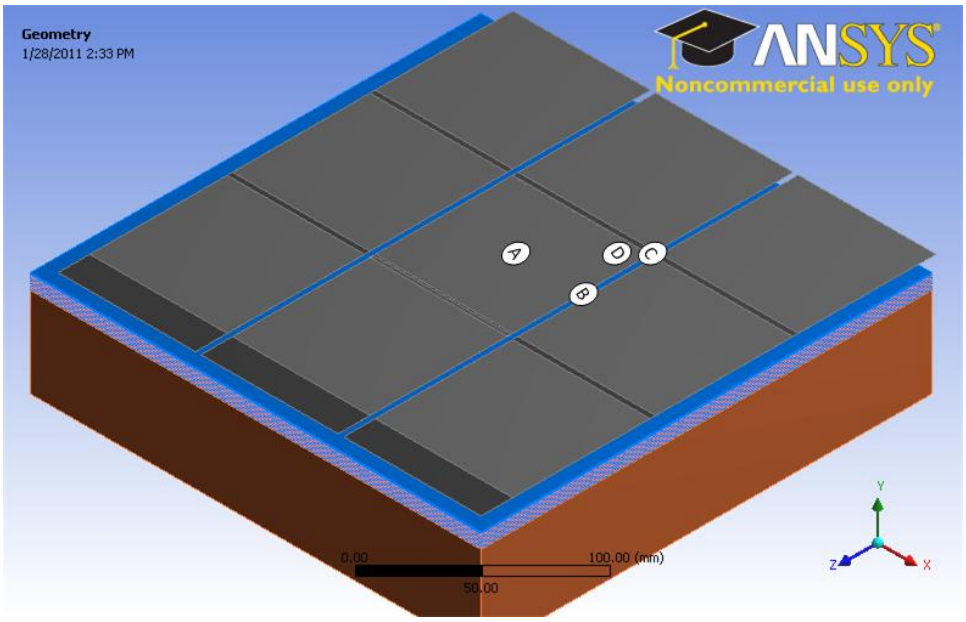

Figure 32 Impact points considered for the FEA.

As illustrated in Figure 32, there are four impact points considered for the finite element analysis (A,B,C,D). Point A is the ideal point of impact, which is dead center in the biplate. Points B, C, and D each correspond to a logically or analytically driven weak point in the armor system. Point B is located at the center of the gap spacing between two biplates, Point C is the center of the corner connection between four biplates, and finally Point D is the center of the danger zone shown in Figure 29. Table 31 shows the impact location with the angle of impact (incidence) and amount of tests at the respective location.

Table 31 Impact location shown with angle of impact.

Point	0°	45°	Total Tests
A	4	4	8
B	4	4	8
C	4	0	4
D	4	0	4

In regards to Point B, the impact(s) at the 45° angle of incidence is referenced toward the angle of skew, thus parallel with the biplate skew angle. Each point is impacted one time per simulation, starting with the lowest and ending with the highest of the four set impact velocities.

7.3 Analysis Impact Velocities

For each impact point, the projectile initial velocity is adjusted. This is done to simulate an impact from the various projectiles in the NIJ level I, IIA, IIIA, and III categories. As mentioned in Section 5.2 Projectile Parameters, the only projectile geometry tested is the 5.56×45 mm NATO, and the impact velocity is adjusted to match the kinetic muzzle energy of a projectile(s) in the various NIJ categories. This serves two purposes; first the 5.56 NATO is a great armor piercing projectile, much better suited for penetrating armor than any other lesser projectile, and therefore a good indicator of if the armor will pass the respective NIJ test. The second purpose is to identify the safe linear range from the muzzle of the 5.56 NATO rifle that the armor system would theoretically protect the wearer. This range can be determined from tables generated by the U.S. Department of Defense that tabulate the velocity of the 5.56 NATO and measured distance (U.S. Department of Defense 1997).

Table 32 Simulation impact velocities used for the FEA.

Velocity (m/s)	NIJ Level	Kinetic energy (J)	Equivalent range (m)
282.8	I	160.0	> 500
527.49	IIA	556.5	408
860.81	IIIA	1482	85
940.0	III	1711	0

Note that in Table 32, the equivalent range of the NIJ level I armor is in excess of 500 meters. This is because at this low velocity the, Department of Defense tables do not have any recorded data. The equivalent ranges for the IIA and IIIA levels were determined by linear interpolation between the data points in the Department of Defense tables.

7.4 Modeling Clay Properties and Boundary Conditions

The modeling clay used to measure the BFS is specified by NIJ standards to be a non-hardening oil based clay (U.S. Department of Justice 2008). The material properties of the oil based clay, to include the engineering constants, are difficult to obtain. This is partly because of the difficultly in conducting experiments on a highly ductile material, and partly because the properties are dependent upon many variables such as temperature (even slight variation in room temperature), prior large-strain history, and applied strain rate (Crandall, Kursweil and Kigam 1971); although, research does show that the modeling clay may be considered to be linear viscoelastic (Crandall, Kursweil and Kigam 1971). For the purposes of this work, the clay is considered to be room temperature at 20°C, and therefore the Young's modulus may be taken to be 34.474 MPa (Crandall, et al. 1970). To determine the shear and bulk moduli, the Poisson's ratio must be experimentally determined. For this work, the average dynamic Poisson's ratio is taken to be 0.434 (Crandall, Kursweil and Kigam 1971). The shear modulus, G (MPa) may be found by Equation 38.

$$G = \frac{E}{2(1+v)}$$

Equation 38 Shear modulus of a linear isotropic material.

With the calculated shear modulus, the bulk modulus, *K* may be determined using Equation 4. The density of the clay as well as other material properties is listed in Table 33 (Crandall, Kursweil and Kigam 1971).

Table 33 Dynamic material properties used for the modeling clay.

Density (kg/m^3)	1300
Young's modulus (MPa)	34.474
Shear modulus (MPa)	12.02
Bulk Modulus (MPa)	87.055
Poisson's Ratio	0.434

The boundary conditions for the finite element model are setup to simulate the effects of the NIJ P-BFS test. The model includes the ballistic plates, Kevlar® layers and the clay backing. The ballistic plates are made of Kevlar, aluminum-oxide, and aluminum, which are perfectly bonded to each other. In turn, the bottom of the ballistic plate is also perfectly bonded to the top layer of the multi-layered Kevlar® textile. The layers of the Kevlar®, however, are in frictionless contact with each other. The clay is simply supported on the bottom while using rollers on the vertical edges. These boundary conditions are assumed to simulate the rigid frame in where the clay is placed.

All of the nodes on the rear face of the clay have a fixed support boundary condition applied to them, thus all degrees of freedom are restricted. This is to simulate the rear removable rigid segment of the NIJ specified test rig. Figure 33 shows the schematic of the constraints used on the clay segment used for the FEA.

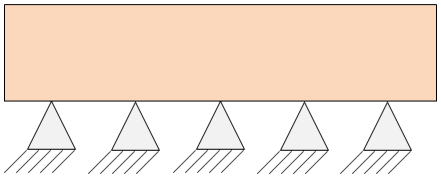

Figure 33 Lower, rear face constraints used for the FEA (Side view of clay).

The nodes on all four of the side faces of the clay segment are supported only in the normal direction. Therefore, the sides may not bend or move outward in the perpendicular direction, but may move in either side-to-side or tangent direction(s). This is done to simulate the rigid side supports of the test rig, as per the NIJ standards (U.S. Department of Justice 2008). Figure 34 shows schematic of the clay side boundary conditions used for the finite element analysis.

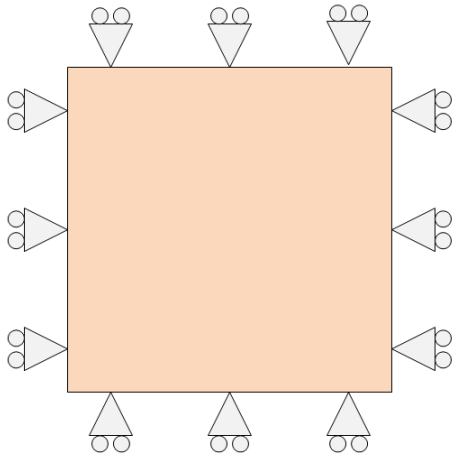

Figure 34 Side constraints used for the FEA (Top view of clay).

7.5 Body Contact Interactions

To simulate a realistic response, the contact interactions between each corresponding armor component must be carefully examined. For this work, only frictionless and bonded contact types are considered. Friction is not considered for two reasons:

1) because of required increased computational time, and
2) to be able to evaluate the armor on a "worst case scenario".

Although in reality friction will inevitable contribute to the armor energy absorption ability, the friction coefficient(s) will change based on uncontrollable external factors,

such as manufacturing techniques and the tangential and normal loading caused by the armor carrier being worn and/or covered by equipment, clothing and so on.

The sixteen woven Kevlar® armor layers are each modeled with frictionless interactions between corresponding layers, and to the clay. For the three biplate components (top Kevlar layer, aluminum-oxide, aluminum), bonded contacts are used to permanently join each layer together. The nine biplates are then each bonded to a single layer 0.5 mm thick layer of Kevlar which has a frictionless interaction with underlying plain-woven Kevlar® layers. This is done to simulate both the separation of the two main armor components, where each is stored in a separated compartment in the armor carrier, and also to simulate the elastic bands holding the biplates together as a system.

7.6 Point A Analysis – Zero Angle of Incidence

Point A of Figure 32 is considered first for the FEA. As discussed in Section 7.3, four impact velocities are used to determine the BFS in the modeling clay. The velocity of the projectile was recorded over the entire impact time to determine if the projectile penetrated the armor system. To predict the backface signature, the maximum vertical deflection was recorded during the entire impact.

Figure 35 shows the system layout for the finite element analysis of Point A.

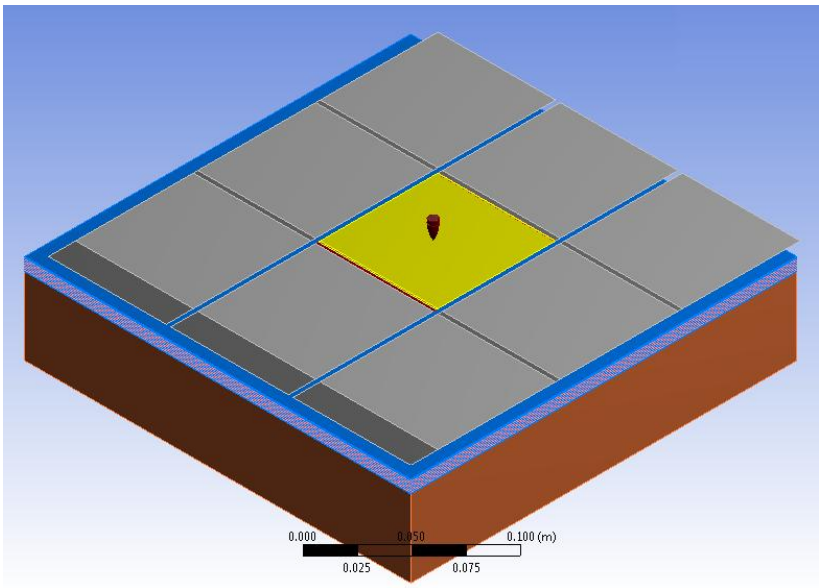

Figure 35 Finite element analysis body layout for Point A analysis.

The element mesh used for the analysis is shown in Figure 36. Notice that the clay is meshed using a sweep technique (SAS IP, Inc. 2007), which to reduce nodes gradually increases the element size from the source to the target.

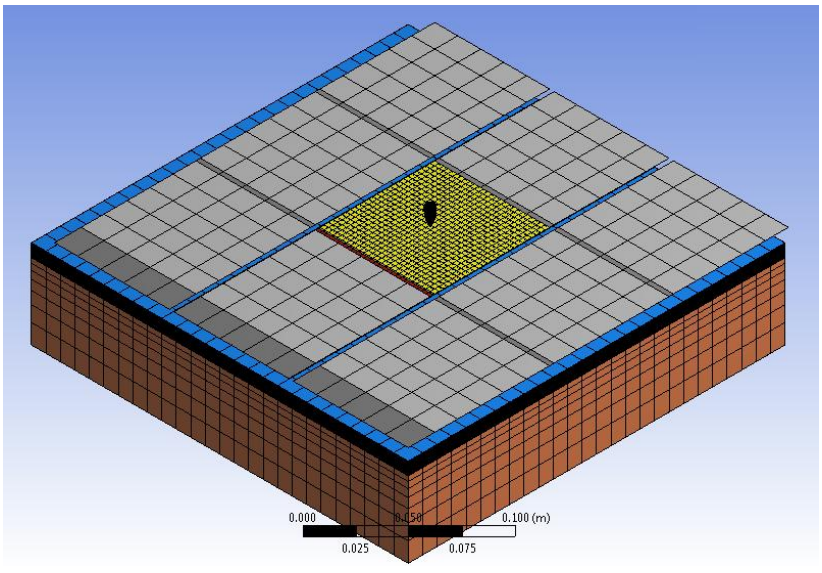

Figure 36 Element mesh used for Point A analysis.

To mesh the geometry, hexagonal (hex8) and tetrahedral (tet4) (SAS IP, Inc. 2007) elements are used. Some the mesh statistics are shown in Table 34.

Table 34 Mesh statistics for Point A analysis.

Nodes	44649
Elements	49095
Average aspect ratio	5.951
Average Jacobian ratio	1.000
Relevance center	Medium
Relevance	-8

The average aspect ratio is shown to quantify the quality of the mesh. The lower the aspect ratio (cannot be lower than one), typically the better and more accurate the response (Logan 2007). In this case, the aspect ratio is fair, showing some room for improvement. The Jacobian ratio is recorded to show consistency between each separate mesh setup.

Figure 37 shows six frames taken from the resulting video created by the Point A equivalent stress analysis.

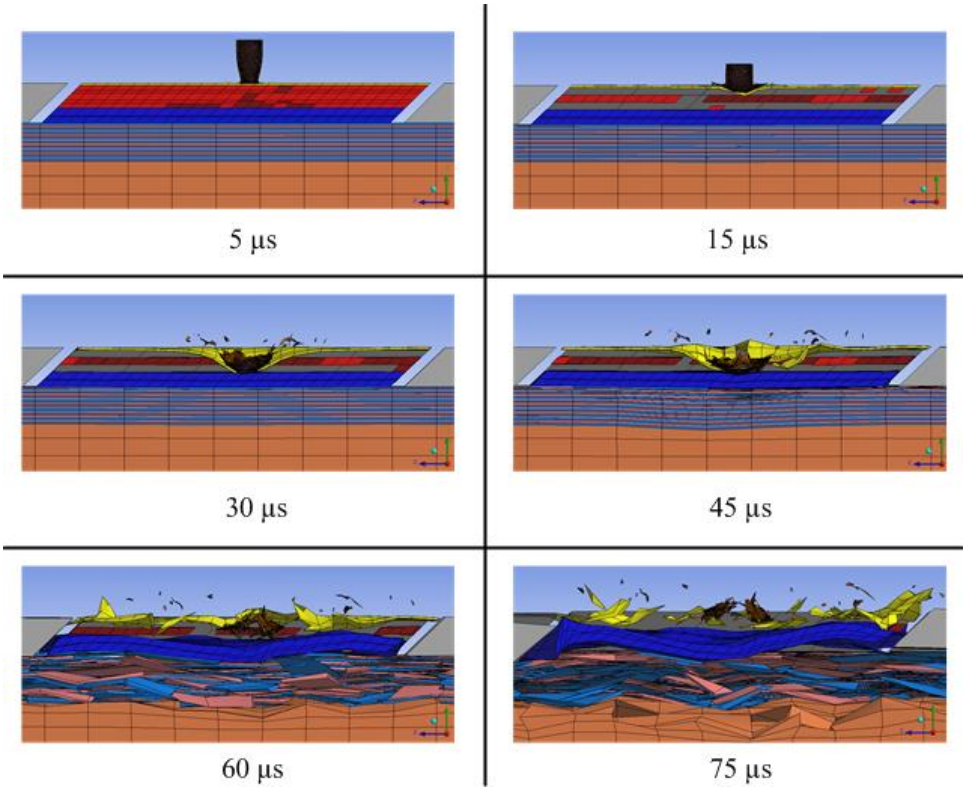

Figure 37 Six frames of the Point A direct impact (NIJ IIA simulation shown).

One can see the damage cone forming in the first frame, 5 μs, which is momentarily after the dwell duration (calculated as 0.77 μs). Notice that the projectile is degrading within the first moments of impact, sending fragments outward from the impact point. This erosion is by design of the ceramic layer as part of the biplate. One can also see the Kevlar® under layers being first deflected then later torn apart; this is expected given the normal modes of textile failure discussed in Section 5.7.

The results of the BFS and if the aluminum of the biplate and/or the entire system is penetrated for the analysis is tabulated in Table 35.

Table 35 Simulation results for the Point A direct impact.

	I	IIA	IIIA	III
Maximum deflection, BFS (mm)	0.67	10.94	35.5	> 55
Penetration detected (Yes, No)	No	No	No	No
Aluminum perforated (Yes, No)	No	No	Yes	Yes

As expected, the BFS increased with increasing impact velocity. The armor system was also able to protect the wearer from a penetrating projectile when impacted at the specified center location. The aluminum was penetrated in both the NIJ IIIA and NIJ III simulations, yet the armor system was not completely penetrated in any simulation. This test predicts that the armor system would fail the BFS (on account of the excessive NIJ III BFS) test and yet pass the perforation test. There is room for improvement, and recommendations are given in Section 9.2.

The recorded projectile velocities for each test are shown in Figure 38.

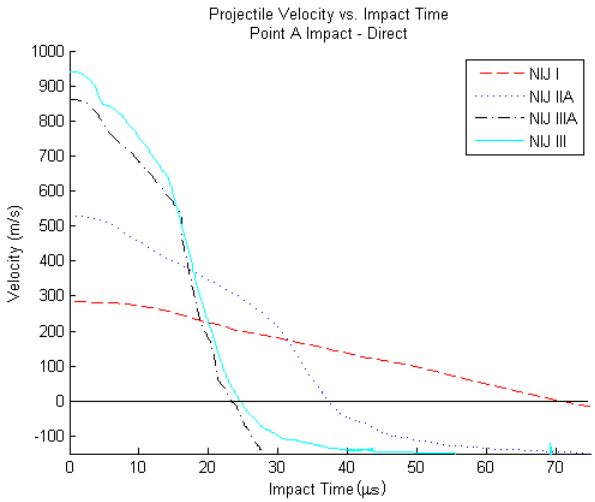

Figure 38 recorded average velocities for the Point A direct impact.

What is interesting to note from Figure 38 is that the NIJ I and IIA simulations predict the projectile velocity to decrease gradually during the impact, whereas the IIIA and III tests have the projectile velocity decreasing rapidly upon impact. As seen in Figure 38, the projectile velocity profiles of both the NIJ IIIA and III tests are virtually identical during the impact, and both tests predict that the aluminum is penetrated.

7.7 Point A Analysis – 45 Degree Angle of Incidence

With the direct impact analysis on Point A complete, the angle of incidence was adjusted to 45° and the analysis was redone. The oblique impact is important to consider because as the angle of incidence changes, the components of velocity change, and thus the mechanisms of energy absorption and projectile degradation are different as compared to a direct impact. Figure 39 shows the layout of the bodies analyzed for the oblique impact at Point A, or the center biplate. All analysis settings and impact velocities are kept constant from the previous direct Point A analysis.

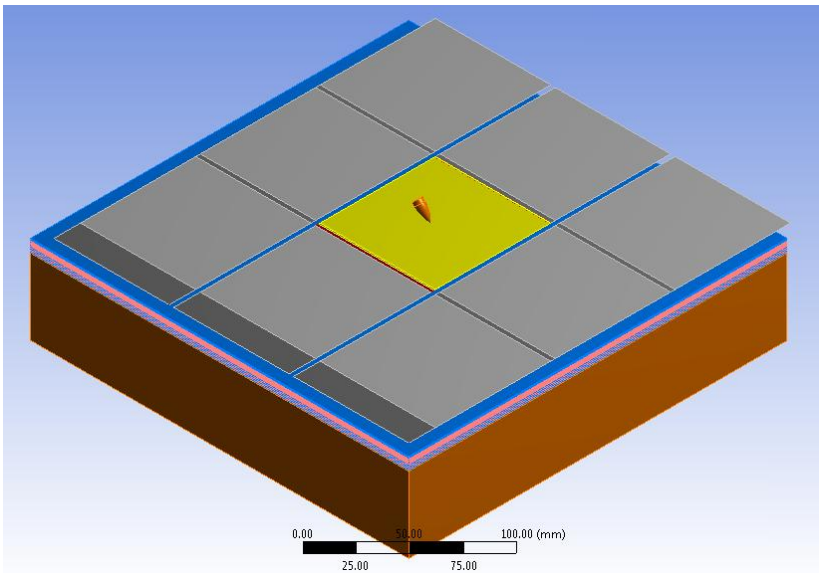

Figure 39 Body layout used for the Point A oblique impact analysis.

The techniques used to generate the element mesh in this analysis were the same as used in Section 7.5, and the mesh is shown in Figure 40.

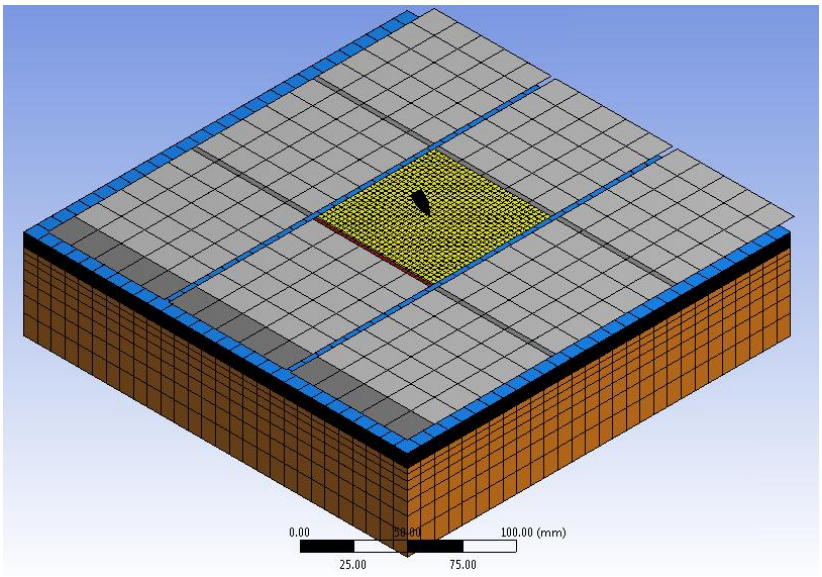

Figure 40 Element mesh used for the oblique center impact.

Table 36 shows some of the statistics of the element mesh used in the oblique center biplate analysis.

Table 36 Statistics of the oblique center impact mesh.

Nodes	48393
Elements	40235
Average aspect ratio	7.162
Average Jacobian ratio	1.000
Relevance center	Medium
Relevance	0

The aspect ratio is slightly higher than the previous analysis, mainly because of the changed relevance value. However, the Jacobian ratio is the same, and therefore the models are comparable.

Figure 41 shows six of the frames captured from the NIJ IIA simulation video of the Point A oblique impact.

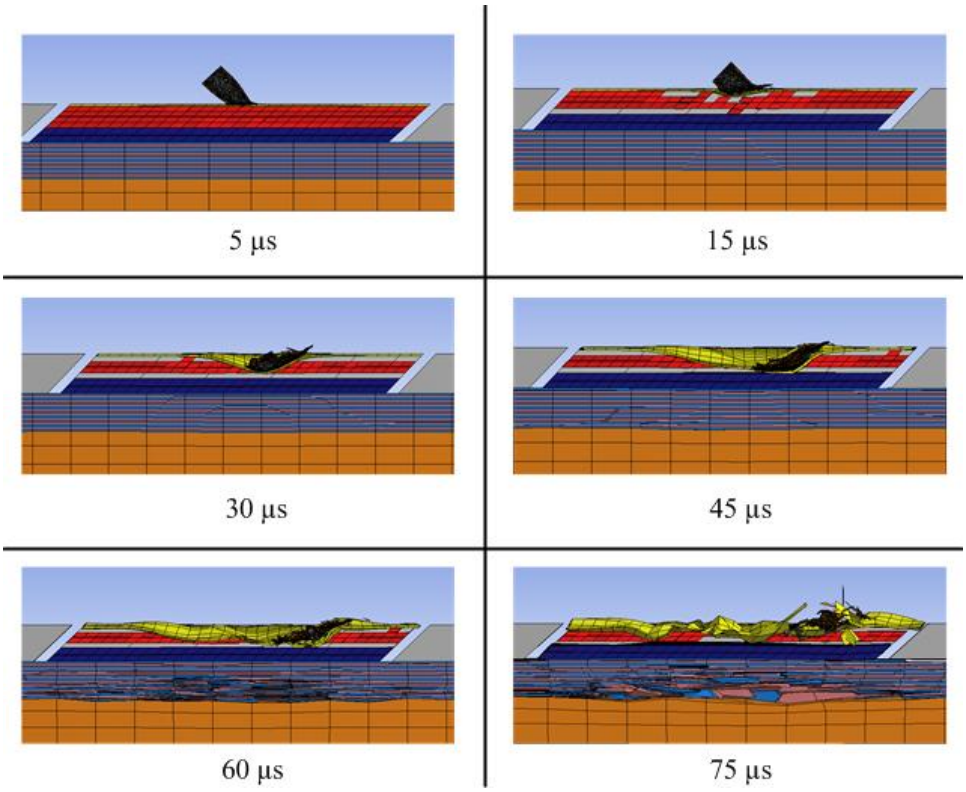

Figure 41 Six frames of the analysis of the oblique Point A impact.

From Figure 41, notice the sliding of the projectile in the tangent direction. This behavior is expected for an oblique impact and is one of the reasons why considering an oblique impact is so important in the analysis. Normally, to reduce variables, only direct impacts are considered (Tabiei and Nilakantan 2008). As one can tell, this response is much different then the direct Point A analysis. If frictional interactions were considered in this work, a large amount of energy would theoretically be absorbed via that mechanism. The modes of failure of the textile, aluminum-oxide, and aluminum are the same as in the direct Point A analysis, as expected.

The P-BFS results are tabulated for the oblique Point A impact in Table 37.

Table 37 Simulation results for the Point A oblique impact.

	I	IIA	IIIA	III
Maximum deflection, BFS (mm)	0.42	5.05	> 55	36.8
Penetration detected (Yes, No)	No	No	Yes	No
Aluminum perforated (Yes, No)	No	No	Yes	No

Note that in Table 37 the BFS of the NIJ III test is less than 44 mm, yet the IIIA test predicts a BFS in excess of 55 mm. This data is nearly reverse that of what is shown in the NIJ IIIA and III simulations in Table 35 for the Point A direct impact analysis. This data goes on to show that at this impact point, the wearer is protected against a penetrating projectile (in the armor and the biplate) for all but the NIJ IIIA impact velocities. This failure at a lower NIJ level could be related to either the damage cone geometry created, or to the critical velocity value, which is mentioned in Section 9.2.

The recorded average mass velocity of the projectile in the normal direction (to the biplate top face) is shown in Figure 42.

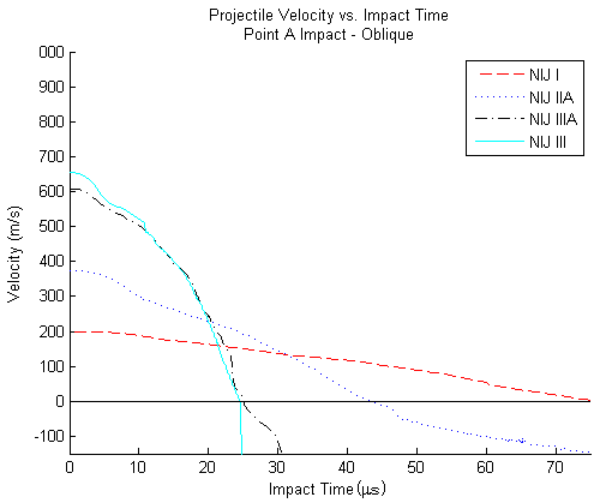

Figure 42 Average projectile mass velocity in the normal direction.

As in the previous Point A analysis, the projectile velocity rapidly decreases upon impact for the NIJ IIIA and III simulations and more gradually for the I and IIA tests. Again, the average projectile velocity profile is nearly identical for both the NIJ IIIA and III tests.

7.8 Point B Analysis – Zero Angle of Incidence

One of the potential, and obvious, weak points of the proposed body armor system is at the spacing (gaps) between the biplates. This area of interest is the next to be analyzed. The analysis settings and clay/armor component geometry is held constant from the previous two impact tests. The geometry layout considered for this simulation is shown in Figure 43.

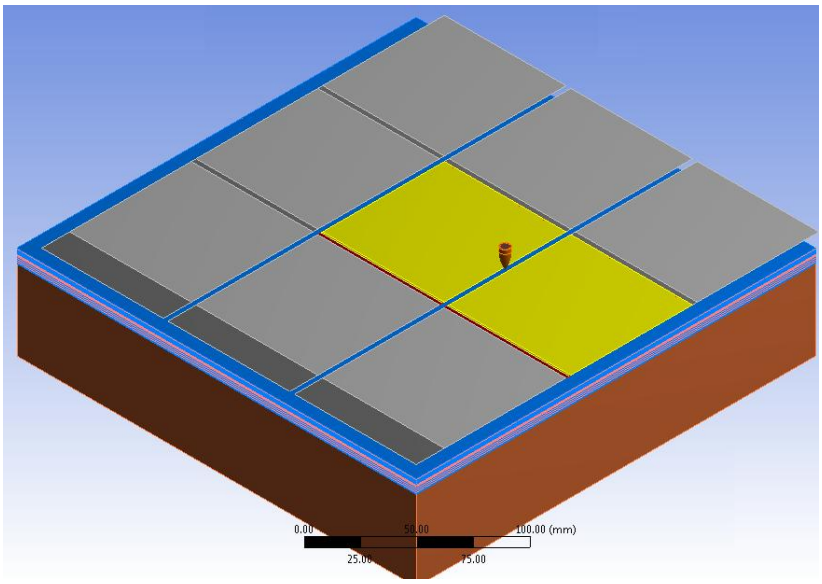

Figure 43 Geometry considered for direct Point B impact.

The same element mesh techniques are used for the finite element analysis in this section as in the previous two impact tests. The element mesh is shown in Figure 44 and some of the mesh statistics are shown in Table 38.

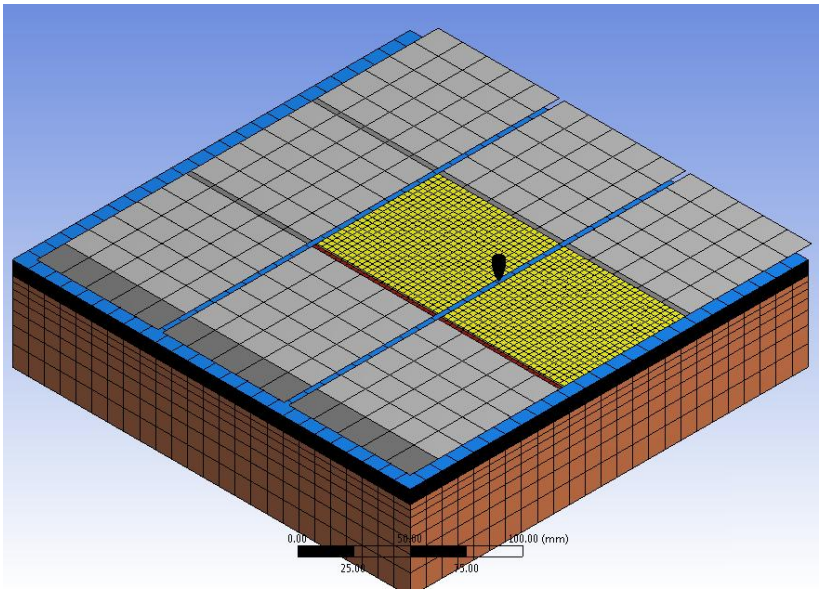

Figure 44 Element mesh used for the direct Point B analysis.

The overall element size used to mesh the biplates increased as compared to the Point A simulation. However the clay, projectile and Kevlar® layers were modeled with nearly identical element sizes.

Table 38 Mesh statistics for direct Point B analysis.

Nodes	45715
Elements	49838
Average aspect ratio	5.813
Average Jacobian ratio	1.000
Relevance Center	Medium
Relevance	-13

The average aspect ratio shows room for improvement, and the Jacobian ratio is held constant from the Point A tests, and therefore the models may be compared.

In this case, two plates will theoretically be working together to absorb energy, destroy the projectile, and distribute dynamic loads. Figure 46 shows six cross-sectional views of captured video clips from the NIJ IIA analysis.

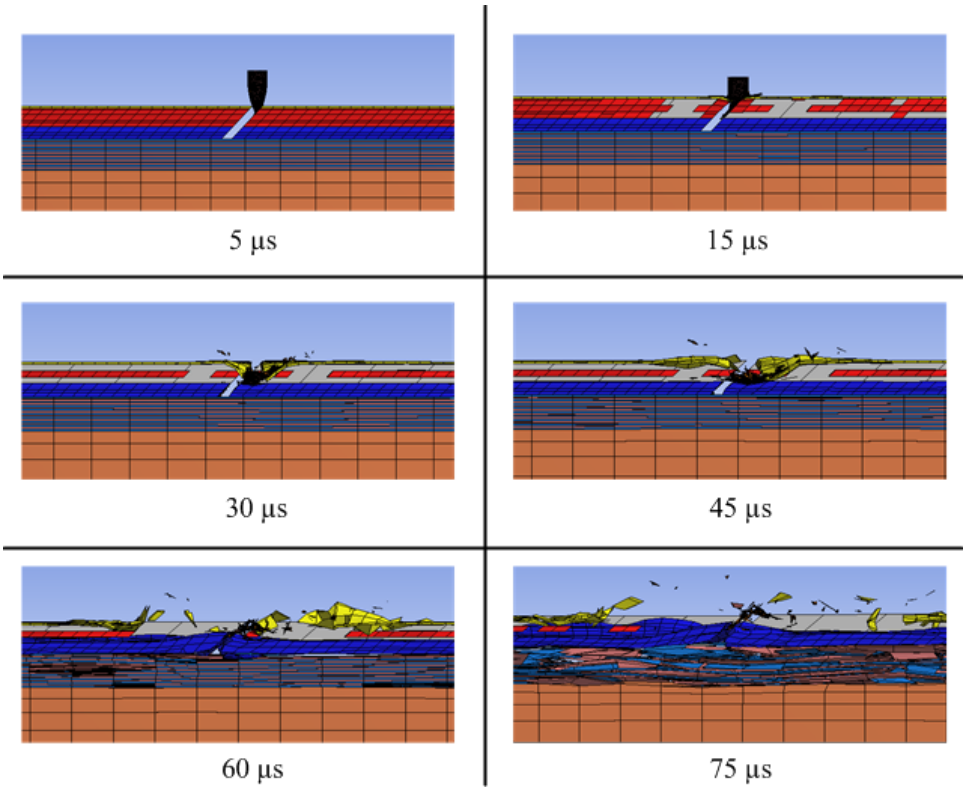

Figure 45 Six frames of the analysis of the direct Point B impact.

Notice in Figure 45 that the projectile impacts the exposed ceramic skewed face (right plate) and then reflects off this face to partially impact the left biplate. This effect contributes highly to the energy distribution in the system and in particle between the two impacted biplates. The projectile is deformed within the first few moments of impact, sending fragments outward from the impact point.

The predictions of the P-BFS test for this impact point combination are shown Table 39.

Table 39 Simulation results for the Point B direct impact.

	I	IIA	IIIA	III
Maximum deflection, BFS (mm)	0.89	10.85	47.6	> 55
Penetration detected (Yes, No)	No	No	No	Yes
Aluminum perforated (Yes, No)	No	No	Yes	Yes

One can see that both the NIJ IIIA and III tests predict that the BFS test would be a failure. However, the armor is able to protect against all threat levels except the NIJ III level, where at this level the armor system was indeed partially penetrated. In the case where the armor or aluminum was penetrated, only a small amount of the projectile was able to proceed beyond the component, as the remainder of the projectile was destroyed.

The recorded projectile average mass velocity for all four simulations is shown in Figure 46.

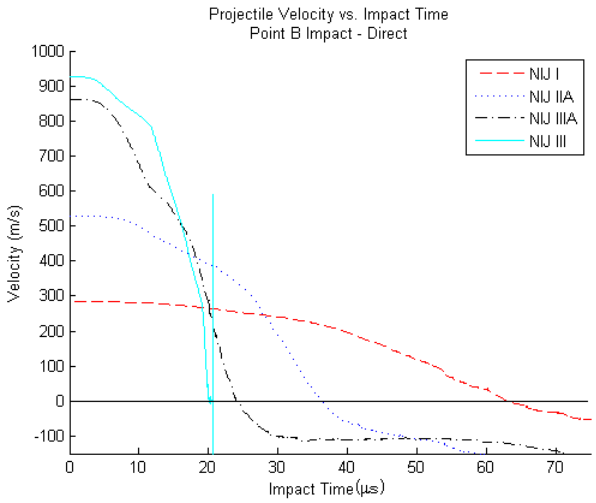

Figure 46 Recorded mass velocity during the direct Point B impact.

As in both of the Point A tests, the same trend with the NIJ IIIA and III velocity profile hold true, however the NIJ I velocity profile is less gradual then either of the two Point A tests. Also, the NIJ III profile has a large spike around 20 μs as this is caused by the projectile being nearly totally destroyed and particles are travelling away from and through the armor system itself.

The results in this section preliminarily show that this impact combination is in fact an armor weak-spot that must be addressed.

7.9 Point B Analysis – 45 Degree Angle of Incidence

With the results tabulated for the direct impact at Point B, the angle of incidence was set at 45°. As mentioned, Point B is a preliminarily established weak spot, and a separate analysis must be considered for a projectile travelling directly into the gap between the two biplates, or in-other-words at the angle of skew. The geometry considered for the FEA in this section is shown in Figure 47. All analysis settings and geometric dimensioning is held the same as the last simulation. Other analysis settings are provided in Table 53.

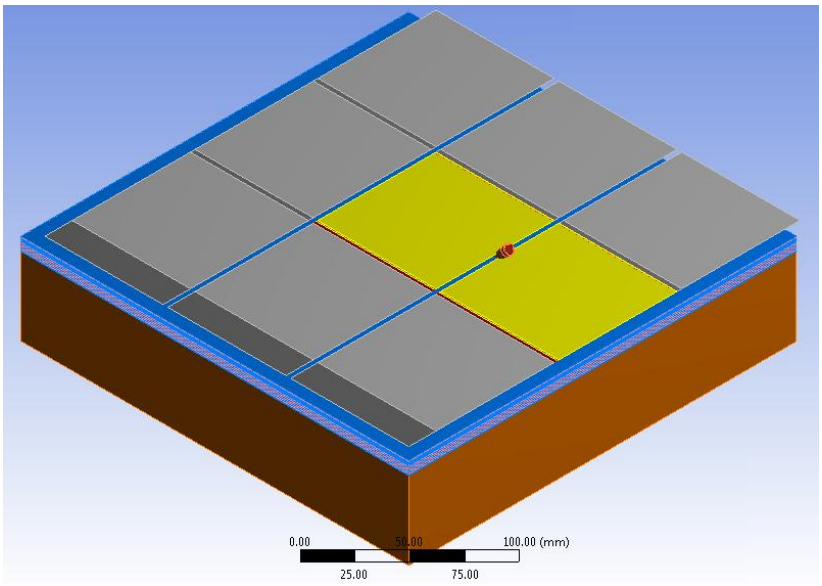

Figure 47 Body layout used for the Point B oblique impact analysis.

The mesh of the model is shown in Figure 48, and some mesh statistics are given in Table 40. As shown, the geometry and mesh is similar to the previous Point B direct analysis completed previously.

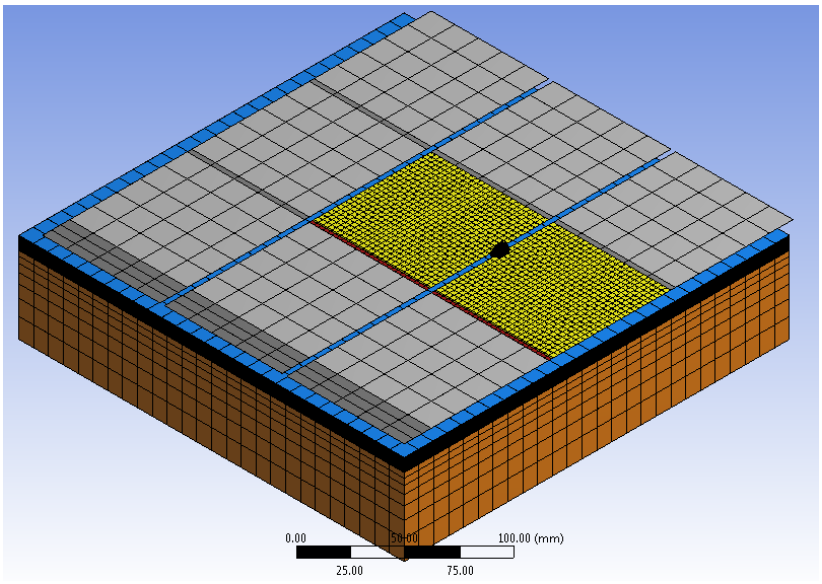

Figure 48 Element mesh used for the oblique Point B analysis.

Table 40 Mesh statistics for Point B oblique impact.

Nodes	50563
Elements	41110
Average aspect ratio	6.933
Average Jacobian ration	1.000
Relevance Center	Medium
Relevance	-7

In Figure 49, one can see six frames captured from the video clip of the equivalent stress analysis for this combination.

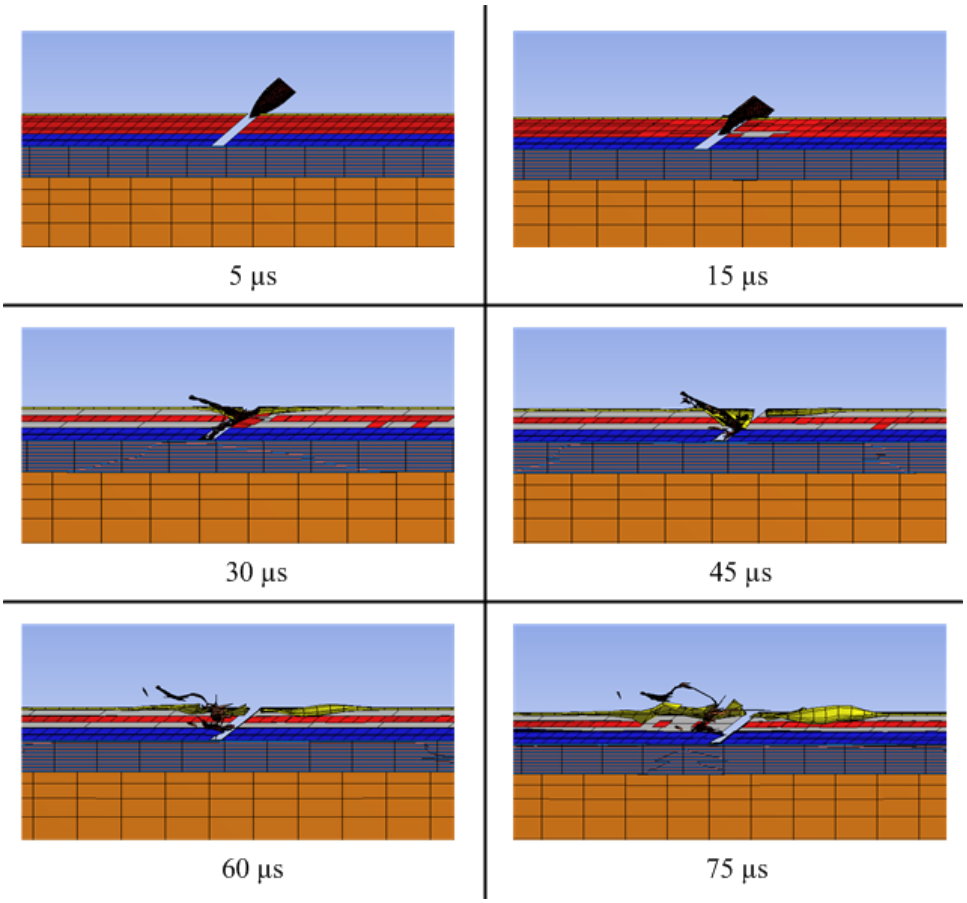

Figure 49 Six frames of the analysis of the oblique Point B impact.

Notice that the projectile is cut, or literally split between the two biplates impacted. This is caused by the hardness and sharp edges of the ceramic and aluminum plates acting in a knife like fashion to cut the projectile. This outcome was predicted by the design and spacing of the plates, where the spacing is uniformly set at 3 mm, or roughly half the nominal diameter of the 5.56 NATO projectile. This splitting proved to be an effective means of distributing the dynamic loads between the two biplates, in fact more effective than anticipated.

The predictions for the NIJ P-BFS test for the Point B oblique impact are shown in Table 41.

Table 41 Simulation results for the Point B oblique impact.

	I	IIA	IIIA	III
Maximum deflection, BFS (mm)	0.14	1.03	7.30	3.49
Penetration detected (Yes, No)	No	No	No	No
Aluminum penetrated (Yes, No)	No	No	No	No

The results of the P-BFS test show that Point B under an oblique impact is not in fact a weak spot. Interestingly, the NIJ IIIA test results in a higher BFS than the NIJ III test, much like the Point A oblique impact. Again, this could be related to either the critical velocity of the conoid angle (aluminum-oxide aluminum contact area).

The average mass normal velocity is shown in Figure 50.

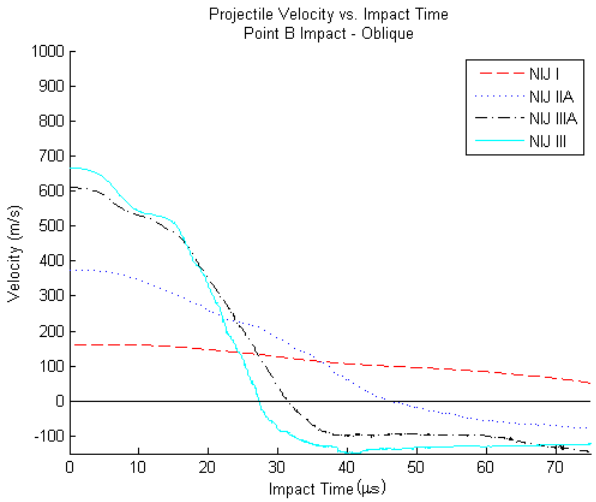

Figure 50 Average mass normal velocity recorded during Point B oblique impact.

As expected from viewing of all the previous results, the velocity profile decreases rapidly for the NIJ IIIA and III simulations, and not nearly as rapidly for the I and IIA tests.

Upon viewing the results, this impact combination is not a weak spot, as originally anticipated. In fact, this combination showed an ideal energy transfer relationship.

7.10 Point C Analysis – Zero Angle of Incidence

Another obvious potential weak spot is the gap where four biplates come together, that is Point C from Figure 32. This is considered a weak spot because at this location only the edges and corners of the biplates may absorb energy and destroy the projectile tip. For this simulation a direct impact on the center of gap is considered (Figure 51). This is mainly because of the results provided in Section 7.7, showing that a 45° impact on a weak spot does not necessarily imply a failed test, and partly because at this location there are two possible oblique angles to consider.

The geometry considered for this analysis is shown in Figure 51, and the element mesh is shown in Figure 52, while some mesh statistics are shown in Table 42.

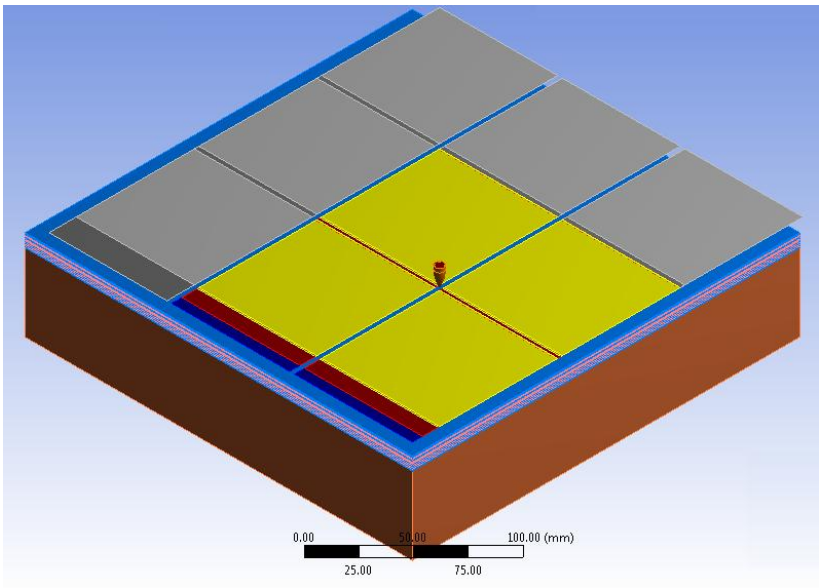

Figure 51 Body layout used for the Point C direct impact analysis.

Notice that the projectile is located directly above the Point C impact location and that there are four biplates that may potentially absorb energy and participate in the analysis.

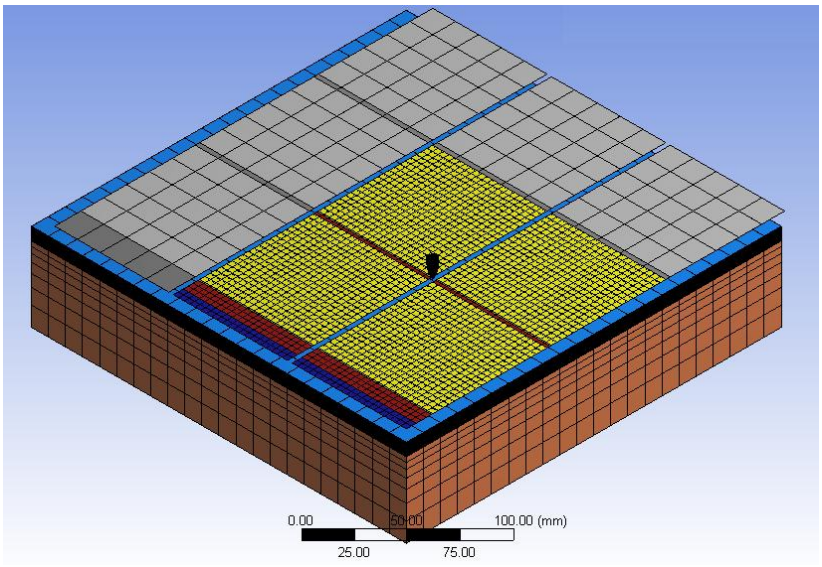

Figure 52 Finite element mesh used for Point C direct impact analysis.

As shown in Figure 52, the overall element size had to be increased as compared to the Point A and Point B simulations because of the number to contributing biplates increased to four.

Table 42 Mesh statistics used for Point C direct impact analysis.

Nodes	41752
Elements	29047
Average aspect ratio	8.011
Average Jacobian ratio	1.001
Relevance Center	Coarse
Relevance	95

The increase in element size caused the aspect ratio to increase to just over 8, however the Jacobian ratio is still about 1, and therefore this model may be compared to the others.

Figure 53 shows six clips captured from the resulting analysis video of the NIJ IIA simulation (9×19 mm NATO simulated projectile) at Point C.

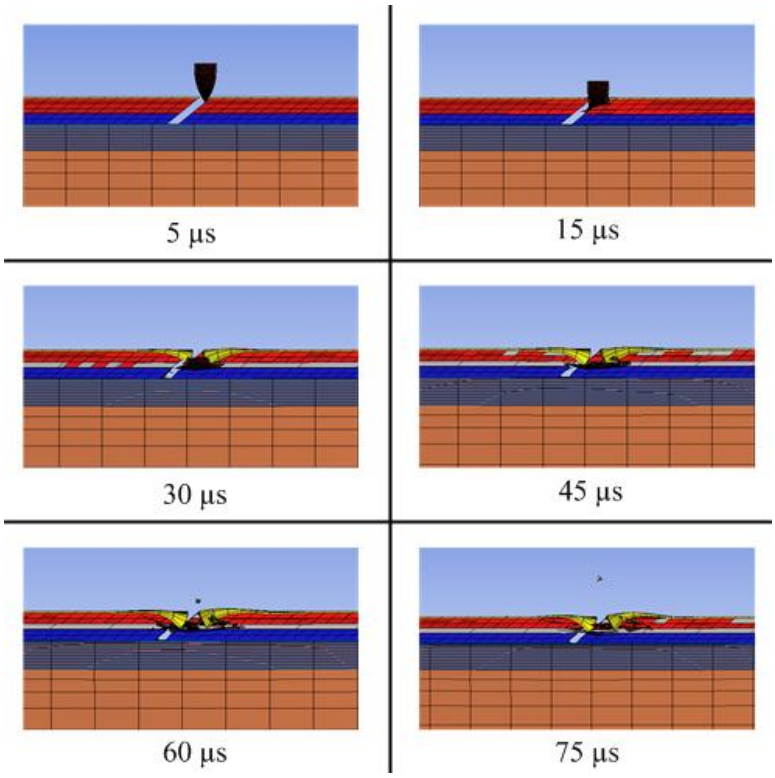

Figure 53 Six video clips from analysis of Point C direct impact.

As shown in Figure 54, the projectile is literally split, almost symmetrically, between all four biplates being impacted. This division of dynamic forces does very well to protect the wearer of the proposed hybrid armor system.

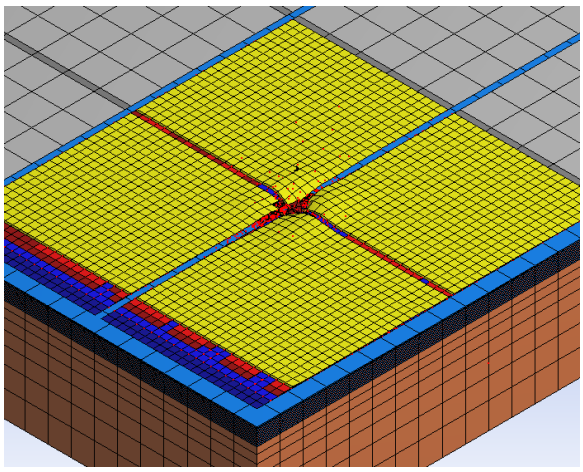

Figure 54 Final clip of the Point C impact - Orthographic view shown.

Table 43 shows the tabulated results of the predicted outcome in the NIJ P-BFS test for the various impact velocities at this location.

Table 43 Predicted outcome of P-BFS test at Point C.

	I	IIA	IIIA	III
Maximum deflection, BFS (mm)	0.25	0.57	1.14	1.25
Penetration detected (Yes, No)	No	No	No	No
Aluminum perforation (Yes, No)	No	No	No	No

Much like the Point B oblique results, the results here indicate that this location is not a weak spot, as first expected. Point C did very well in terms of minimizing BFS and stopping the projectile in all cases, regardless of impact velocity. This is largely due to the excellent distribution of dynamic forces and energy to each of the four impacted biplates.

The average body velocity of the projectile is recorded for all four simulations and may be seen in Figure 55.

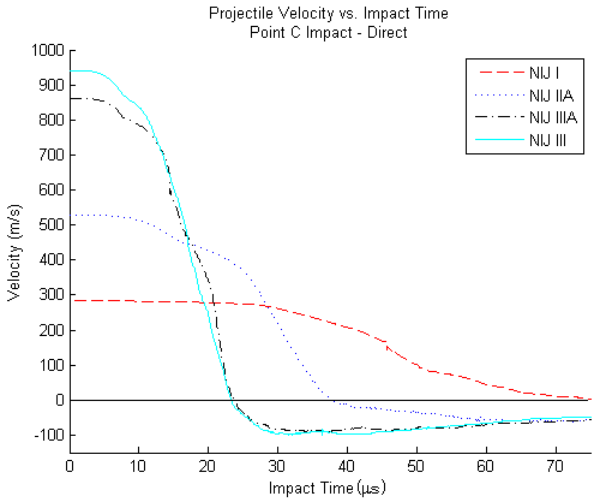

Figure 55 Average mass velocity of each simulation during the Point C impact time.

Although compared to the other locations, this point differed in response in the P-BFS test, but not much in the velocity profile response. As shown in Figure 55, the

velocity profile of both the NIJ IIIA and III tests decreases rapidly whereas the NIJ I and IIA velocities for the most part decrease steadily. This is very similar to all other tests conducted.

7.11 Point D Analysis – Zero Angle of Incidence

As mentioned in Section 6.4 Geometry Selection of the Biplate, a third potential weak spot is that of an impact to the danger zone. This area, found by the calculated dwell duration and skew angle, is characterized by the area in the outer edge of the biplate, or Point D of Figure 32. For this analysis, the impact velocities, end time and other settings were held constant from the previous simulations.

Figure 56 shows the geometry considered for the analysis.

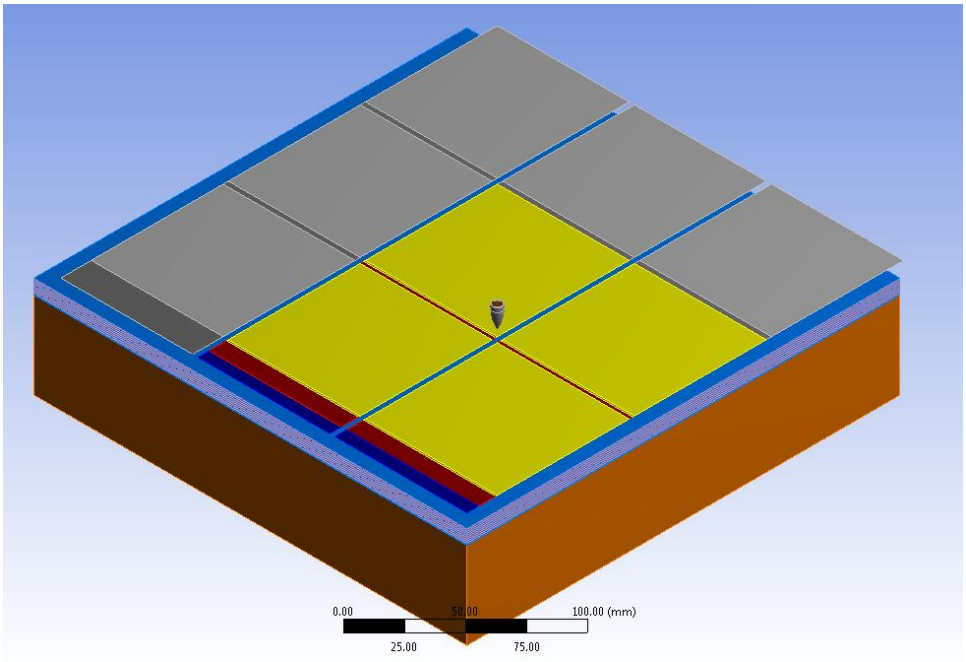

Figure 56 Point D analysis geometry considered.

The same techniques, such as body sweep, were used to generate the element mesh shown in Figure 57. The mesh densities for the biplates and other armor components are similar to what was used for the Point C analysis.

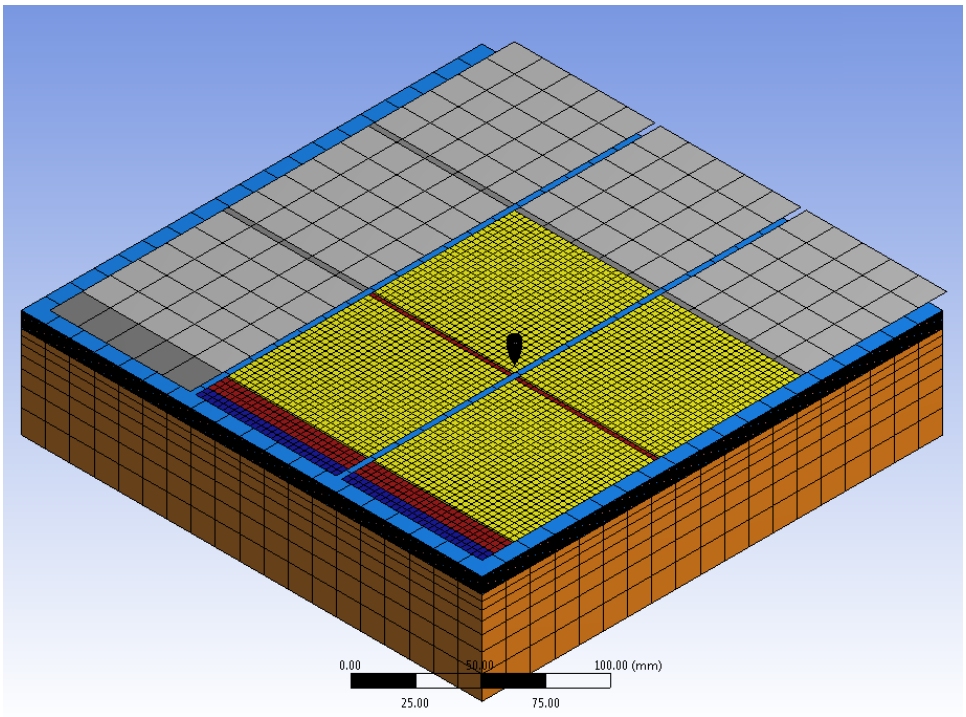

Figure 57 Element mesh used for the oblique center impact.

Some of the mesh statistics for the Point D analysis are shown in Table 44.

Table 44 Mesh Statistics for the Point D FEA.

Nodes	44915
Elements	30567
Average aspect ratio	6.867
Average Jacobian ratio	1.002
Relevance center	Coarse
Relevance	60

Because of the increased element size the aspect ratio is about 6.8, which does show room for improvement, but the Jacobian ratio is just over 1, which is still close enough to be able to accurately compare this model to the others.

Figure 58 shows six of the captured frames from the simulation video of the NIJ IIA danger zone Point D impact.

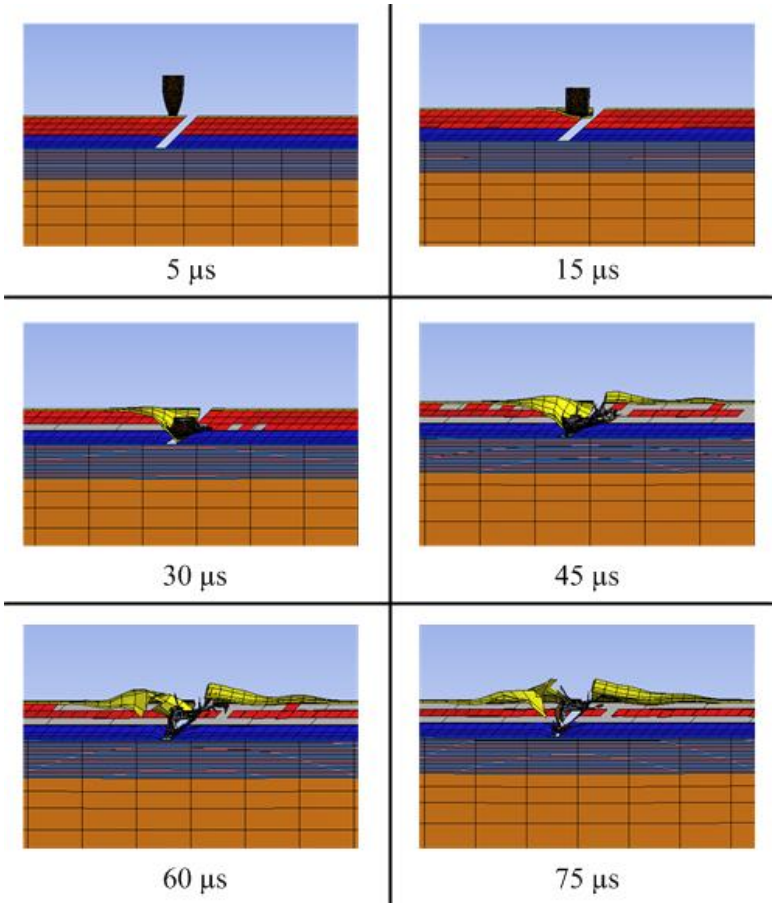

Figure 58 Six frames of the analysis of the Point D danger zone impact.

The results in the simulation video show a similar outcome to that of the Point C analysis. The majority of the impact energy is absorbed by the center plate. However, once the center plate is impacted, fragments begin to impact the adjacent plates, helping to distribute the dynamic loads and energy. One can also see that the projectile is destroyed within the first few moments of impact, helping to distribute the loads to the adjacent plates.

The predicted P-BFS results for the danger zone, Point D impact are shown in Table 45.

Table 45 Simulation results for Point D impact.

	I	IIA	IIIA	III
Maximum deflection, BFS (mm)	0.24	0.51	2.51	4.67
Penetration detected (Yes, No)	No	No	No	No
Aluminum perforated (Yes, No)	No	No	No	No

The results shown for the P-BFS test indicate that this impact point is not a weak spot. This impact combination effectively distributed the dynamic loads and energy much more efficiently than anticipated.

The recorded projectile average mass velocity is shown in Figure 59.

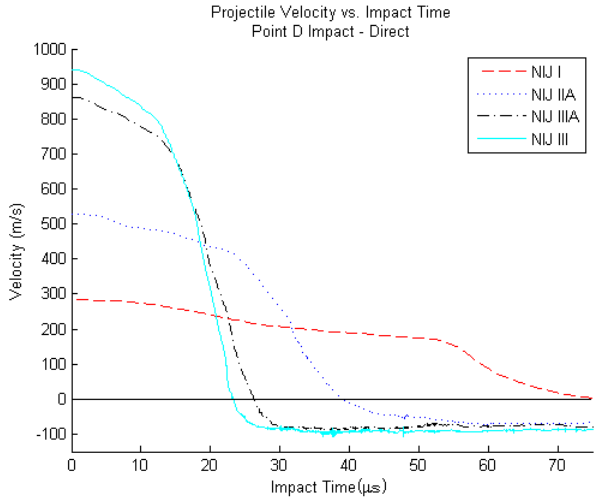

Figure 59 Average projectile mass velocity in the normal direction.

As with the all of the previous velocity profile results, the same trend holds true. The profile of the NIJ IIIA and III is that of a rapid decreasing response, and the NIJ I and IIA is that of a gradual decreasing response.

7.12 Summary of FEA Results

A summary of the FEA results showing the BFS predicted values for impact Points A, B, C, and D is shown in Table 46 and the penetration results are shown in Table 47.

Table 46 Summary of BFS for the various tests.

	Max BFS (mm)			
	NIJ I	NIJ IIA	NIJ IIIA	NIJ III
Point A Direct	0.67	10.94	35.50	> 55
Point A Oblique	0.42	5.05	> 55	36.80
Point B Direct	0.89	10.85	47.60	> 55
Point B Oblique	0.14	1.03	7.30	3.49
Point C Direct	0.25	0.57	1.14	1.25
Point D Direct	0.24	0.51	2.51	4.67

Table 47 Summary of the penetration detection for the various tests.

	Penetration Detection (overall | aluminum)							
	NIJ I		NIJ IIA		NIJ IIIA		NIJ III	
Point A Direct	N	N	N	N	N	Y	N	Y
Point A Oblique	N	N	N	N	Y	Y	N	Y
Point B Direct	N	N	N	N	N	Y	Y	Y
Point B Oblique	N	N	N	N	N	N	N	N
Point C Direct	N	N	N	N	N	N	N	N
Point D Direct	N	N	N	N	N	N	N	N

The preliminary analysis results of the proposed hybrid semi-flexible armor system show that it is capable of protecting the wearer against NIJ level I and IIA projectiles in all hit locations, and the many of the NIJ IIIA and NIJ III impact combinations. Furthermore, only two impacts resulted in a complete perforation of the armor system, and only six of the twenty four simulations resulted in a perforation of the ballistic biplate. This indicates a good multiple hit capacity.

The velocity profiles for each impact scenario proved to be very similar for each NIJ level, regardless of hit location or angle of incidence. This outcome at first seemed strange, however later proved not to be a coincidence. The critical velocity of the armor is determined to be the reason why the higher velocity impacts resulted in a very rapid decline, whereas the lower velocity impacts resulted in a more gradual decline in projectile velocity (David, Gao and Zheng 2009). The critical velocity is an armor

parameter that is dependent upon many factors such as, the number and thicknesses of layers, layer materials, angle of incidence, etc. This velocity value is determined by experimental testing, and is at which point there is a distinct difference in failure/fracture mode of the ballistic plate between a sub-critical and super-critical impacts. For a typical ballistic plate, a sub-critical impact would result in a plate failure by stacking faults and microtwins produced by plastic deformations during the impact (David, Gao and Zheng 2009). On the other hand, a super-critical impact would typical result in a ballistic plate failure by a mode of solid-state transformation, as observed on a nanoscale, from crystalline to amorphous caused by the high impact strain rate (David, Gao and Zheng 2009). The critical velocity of the proposed armor system is something that is recommended to be investigated further in future studies.

7.13 Energy Distribution during Impact

For a body armor system, one of the key design parameters is the energy absorption capability of each component as used in the system. The amount of energy that a component can absorb may change, if tested individually and separately from the armor system as a whole. The amount of energy absorbed by each piece, including the wearer (in this work, the clay) was recorded in ANSYS 12.1 (SAS IP, Inc. 2009) during the finite element analysis and imported into MATLAB® (TheMathWorks, Inc. 2008) as a text file. The energy absorption data was then analyzed to determine the percentage of total energy absorbed by each component. This technique provides another outlook to the performance of the armor system, beyond simply the perforation and backface signature test results.

Table 48 shows the percent of the total system energy absorbed for the various armor components. Several components are not included in this table but are included in the total energy summation, such as the total projectile energy, and the top biplate layer (Kevlar®) energy.

Table 48 Percent system energy absorption summary per component.

	Percent Energy Absorption (%)			
Point A Direct	Ceramic	Aluminum	Kevlar	Clay
NIJ I	0.754	84.83	3.53	0.169
NIJ IIA	0.708	12.77	83.72	1.255
NIJ IIIA	0.814	5.786	76.05	16.83
NIJ III	21.74	5.674	29.15	42.35
Point A Oblique	Ceramic	Aluminum	Kevlar	Clay
NIJ I	0.656	82.75	4.169	0.248
NIJ IIA	1.128	36.02	56.13	1.413
NIJ IIIA	7.699	3.450	63.92	24.45
NIJ III	10.93	23.03	46.02	17.77
Point B Direct	Ceramic	Aluminum	Kevlar	Clay
NIJ I	0.2412	14.62	83.70	0.0204
NIJ IIA	0.3675	10.06	88.10	0.542
NIJ IIIA	1.122	0.109	98.66	0.064
NIJ III	1.539	11.40	4.963	81.62
Point B Oblique	Ceramic	Aluminum	Kevlar	Clay
NIJ I	0.603	85.69	0.474	0.074
NIJ IIA	1.193	80.67	6.172	0.333
NIJ IIIA	1.023	11.45	84.73	1.159
NIJ III	0.591	47.95	43.95	1.042
Point C Direct	Ceramic	Aluminum	Kevlar	Clay
NIJ I	0.724	83.36	0.129	0.019
NIJ IIA	0.502	85.35	0.237	0.097
NIJ IIIA	0.466	86.81	0.882	0.278
NIJ III	0.595	86.82	1.135	0.673
Point D Direct	Ceramic	Aluminum	Kevlar	Clay
NIJ I	1.860	95.02	0.081	0.010
NIJ IIA	0.084	95.36	0.153	0.056
NIJ IIIA	0.303	52.36	45.11	0.555
NIJ III	0.238	39.93	58.09	0.592

Table 48 shows that in most cases, for the two lower impact velocities the majority of the energy was absorbed through the aluminum portion of the armor. In

contrast, for the higher two impact velocities, the majority of the energy absorbed is via the Kelvar® layers and the clay. This shift in energy absorption is possibly related to the previously mentioned armor critical velocity. This is thought to be the culprit because at these higher impact velocities, the aluminum is penetrated leaving the Kevlar® to absorb the remaining energy.

One should also take note that in two of the potential armor weak spots (Points C and D), the percentage of energy absorbed by the clay was actually lower than that of a direct center plate impact (Point A). Upon evaluation, it is determined that this is mainly because the projectile impact energy and dynamic loads are distributed to more than one plate, and in turn this increases the contact area for all subsequent layers, thus reducing stress and inward clay deflection.

It was always observed that in the simulations where the Kevlar® layers absorbed the majority or near-majority of the energy, the layers were typically torn apart and reduced to a non-structural armor component. This is an important thing to consider because the multiple-hit capability of the armor is heavily dependent upon the Kevlar® (and all other components) layers remaining at least somewhat intact.

7.14 Equivalent Thickness of Kevlar in Lieu of Plates

There are many "what if" questions that can be asked about the design of an armor system. One of these questions is: What if the biplates are replaced with an equivalent thickness of plain-woven Kevlar® layers? This type of armor design would contain thirty-three layers of 0.5 mm thick Kevlar® sheets, and is shown in Figure 60.

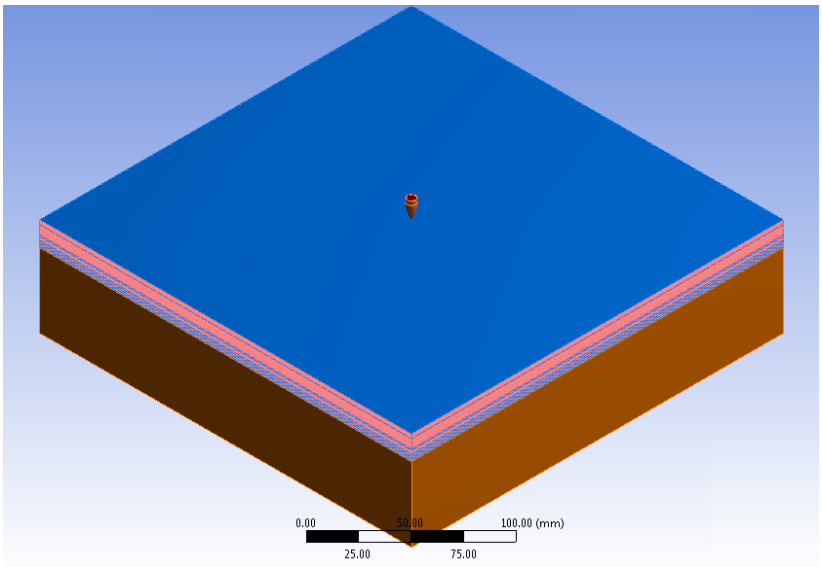

Figure 60 Geometry showing the replacement of biplates with layers of Kevlar.

The question of replacing the biplates with Kevlar® layers can be answered using the same techniques in Sections 7.5 through 7.11. And in a similar fashion to those sections, finite element analysis is used to determine the effect of using thirty-three layers of plain-woven Kevlar® 29 fibers in lieu of biplates.

The same four impact velocities, projectile geometry and clay properties are used for the analysis in this section as in the previous sections. The element mesh is shown in Figure 61, and the element statistics are shown in Table 49.

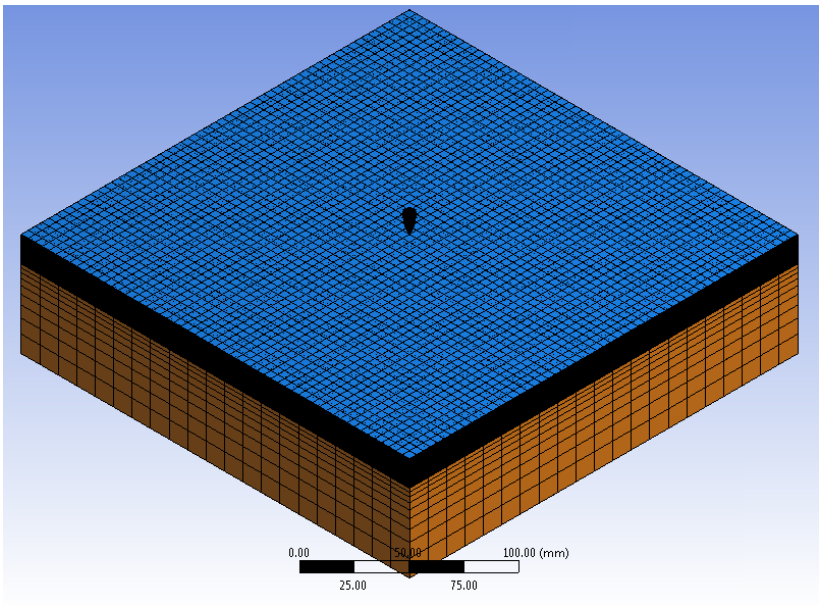

Figure 61 Mesh used to conduct the FEA on the replacement geometry.

Figure 61 shows that the same meshing techniques were used to model the replacement geometry as in the other sections. In this case, the aspect ratio is rather large and could use some improvement.

Table 49 Mesh statistics for the analysis of the replacement geometry.

Nodes	48782
Elements	29240
Average aspect ratio	13.896
Average Jacodian Ratio	1
Relevance	74
Relevance center	Coarse

Figure 62 shows six clips from the NIJ IIA resulting simulation.

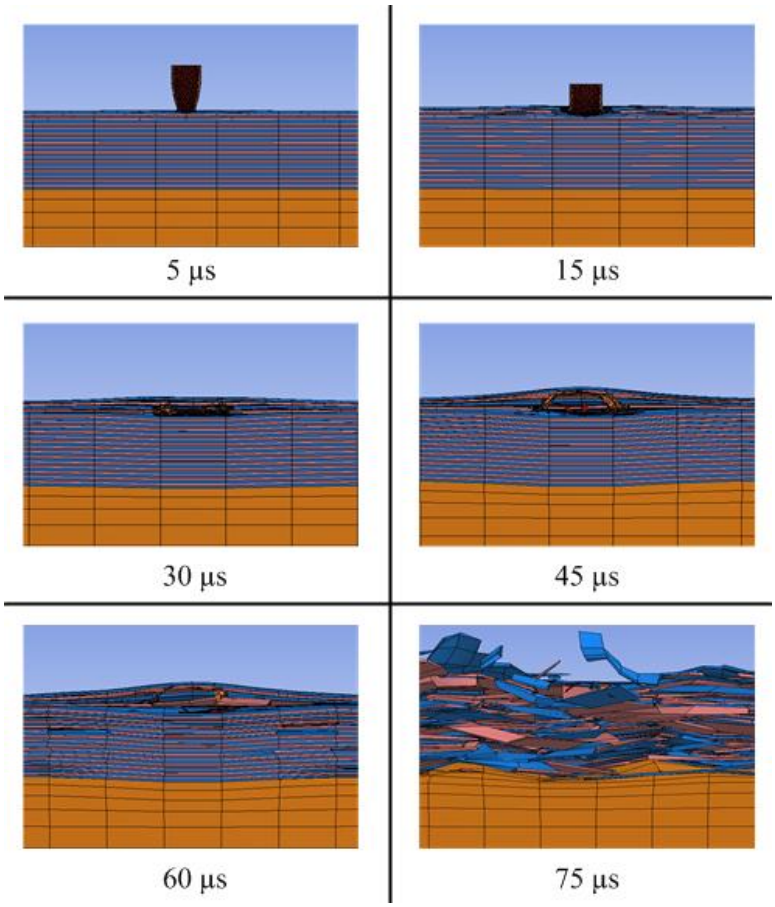

Figure 62 Six video clips of the simulated projectile into replacement layers.

The theoretical results of the P-BFS test given in Table 50 and shown in Figure 63 depict the mass velocity of each simulated projectile during the impact time.

Table 50 Predicted results of the P-BFS test for the replacement geometry configuration.

	I	IIA	IIIA	III
Maximum deflection, BFS (mm)	1.87	12.29	9.88	10.70
Penetration detected (Yes, No)	No	No	Yes	Yes

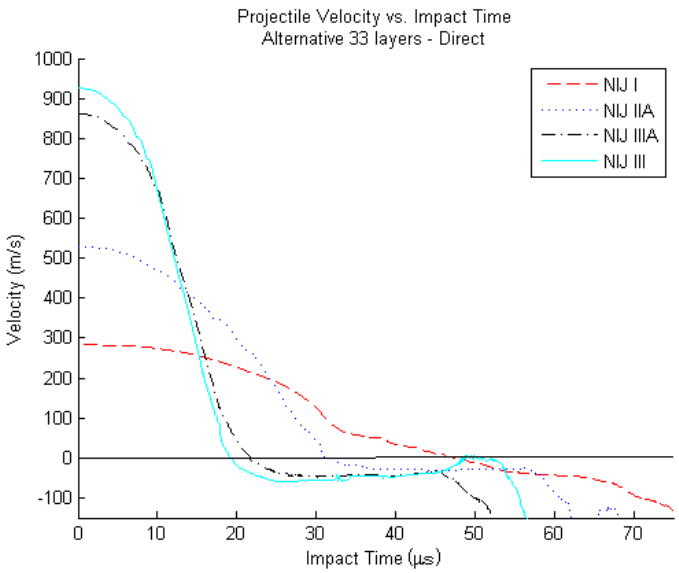

Figure 63 Average mass velocity of each projectile in the replacement configuration.

As shown in Figure 63, the average velocity profiles for the projectile are very similar to those of the biplate finite element analysis testing results. The projectile in the NIJ IIIA and III tests rapidly decreases, whereas the NIJ I and IIA velocities decreases more gradually.

Upon first review, the results in Table 50 may seem to justify the use of a thirty-three layer armor system in place of the hybrid ballistic plate and textile armor system presented; as all of the four simulations have a BFS less than 44 mm. However, with one impact from an NIJ IIA, IIIA, or III projectile, all of the armor layers are completely destroyed, as shown in the last clip. This leads to a predicted failure of the NIJ P-BFS test with any NIJ IIA, IIIA, or III impact. Additionally, things such as multiple-hit capacity, flexibility, durability, and feasibility must all be considered. As shown, the alternative thirty-three layer armor system does not likely posses a multiple-hit capacity. Meaning, after being struck one time, the armor cannot be depended upon to protect the wearer against any follow through projectile strike. This alone is enough to deem it a failure in

the P-BFS test. Additionally, the durability and feasibility is questionable, simply because of environmental conditions, such as ultra-violet light, humidity, and extreme temperature (low or high) that may break down Kevlar®. With the presented hybrid armor system, the woven Kevlar® layers are contained in a plastic container and stored in the lower compartment of the armor carrier, which make them easily removable and replaceable.

Another thing to consider regarding the thirty-three layer Kevlar® replacement system is how the armor system would theoretically counter sharp pointed objects and/or shrapnel fragments. Normally, to protect against sharp pointed objects (such as a knife or bayonet) and shrapnel, hard materials are used (Croitoro and Boros 2007). Woven Kevlar® layers would likely be penetrated if stabbed or hit by an oddly-shaped pointed piece of shrapnel.

7.15 Discussion of Results

The purpose of the preliminary finite element analysis shown in this chapter is to determine if the presented armor system is feasible. Based upon the results of the finite element analysis, the purposed semi-flexible hybrid armor system shown shows great potential in being further developed into a full scale NIJ level III armor system. Furthermore, as shown in the current configuration, the analysis results indicate that the armor can safely protect the wearer against all NIJ IIA impacts, most NIJ IIIA impacts and some NIJ III impacts. This would theoretically place the armor system as a NIJ II to IIIA level armor, the same rating or better as the PASGT armor system used by the U.S. Armed Forces from the 1980s up until the turn of the 21st century.

The results also indicate that simply replacing the ballistic plates with Kevlar® layers will result in a failed P-BFS test on account that the multiple-hit requirement will more than likely not be met, among other possible failures.

CHAPTER 8 DESIGN OF EXPERIMENTS

A formal design of experiments (DOE) study is used to help analyze the data obtained from the finite element analysis. Particularly, the results from the DOE study will help to determine which factors contribute to the energy absorbed by the various components of the armor system and most importantly, by the wearer (in this case, the clay).

8.1 Design of Experiments – Setup

The DOE study conducted for this work examined how the various impact velocities and hit locations affected the ability for the aluminum, Kevlar®, and clay components to absorb energy. Three separate studies were conducted to preliminarily determine how

1) velocity,
2) impact location, and
3) the combined effect of velocity with impact location,

contributed to the energy absorbed by the

1) aluminum,
2) Kevlar layers®, and
3) clay (wearer).

Table 51 shows the factors and the values for used for the DOE analysis.

Table 51 Values of different levels of the DOE factors.

Factor	Symbol	Level 1	Level 2	Level 3	Level 4
Velocity	V	282.8	527.49	860.81	940
Location	L	A	B	C	D

The velocity levels are based on NIJ levels and are given in Table 32. The location points, A, B, C, and D correspond to the impact locations used for the finite element analysis as shown in Figure 32.

The software used to complete the DOE was Microsoft Excel (Microsoft, Inc. 2009) used in conjunction with Minitab 15 (Minitab Inc. 2007). The overall goal of this design of experiments study is to provide insight into the energy absorption mechanisms, and as a tool to further develop the hybrid armor system.

8.2 Design of Experiments – Outcome

Upon completing the DOE study, Figure 64, Figure 65 and Figure 66 were generated. One can see the effect of velocity, location and the combined effect of location and velocity on the ability for the aluminum layer to absorb energy in Figure 64.

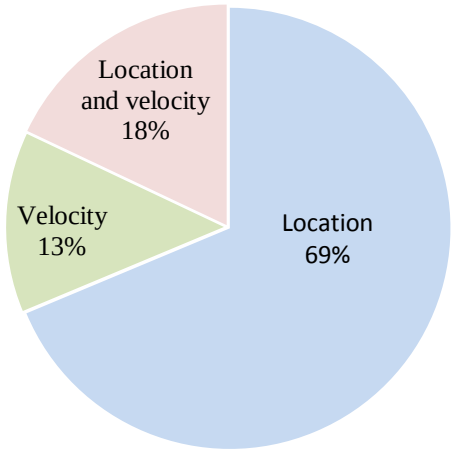

Figure 64 Percent contribution to energy absorption by aluminum.

As shown, the largest contribution, at 69%, to the ability of the aluminum to absorb energy is the location of the impact. Furthermore, it is shown that impact velocity alone and the combined effect of velocity and impact location do not contribute nearly as much as location alone. This means that the plate spacing, top area, and critical width have more of an effect on the energy absorption ability of the aluminum than the impact velocity of the projectile. This trait follows the analysis as well. If impacted in the Danger Zone, the biplate does not have a maximum aluminum-oxide aluminum contact area, and thus the aluminum cannot absorb energy. Similarly, if impacted in any gap (such as Point B or C), the aluminum does not make full contact with any other component and thus cannot absorb energy. On the other hand, if impacted in a location such as Point A, the aluminum-oxide aluminum contact area is high and the aluminum may then absorb energy.

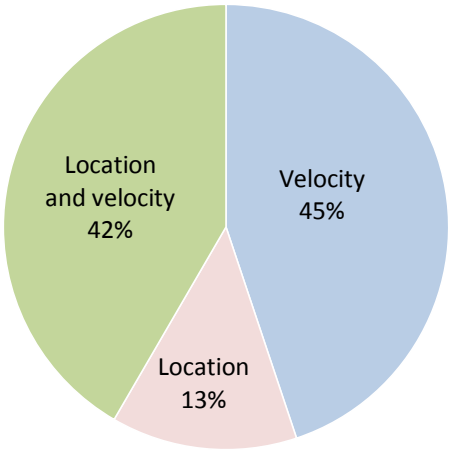

Figure 65 Percent contribution to energy absorption by Kevlar layers.

In Figure 65 one can see the contributions to the ability of the Kevlar® layers (all 16) to absorb energy. As shown, the hit location alone does not contribute as highly as the velocity alone does to the ability to absorb energy. This study shows that the spacing of the plates, the angle of skew, and the biplate layer thicknesses are acceptable. If one of these design parameters was faulty, the location of the impact would contribute a higher percentage than what is presented.

The most important component to analyze is the clay, as these results are directly related to the survivability of the wearer. Figure 66 shows how the absorption of energy to the clay is affected by the various impact parameters.

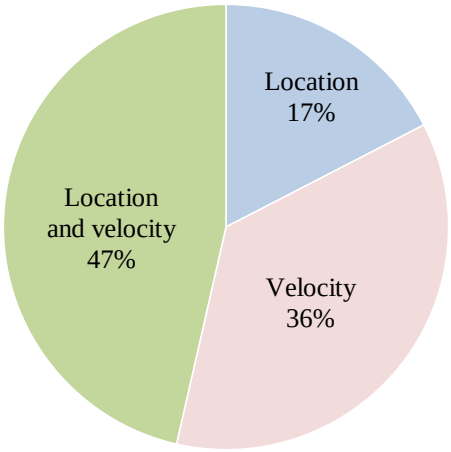

Figure 66 Percent contribution to energy absorption by clay.

As shown, velocity alone contributes 36% to the energy absorption ability of the clay, whereas location and velocity combined contribute 47% to the ability of clay to absorb energy. These outcomes are as expected; as the kinetic energy of the projectile increases, the energy transfer to the clay will be larger. The impact location only contributes 17% to the energy absorption of the clay, which is the minimum effect. This is a good indicator of the ability of the armor system as a whole to distribute the dynamic loads, regardless of impact location. These results further verify that the biplate thickness(es), spacing, angle of skew and Kevlar® layer quantities are all acceptable for the system.

Overall, the DOE results show that further from the impact point, the less effect location has on the ability to absorb energy, again reinforcing the capability for the armor system as a whole to distribute loads. Also, the results show that the further from the impact point, the more effect that velocity has on the ability of the respective component to absorb energy.

On the onset on this work, these two relationships were unknown, and with the now known relationships presented, the optimization and development of the armor may be more focused in future work.

CHAPTER 9 PROJECT DISCUSSION

9.1 Limitations on the Analysis and on the Project

The FEA shown is limited by a number of things. The primary limitation is the number of permitted nodes by the available license. Additionally, the computational resources currently available are a limiting factor. Both of these factors limit the overall analysis time and increase the analysis error and hourglass energy. Hourglass energy is a fictional energy source created by ANSYS to simulate the realistic dynamic response of stiff materials (SAS IP, Inc. 2007). This was one of the main problems in the analysis, and to reduce hourglass energy it is recommended that one increase the mesh density. However, this was impossible given the nodal limitations (SAS IP, Inc. 2007).

With unlimited or near-unlimited restrictions on nodes and computational resources, the finite element analysis could be conducted on a larger scale (actual size), with the armor carrier, and without the non-impacted plates being modeled as rigid. Moreover, the mesh density could be increased to more accurately simulate the material failure and/or facture. With increased computational resources, the overall analysis time could be increased as well, thus to further investigate the energy transfer mechanisms and to ensure that the maximum BFS is reached.

9.2 Method of Improvements toward Final Design

Some areas of improvement can be picked out for the final armor based on the summary of results shown in Table 46, Table 47, and Table 48. The areas of further improvement, research and development are:

1) the implementation of a damping mechanism for high velocity strikes,
2) determining the ballistic limit of the armor system,
3) determining the velocity at which statistically half the impacting projectiles penetrate the armor, or the V50,
4) study the mobility and dexterity characteristics of the entire armor system,
5) complete the design and then implement and optimize the armor carrier vest, and
6) determine if the armor has a positive buoyancy.

Work in these six areas will insure that an effective alpha prototype is created and experimentally tested with minimal need for other expensive testing before final production.

The first two areas of improvement are directly related to the rapid velocity decline of the high velocity impact. This high change of velocity over a short period time increases impulse to the clay, thus the maximum backface signature is increased as well. If the impact velocity could be held below the critical velocity and/or a damping mechanism was introduced, the impulse to the clay would be decreased and in turn decrease the BFS. This area of armor design is not widely researched, although some damping systems have been proposed to reduce blunt trauma to the wearer, with the

overall goal of reducing the likelihood of fractured bone structure and damaged organs (David, Gao and Zheng 2009).

The next area of necessary research is Item (3), to determine the V50 of the armor. This is rating, much like the NIJ level, which is the second required National Institute of Justice test, after the P-BFS test. This test can be simulated, and often is, using finite element analysis to predict the V50 value for the hybrid armor setup.

Items (4) and (5) are both related to the flexibility of the hybrid armor, and are to develop a quantitative mobility and dexterity study and to complete the design the armor carrier. These items must be completed after the armor system is optimized by determining the ballistic limit and the V50, as these two items may change the armor dimensions. It should be noted that a quantitative mobility and dexterity study is not a well-researched topic, although such a study is highly needed in this and many other fields.

The last item is to determine if the armor possesses positive buoyancy. This is set as a current design subgoal and is an important consideration because in the event that the wearer falls into a body of water, the individual will potentially float or be assisted to the surface if the armor posses a positive buoyancy. Currently, the underlying Kevlar® layers in the lower compartment are contained inside a thin sealed plastic case. This is to keep the layers separate from environmental factors, including water. This setup is thought to increase the positive buoyancy of the armor, and is currently the only method designed into the hybrid armor to do such.

9.3 Analysis Results and Outcomes in Terms of Design Goals

After completing the finite element analysis and preliminary design, it is safe to determine that the semi-flexible hybrid armor system will indeed offer the wearer an ideal balance of protection and flexibility. This balance, proven by existing technology, such as the flexible stab resistance armor array (Croitoro and Boros 2007), will help to accomplish the first objective - to increase the mobility and dexterity of the wearer. Additionally, the user will be able to easily adjust the desired protection level by adding or removing the ballistic biplates, made possible by the integrated elastic straps.

The completed armor system will be contained in a two compartment armor vest, worn in a similar fashion to currently produced ballistic vests. However, the completed semi-flexible vest will extend the rifle protection area higher in the underarms in lower in the groin and torso sections. These extensions will help accomplish the second objective - to increase the NIJ IIIA/III protection area. As a result of the added protective area, soldiers and law enforcement officers will have higher levels of confidence and morale, and in the event they are struck by a bullet, their likelihood of survivability will be increased.

Using Equation 2 and the material properties in Table 10, Table 11 and Table 14, the predicted areal density of the hybrid armor system is 43.87 kg/m^3. This areal density shows a decrease of approximately 36% compared to similar protective hard armor systems shown in Table 9. The reduced areal density will yield weight reductions in the vest and insure that the third design objective – to reduce the armor areal density, is accomplished.

The overall thickness of the armor system is a mere 16.8 mm. This value does not include the armor carrier vest which is still in the design phases. To maintain the overall thickness subgoal of less than 20 mm, the armor vest may only contain 3.2 mm of thickness in material. This is definitely possible, and is a consideration for the final design of the armor carrier vest.

9.4 Concluding Remarks

This work set out to address the issue of the balance of mobility and protection inherent in personal body armor vests. The solution presented mixes proven technology with advanced computational techniques to increase the wearer's mobility. The result is a well balanced hybrid armor system, capable of providing the wearer with rifle projectile protection. This is made possible by using a matrix of specially designed small ballistic plates placed on top of flexible woven Kelvar® layers. Additionally, the hybrid armor system presented shows a significant decrease in overall armor weight, thus adding to the user's mobility. The analysis conducted shows that the armor system is capable of complying with the NIJ level II or NIJ level IIIA requirements, without any further modifications. Furthermore, this work recognizes areas of improvement that were found by using both finite element analysis and design of experiments to increase the potential armor rating to NIJ level III, the ultimate goal.

The semi-flexible hybrid armor system shows great potential in accomplishing all three design goals and both design subgoals set forth at the onset of this work. In fact, the analysis shows that two of the three design goals and potentially all of the design subgoals are met with the beta semi-flexible hybrid personal body armor shown.

REFERENCES

Bashford, Dean. *Helmets and Body Armor.* New Haven, NY: Yale University Press, 1920.

Berg, Vanessa, Jerome Stofleth, Matthew Risenmay, and Dale Preece. "Kevlar and Carbon Composite Body Armor - Analysis and Testing." *Proceedings of the ASME Pressure Vessels and Piping Conference*, 2005: 787-795.

Bittinger, Beecher, Ellenbogen, and Penna. *Precalculus Graphs and Models.* Second. Addison Wesley Longman, Inc., 2001.

Brady, Christopher G. *An Analysis of Wound Statistics in Relation to Personal Ballistic Protection.* Edinburgh South Australia: DSTO Systems Sciences Laboratory , 2003.

Chocron, Benlouo, and Sanchez Galvez. "A New Analytical Model to Simulate Impact onto Ceramic/Compsite Armors." *International Journal of Impact Engineering* 21 (1998): 461-471.

Crandall, S.H., L.G. Kursweil, and A.K. Kigam. "On the Measurement of Poisson's Ratio for Modeling Clay." *Experimental Mechanics*, 1971: 402-407.

Crandall, Stephen H., Leonard G. Kurzwell, Anant K. Nigam, and Paul J. Remington. *Dynamic Properties of Modelling Clay.* Analysis Results, Acoustics and Vibration Laboratory, Massachusetts Institute of Technology, Cambridge: Massachusetts Institute of Technology, 1970, 105.

Croitoro, Elena M., and I. Eugen Boros. "Flexible Stab Resistant Ceramic-Based Body Armor." *Transactions of the CSME* 31 (2007): 157-165.

David, N.V., X.L. Gao, and J.Q. Zheng. "Ballistic Resistant Body Armor: Contemporary and Prospective Materials and Related Protection Mechanisms." *Applied Mechanics Reviews*, 2009: 050802-1-050802-20.

Davila, C.G., and Tzi-Kang Chen. "Advanced Modeling Strategies for the Analysis of Tile-Reinforced Composite Armor." *Applied Composite Materials* 7 (2000): 51-68.

Discovery Media. *Museum of Learning.* January 17, 2011. http://www.museumstuff.com/learn/topics/Myeonje_baegab (accessed January 17, 2011).

DuPont. *Technical Guide, Kevlar Aramid Fibers.* Richmond, VA: DuPont, 2010.

Encyclopaedia Britannica. *Flak Jacket.* December 2010, 2010. http://www.britannica.com/EBchecked/topic/209325/flak-jacket (accessed January 17, 2011).

Fellows, N.A., and P.C. Barton. "Development of Impact Model for Ceramic-Faced Semi-Infinite Armour." *International Journal of Impact Engineering* 22 (1999): 793-811.

Fickler, M.L. "Ballistic Injury." *Annals of Emergency Medicine*, December 1986: 111-114.

Fickler, M.L. "Wounding Patterns of Military Rifle Bullets." *International Defense Review*, January 1989: 59-64.

Gellert, E.P., S.D. Pattie, and R.L. Woodard. "Energy Tansfer in Ballistic Perforation of Fibre Reinforced Composties." *Journal of Materials Sciences* 33 (1998): 1845-1850.

Grau, Lester W., and Dr. William A. Jorgensen. "Handling the Wounded in a Counter-Guerrilla War: the Soviet/Russian Experience in Afghanistan and Chechnya." *U.S. Army Medical Department Journal*, January/Febuary 1998.

Greenwood, Donald T. *Principles of Dynamics.* Upper Saddle River, NJ: Prentice Hall, 1988.

Hahn, H. Thomas, Jenn Ming Yang, Sung S. Suh, and Nanlin Han. *Design, Manufacturing, and Performance of Stitched Stiffened Composite Panels With and Without Impact Damage.* Technical, Federal Aviation Administration, Los Angeles: U.S. Department of Transportation, 2002.

Hannon, F.S., and K.H. Abbott. "Ceramic Armor Stops Bullets, Lowers Weight." *Material Engineering*, September 1968: 42-43.

Hodge, N. "US Seeks to Switch Body Armour." *Jane's Defense Weekly*, June 2006: 623-624.

Kaw, Autar K. *Mechanics of Composite Materials, Second Edition.* Boca Raton, FL: CRC Taylor & Francis, 2006.

Lardner, R. "Less Body Armor May be the Answer in Afghanistan." *Associated Press*, March 10, 2009.

Li, X., et al. "Preparation of Body amour materials of Kevlar fabric treated with colloidal silica nanocomposite." *Plastics, Rubber and Composites* 37 (2008): 223-226.

Logan, Daryl L. *A First Course in the Finite Element Method.* Edited by Fourth. Toronto, Ontario: Thomson, 2007.

Lopez, C. Todd. "Soldier Testifies to Congress on Body Armor." *Army News Services*, February 5, 2009.

MatWeb. *AISI Type S1 Tool Steel, Quenched 955°C (1750°F), Tempered 250°C (500°F).* 2010. www.matweb.com (accessed January 17, 2011).

—. *Alumina, 99.9%, Al2O3.* 2010. www.matweb.com (accessed January 2011, 2011).

—. *Aluminum 7075-T6; 7075-T651.* 2010. www.matweb.com (accessed January 17, 2011).

—. *CeramTec Rocar® SiG Silicon Carbide, SiSiC.* 2010. www.matweb.com (accessed January 17, 2011).

—. *CoorsTek Boron Carbide Reaction-Bonded Boron Carbide.* 2010. www.matweb.com (accessed January 17, 2011).

—. *Titanium Ti-4.5Al-5Mo-1.5Cr (Corona 5).* 2010. www.matweb.com (accessed January 17, 2011).

Ministry of Foreign Affairs. *Jan Szczepanik: Polish Edison.* http://en.poland.gov.pl/Jan,Szczepanik,Polish,Edison,1986.html (accessed January 17, 2011).

Minitab Inc. *Minitab® 15.1.30.0.* 2007.

Microsoft, Inc. *Microsoft Excel 2007.* 2009.

Nicky. *The Kelly Armour.* January 10, 2004 . http://www.bailup.com/armour.htm (accessed January 17, 2011).

Norton, Robert L. *Machine Design, An Integrated Approach, Third Edition.* Upper Saddle River, NJ: Pearson Prentice Hall, 2006.

Olive-Drab LLC. *Body Armor (Flak Jackets) in WW II.* May 22, 2008. http://www.olive-drab.com/od_soldiers_gear_body_armor_wwii.php (accessed january 17, 2011).

—. *Body Armor (Flak Jackets) Post WW II.* May 22, 2008. www.olive-drab.com (accessed December 15, 2010).

—. *Interceptor Body Armor System.* May 22, 2008. http://www.olive-drab.com/od_soldiers_gear_body_armor_interceptor.php (accessed Januray 17, 2011).

—. *PASGT Body Armor, Fragmentation Protective Vest.* May 22, 2008. http://www.olive-drab.com/od_soldiers_gear_body_armor_pasgt.php (accessed January 17, 2011).

Pinnacle Armor. *Duty - Uniform Body Armor.* 2010. http://www.pinnaclearmor.com/body-armor/duty-uniform/ (accessed January 17, 2011).

SAS IP, Inc. *ANSYS Workbench 12.1.0 Engineering Data.* Canonsburg, PA, October 29, 2009.

SAS IP, Inc. *ANSYS Workbench 12.1.0 Explict Dynamics.* Canonsburg, PA, October 29, 2009.

SAS IP, Inc. *Theory Reference for ANSYS and ANSYS Workbench.* Official Reference, Canonsburg: ANSYS, Inc and ANSYS Europe, 2007.

Second Chance Body Armor. *2008 Body Armor Catalog.* Central Lake, MI: Second Chance Body Armor, 2010.

Shokrich, M.M., and G.H. Javadpour. "Penetration Analysis of a Projectile in Ceramic Composite Armor." *Composite Structures* 82 (2008): 269-276.

Tabiei, Ala, and Gaurav Nilakantan. "Ballistic Impact of Dry Woven Fabric Composties: A review." *Applied Mechanics Reviews* 61 (January 2008).

Teng, X., T. Wierzbicki, and M. Huang. "Ballistic Resistance of Double-Layered Armor Plates." *International Journal of Impact Engineering* 35 (2008): 870-884.

TheMathWorks, Inc. *MATLAB 7.6.0.324 (R2008a).* 2008.

U.S. Department of Defense. *Department of Defense Test Methods Standards, V50 Ballistic Test for Armor.* Testing Standards, Washinton D.C.: U.S. Govnerment, 1997.

U.S. Department of Justice. *Ballistic Resistance Body Armor, Standards.* Washington DC: U.S. Government, 2008.

Ugural, A.C., and S. K. Fenster. *Advanced Strength and Applied Elasticity.* Upper Saddle River, NJ: Prentice Hall, 2003.

Urey, Patrick. *Handgun Wounding Factors and Effectivness.* FBI Academy, Quantico: FBI, 1989.

vietnamgear.com. *M1952A Flak Vest.* http://www.vietnamgear.com/kit.aspx?kit=21 (accessed January 17, 2011).

White, Frank M. *Viscous Fluid Flow, Third Edition.* New York, NY: McGraw-Hill, 2006.

wikipedia. *SN-42.* June 14, 2010. http://en.wikipedia.org/wiki/SN-42 (accessed January 17, 2011).

Yurasovskiy, A. *Kuyak. XVI century.* http://www.cross-roads.ru/english/armour/kuyak-brigandine.html (accessed January 17, 2011).

APPENDICES

Appendix A: List of Acronyms

Listed in alphabetical order:

AP – Armor Piercing

BFS – Backface signature

DOE – Design of Experiments

FEA – Finite element analysis

IBA – Interceptor Body Armor

ISAPO – Interim Small Arms Protective Overvest

LR – Long Rifle

NATO – North American Treaty Organization

NIJ – National Institute of Justice

PASGT – Personnel Armor System for Group Troops

P-BFS – Peroration-Backface Signature (test)

SN – Stalynoi Nagrudnik (steel bib)

Appendix B: List of Nomenclature

Listed in alphabetical order:

A_C = contact area between aluminum-oxide and aluminum

A_p = areal density

a = speed of sound

$[C_i]$ = stiffness matrix

D_S = distance covered during conoid formation

d_e = eroded projectile tip diameter

d_p = nominal diameter of the projectile

E = Young's modulus

E_k = kinetic energy of a projectile

E_P = residual energy of the projectile

F_g = gap caused by the fill

f = fill (subscript)

fy = fill yarn (subscript)

h_f = diameter of the fill

h_t = height of projectile tip (nominal)

h_w = diameter of the warp

im = interyarn matrix (subscript)

K = bulk modulus

L_f = fill spacing

L_w = warp spacing

m = mass of a projectile

m = matrix (subscript)

$[S_i]$ = compliance matrix

S_{ut} = ultimate tensile strength of the material

S_y = yield strength of the material

T_D = time of dwell

T_i = respective parameter being normalized

T_i^* = normalized parameter

T_T = total thickness of the textile

t_c = thickness of the aluminum-oxide on the biplate

t_i = individual layer thickness

t_k = thickness of the top Kevlar® layer(s) on the biplate

t_m = thickness of the aluminum on the biplate

t_p = overall thickness of the biplate

U_i = invariants of the stiffness matrix

U_R = modulus of resilience

U_T = modulus of toughness

V = general notation for velocity of a projectile

V_f = fiber volume fraction

Appendix B: (Continued)

V_i = volume occupied by various textile components

V_{in} = initial projectile velocity

V_{re} = residual projectile velocity

W_c = critical width of the biplate

W_g = gap caused by the warp

W_p= overall width of the biplate

w = warp (subscript)

wy = warp yarn (subscript)

ε_f = strain at failure of the material

η_i = general notation for the stress partitioning factor

θ = angle of skew on the biplate

v = Poisson's ratio

ρ = material density

ρ_i = individual mass density

ϕ = conoid angle

Appendix C: Analysis Settings for Biplate Finite Element Analysis

The analysis and solver settings used for the finite element analysis of the biplate layer thicknesses in Section 6.1 - Biplate Finite Element Analysis – Setup are shown in Table 52.

Table 52 Analysis Settings used for the analysis of the biplate.

Solution end time (second)	50µ
Energy error	0.3
Automatic mass scaling	Off
Hexagonal integration type	Exact
Geometric strain limit	1.5
AUTODYN standard damping	On
Failure modes:	
On material failure	Yes
On geometric strain limit	Yes
On minimum element time step	No
Elements retain inertia on failure	Yes

Appendix D: Settings Used for Armor System Finite Element Analysis

The analysis settings and preferences used to for the main system finite element analysis (Chapter 7) are shown in Table 53.

Table 53 Settings used for the armor system analysis.

Solution end time (second)	75µ
Energy error	0.47
Automatic mass scaling	Off
Hexagonal integration type	Exact
Geometric strain limit	1.5
AUTODYN standard damping	On
Failure modes:	
On material failure	Yes
On geometric strain limit	Yes
On minimum element time step	No
Elements retain inertia on failure	Yes

Appendix E: Alternative Plate Geometries and Layouts

Several different plate geometrics were considered for the final hybrid armor design. The biplate geometry presented in this work was one of three possible plate arrangments considered. In some ways the biplate shown in this work was the second best choice of the three plates - from a mobility and protection point of view. All three biplate geometries, including the particular plate arrangement tested are shown in Figure 67.

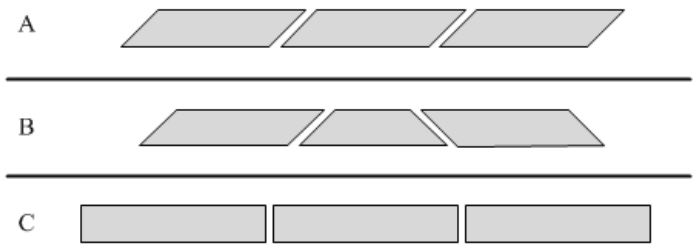

Figure 67 Three plate geometries and layouts considered.

Arrangement A was the plate used for the analysis in this work. Plate arrangement B was inspired by the key stone found in a common stone archway. The concept is that around the harsh transition points on the torso (shown in Figure 30), the "key" plate (center symmetric plate) will be used to minimize the exposed gap.

Plate arrangement C is the simplest design, using squares or rectangles. A very similar arrangement to this was developed as a stab resistant armor in Canada, and proven to be flexible (Croitoro and Boros 2007).